Reactive Halogen Chemistry and Speciation in Volcanic Plumes: UAV-Based In-Situ Measurements and Analytical Developments

Dissertation

for attaining the Academic Degree of

"Doktor rerum naturalium" (Dr. rer. nat.)

of the Department

09 – Chemistry, Pharmaceutics and Geosciences,

of the Johannes Gutenberg-University

Bastien H. Geil

Born 06.01.1991

in Lahnstein

Johannes Gutenberg-University

Mainz, February 2026

1st supervisor:

2nd supervisor:

Date of Examination: 16.04.2026

D77 Dissertation der Johannes Gutenberg-Universität Mainz

Urheberrechtsschutz (in C-1.0)

I hereby declare that I wrote the dissertation submitted without any unauthorized external assistance and used only sources acknowledged in the work. All textual passages which are appropriated verbatim or paraphrased from published and unpublished texts as well as all information obtained from oral sources are duly indicated and listed in accordance with bibliographical rules. I used ChatGPT, DeepL Translate and DeepL Write for grammatical corrections and better readability. In carrying out this research, I complied with the rules of standard scientific practice as formulated in the statutes of Johannes Gutenberg-University Mainz to ensure standard scientific practice.

Mainz, January 2026

Bastien Geil

„In this house, we obey the laws of thermodynamics!“

— Homer Simpson

Table of Contents

Danksagung (in der elektronischen Form gelöscht)

Zusammenfassung

Vulkane gehören zu den wichtigsten natürlichen Quellen halogenhaltiger Gase, die bei Durchmischung mit der Atmosphäre rasch oxidiert und aktiviert werden. Diese Prozesse beeinflussen die atmosphärische Chemie, können zu regionalen Auswirkungen auf Luftqualität und Klima beitragen und dienen potenziell als Indikatoren für vulkanische Aktivität und magmatische Bedingungen. Verbesserte Beobachtungsmethoden zu frühen Halogentransformationen sind daher entscheidend, um atmosphärenchemische Modelle zu verbessern und das Entgasungsverhalten stärker mit Prozessen im Untergrund zu verknüpfen.

Diese Dissertation stellt die Entwicklung, Validierung und Feldanwendung miniaturisierter analytischer Verfahren zur quantitativen Halogenspeziation in vulkanischen Gasfahnen vor, mit einem Schwerpunkt auf Probenahmen mittels unbemannter Fluggeräte (UAV). Im ersten Teil werden chemische Derivatisierungstechniken etabliert und bewertet, die für die selektive Erfassung primärer und reaktiver Halogenspezies ausgelegt sind. Zwei beschichtete Spritzenfilter kamen zum Einsatz: *cis*-Stilben zur Derivatisierung molekularer Halogene und Interhalogene (z. B. Cl_2, Br_2, BrCl) sowie 1,3,5-Trimethoxybenzol (TMB) für nicht näher definierte reaktive nicht- radikalische Halogenspezies (z. B. BrX/ClX/IX) in den Oxidationsstufen 0 oder +1. Parallel wurde ein alkalischer Sammler („Bubbler“) entwickelt, um Gesamthalogene und Schwefel zu quantifizieren. Die Leistungsfähigkeit der Methoden wurde anhand einer eigens konstruierten Chlor-Permeationsquelle sowie kontrollierter Verdünnungskammer-experimente untersucht. Die Tests ergaben Nachweisgrenzen im Pikogrammbereich für die GC-HRMS-basierte Speziation und im Submikrogrammbereich für die Ionenchromatographie der Gesamthalogene, was die Eignung für UAV-Einsätze bestätigt.

Der zweite Teil wendet diese Methoden während UAV-Feldkampagnen am Ätna im Juli 2022 und Juni 2023 an. Der Ätna bietet aufgrund seiner anhaltend hohen Halogenemissionen, seiner guten Zugänglichkeit und seines umfangreichen Monitorings ein ideales Testumfeld, das eine kontrollierte Probenahme in einer gut charakterisierten Gasfahne ermöglicht. Die UAV-Flüge beprobten Gasfahnenpakete mit Altersstufen von etwa 0,1 bis 32 Minuten nach der Emission; das Fahnenalter

wurde aus UAV-Position, Winddaten und visueller Verfolgung abgeleitet. Die Konzentrationen wurden als Halogen-zu-Schwefel-Verhältnisse ausgewertet, um Verdünnungseffekte zu minimieren. Die Messungen zeigen eine rasche Bromaktivierung innerhalb der ersten Minuten der Fahnenalterung, wobei BrX-Spezies gegenüber Br_2 und BrCl dominieren. Dieses Verhalten stimmt mit frühen gasphasenchemischen Oxidationspfaden über HOBr überein und weist auf eine begrenzte heterogene Aktivierung nahe der Emissionsquelle hin. Chloraktivierung ist im Allgemeinen schwächer, zeigte jedoch episodische Cl_2-Anreicherungen, insbesondere unter bromarmen Bedingungen. Reaktive nicht-radikalische Halogene nehmen mit zunehmendem Fahnenalter schnell ab, was auf effiziente Photolyse und mögliche partikelbasierende Senken hindeutet. Unterschiede zwischen den Messkampagnen, darunter höhere Br/S- und IX/S-Verhältnisse im Jahr 2022, deuten auf Variationen in der vulkanischen Magmazusammensetzung oder Entgasungsprozessen hin.

Die Kombination aus analytischen Weiterentwicklungen und Feldmessungen liefert neue Randbedingungen für die Halogenchemie im Quellbereich und zeigt, dass UAV-gestützte Techniken sowohl die Größenordnung als auch die schnelle Entwicklung reaktiver Halogene erfassen können. Die Ergebnisse werden im Kontext früherer Halogenmessungen am Ätna und im Vergleich zu Vorhersagen atmosphärischer photochemischer Modelle interpretiert. Dieser integrierte Ansatz betont die Bedeutung früher Oxidationspfade in der Gasfahne, belegt die Leistungsfähigkeit luftgestützter chemischer Fallen und erweitert die Beobachtungsgrundlage für das Verständnis vulkanischer Beiträge zu atmosphärischen Halogenkreisläufen.

Abstract

Volcanoes are major natural sources of halogen-bearing gases, which undergo rapid oxidation and activation upon mixing with the atmosphere in the plume. These processes influence near-source atmospheric chemistry, can contribute to regional air quality and climate impacts and offer potential indicators of volcanic activity and magmatic conditions. Improving observational constraints on early halogen transformations is therefore essential for improving atmospheric chemistry models and for linking degassing behavior to subsurface processes.

This dissertation presents the development, validation and field application of miniaturized analytical methods for quantitative halogen speciation in volcanic plumes, with a focus on unmanned aerial vehicle (UAV) based sampling. The first part establishes and evaluates a set of chemical trapping techniques designed for selective detection of both primary and reactive halogen species. Two coated syringe filters were implemented, one with *cis*-stilbene to derivatize molecular halogens and interhalogens (e.g., Cl_2, Br_2, BrCl) and 1,3,5-trimethoxybenzene (TMB) for not further defined reactive non-radical halogen species (e.g., BrX/ClX/IX) with oxidation state 0 or +1. In parallel, an alkaline trap system ("bubbler") was developed to quantify total halogens and sulfur. Method performance was assessed using a custom-built chlorine permeation source and controlled dilution-chamber experiments. These tests demonstrated detection limits in picogram range for GC-HRMS-based speciation and sub-microgram detection limits for ion chromatography of total halogens, confirming suitability for UAV deployment.

The second part applies these methods during UAV field campaigns at Mt. Etna in July 2022 and June 2023. Mt. Etna provides an ideal test environment due to its persistent high halogen emissions, accessibility and extensive monitoring record, which together allow controlled sampling in a well characterized plume. UAV flights intercepted plume parcels spanning ages of approximately 0.1–32 minutes after emission, with plume age derived from UAV position, wind data and visual plume tracking. Concentrations were evaluated as halogen to sulfur ratios to minimize dilution effects. The measurements reveal rapid bromine activation within the first minutes of plume aging, with BrX species dominating over Br_2 and BrCl. This behavior is consistent with early gas phase oxidation pathways involving HOBr and limited

heterogeneous activation near the vent. Chlorine activation is generally weaker, although episodic Cl_2 enhancements were observed, especially under bromine-poor conditions. Non radical reactive halogens decay rapidly with plume age, indicating efficient photolysis and possible particle mediated sinks. Interannual differences, including higher Br/S and IX/S ratios in 2022, suggest variability in volcanic source composition or degassing processes.

The combined analytical advances and field observations provide new constraints on near source halogen chemistry and demonstrate that UAV based chemical trapping can capture both the magnitude and the rapid evolution of reactive halogens. The results are interpreted in the context of previous halogen measurements at Mt. Etna and compared with predictions from atmospheric photochemical models. This integrated approach highlights the importance of early plume oxidation pathways, establishes the performance of airborne chemical trapping systems and extends the observational basis for understanding volcanic contributions to atmospheric halogen cycles.

1 Introduction

Atmospheric Relevance of volcanic systems

Volcanoes represent major natural sources of halogens and sulfur to the atmosphere, releasing trace gases that influence the oxidative capacity, ozone abundance and radiative balance of the troposphere (Fig. 2) (Glasow, 2010; Saiz-Lopez and Glasow, 2012). Although water vapor, carbon dioxide and sulfur dioxide dominate in abundance, halogen-bearing species such as hydrogen chloride (HCl), hydrogen bromide (HBr) and hydrogen iodide (HI) exert a disproportionately large impact on atmospheric chemistry (Aiuppa et al., 2005; Symonds et al., 1988). Once emitted, these gases undergo rapid transformation into reactive halogen species (RHS), which participate in catalytic cycles that alter the oxidative state of the atmosphere and contribute to ozone depletion (Glasow and Crutzen, 2003). Understanding the mechanisms and dynamics of these reactions is essential for linking volcanic source compositions to observed atmospheric effects.

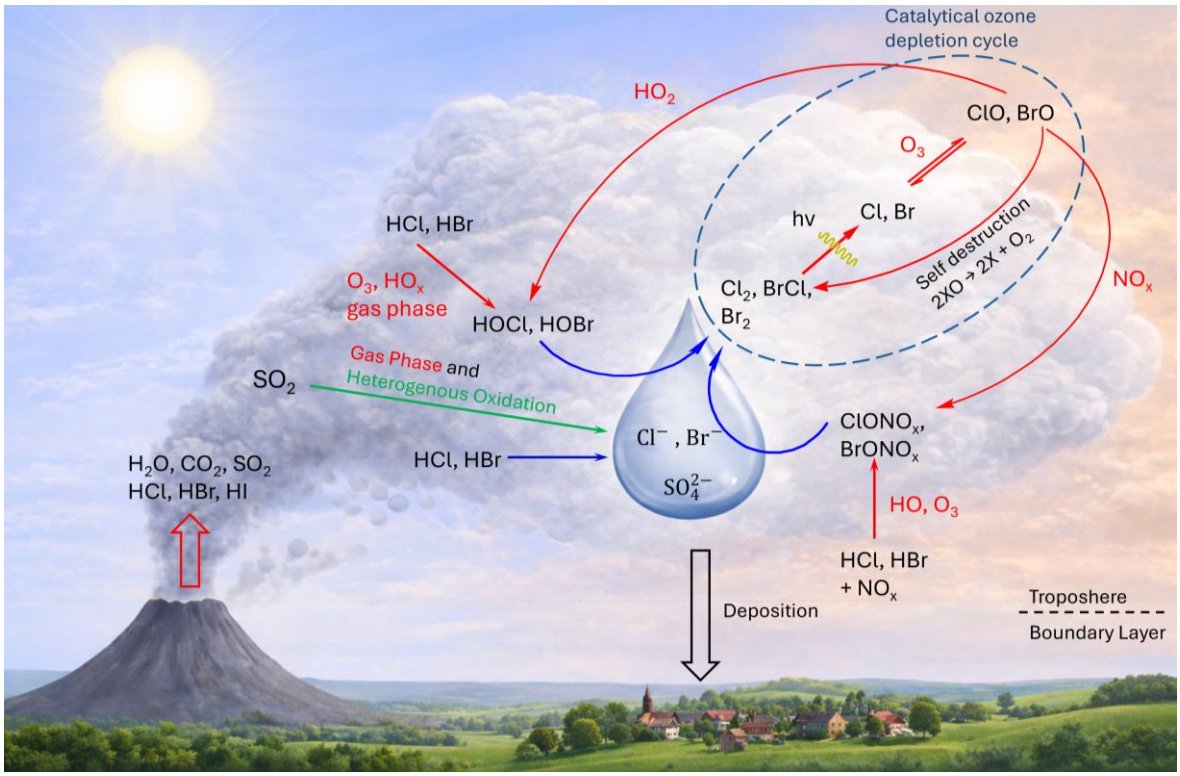

Figure 1: Schematic oxidation pathways of halogen when mixing with ambient air, background designed by ChatGPT 5.2, Open AI.

From an atmospheric perspective, volcanic plumes represent natural systems for multiphase oxidation chemistry under extreme conditions. The combination of high temperatures, reactive gases and rapid aerosol formation creates chemical environments where halogen activation proceeds on timescales of seconds to minutes. Despite their comparatively small contribution to global halogen fluxes relative to anthropogenic sources, volcanic emissions have a disproportionate effect on local and regional atmospheric chemistry, particularly because bromine and iodine are highly efficient catalyst in ozone depletion reaction cycles (Daniel et al., 1999; Glasow, 2010). The tropospheric impacts of these emissions are controlled by rapid multiphase processes involving oxidation, photolysis and aerosol chemistry, whereas only a minor fraction of emitted halogens reaches the stratosphere (Pyle and Mather, 2009). Quantifying reactive halogen formation within minutes after emission is therefore crucial for bridging the gap between volcanic source composition and observed atmospheric transformations.

On broader spatial and temporal scales, volcanic halogens also contribute to atmospheric variability. Major explosive eruptions, such as Pinatubo (1991), injected halogen-bearing aerosols into the stratosphere, enhancing ozone-depleting chemistry (Solomon, 1999). At persistently degassing volcanoes like Mt. Etna, halogen fluxes show strong variability linked to magmatic supply and vent sealing (La Spina et al., 2023; Moretti et al., 2018).

Historical Development of Volcanic Halogen Measurements

The evolution of volcanic halogen research reflects broader advances in analytical chemistry and atmospheric observation. Early studies in the 1960s and 1970s relied on direct sampling of fumarolic gases using evacuated flasks and alkaline absorption bottles, techniques pioneered by Giggenbach (1975). These methods provided quantitative measurements of major species such as HCl, HF and SO_2, but were limited by long collection times, post-sampling reactions and safety constraints near active vents. During the 1980s and 1990s, the emergence of remote sensing techniques, particularly the COSPEC (Correlation Spectrometer) and later DOAS (Differential Optical Absorption Spectroscopy) systems, revolutionized volcanic gas monitoring by enabling remote detection of SO_2 (Stoiber et al., 1987). The first detection of BrO in a volcanic plume marked a turning point, demonstrating that

reactive halogen chemistry occurs even in the troposphere and can be observed spectroscopically (Bobrowski et al., 2003; Bobrowski and Giuffrida, 2012). Subsequent advances integrated multi-axis DOAS, FTIR spectroscopy and airborne platforms, allowing detection of optically active species such as IO and OClO (Gliß et al., 2015; Platt and Stutz, 2008; Schönhardt et al., 2017). However, these optical techniques remained restricted to compounds with distinct absorption features and could not resolve the complete halogen budget, leaving short-lived precursors such as Br_2, BrCl and Cl_2 inaccessible.

To address these limitations, analytical strategies increasingly returned to *in-situ* sampling approaches. Classical methods such as alkaline traps and impregnated filters enabled determination of total halogen and sulfur fluxes (Finnegan et al., 1989; Giggenbach, 1975; Wittmer et al., 2014), but lacked speciation capability due to chemical transformation of reactive intermediates during or after sampling. In the 2010s, *in-situ* sampling techniques gained renewed attention, with a particular focus on chemical derivatization approaches designed to stabilize reactive halogen species directly during sampling and enable chromatographic mass spectrometric detection (Gutmann et al., 2021; Rüdiger et al., 2017). The miniaturization of these systems and their subsequent integration into unmanned aerial vehicles (UAVs) represents the most recent methodological advance, allowing direct access to young volcanic plumes within minutes of emission and at distances of tens to hundreds of meters from the vent (Karbach et al., 2022). This progression from manual bottle sampling to automated, airborne *in-situ* systems illustrate how technological innovation has continually expanded the ability to quantitatively constrain short-lived, chemically reactive halogen species in volcanic plume chemistry.

Atmospheric Chemistry of Volcanic Halogens

The chemical evolution of volcanic halogen species is governed by coupled gas-phase and multiphase reactions that occur as volcanic gases mix with ambient air. These processes control the transition from primary emissions dominated by hydrogen halides to secondary products such as molecular halogens and interhalogens, which play central roles in ozone destruction and oxidation chemistry (Roberts et al., 2009; Saiz-Lopez and Glasow, 2012). The following sections outline the major chemical pathways, microphysical controls and analytical implications relevant to the present study.

Volcanic emissions release large amounts of HCl, HF, HBr and minor HI, which undergo oxidation to produce reactive halogen intermediates. These reactions begin as the hot, moist volcanic gases entrain atmospheric oxidants such as O_3, OH and HO_2. The resulting radicals (Cl, Br, I) react with ozone to form halogen oxides (ClO, BrO, IO), initiating catalytic ozone destruction cycles and the efficiency of these cycles depends strongly on the local photochemical and aerosol environment (Glasow, 2010). Bromine chemistry is particularly effective because BrO–BrO and BrO–ClO cross-reactions lead to the formation of molecular and interhalogen species (e.g., Br_2, BrCl), which photolyze rapidly to regenerate radicals (Marécal et al., 2023; Narivelo et al., 2023; Roberts et al., 2009). The oxidation of hydrogen halides involves several interlinked stages. Initially, reactions with OH and HO_x produce halogen radicals and halogen oxides within seconds of emission. These intermediates react further to form interhalogens and halogen nitrates such as BrCl and $BrONO_2$, which act as short-lived reservoirs. Simultaneously, oxidation of SO_2 generates sulfuric acid aerosols that provide reactive surfaces for heterogeneous halogen activation. In acidic aqueous phases, reactions of hypohalous acids (HOBr, HOCl) with halide ions release molecular halogens such as Br_2, BrCl and Cl_2 (Roberts et al., 2018). The overall reaction network thus represents a coupled multiphase system sensitive to aerosol surface area, pH, humidity and sunlight intensity. The interplay between sulfur and halogen chemistry is central to early plume evolution. SO_2 oxidation to sulfate controls aerosol pH and surface area, while halogen radicals influence sulfur oxidation kinetics (Martin et al., 2006; Roberts et al., 2018). This strong coupling emphasizes the need to measure both halogen and sulfur species simultaneously in volcanic plumes.

The early plume environment is characterized by rapid cooling, turbulent mixing and condensation of water and sulfuric acid droplets (Mather et al., 2004). These microphysical processes control the surface area and acidity of aerosols, which in turn influence the rates of heterogeneous halogen activation. Acidic conditions favor the conversion of HOBr and HOCl into Br_2, BrCl and Cl_2, linking sulfur and halogen chemistry. Modeling studies of Mt. Etna's plume indicate that aerosol loading and entrainment rates strongly determine the abundance of BrO and the extent of downwind ozone depletion (Marécal et al., 2023; Narivelo et al., 2023). These findings underline the need for time-resolved, *in-situ* measurements capable of capturing early plume processes.

High-temperature initiation during mixing with air

The oxidation of halogens in volcanic plumes arises from a coupled sequence of high-temperature and atmospheric processes when magmatic gases mix with ambient air. The reactions summarized below focus on pathways relevant for near-vent volcanic plume chemistry and for interpreting the speciated signals Br_2, BrCl, Cl_2 and BrX, ClX, IX. The following stages of halogen oxidation and reactions with ambient air are based on atmospheric chemical models (Glasow et al., 2009; Nies et al., 2025; Roberts et al., 2009; Roberts et al., 2014; Surl et al., 2021).

Within milliseconds to seconds after emission, hot magmatic gases entrain atmospheric O_2 while still at elevated temperatures. Kinetic modeling shows that reactions between hot H_2O and O_2 generate enhanced HO_x (OH, HO_2) levels in this regime, which efficiently oxidize hydrogen halides (Kuhn et al., 2022):

$$HBr + OH \rightarrow Br + H_2O \quad \text{Eq. 1}$$

$$HBr + HO_2 \rightarrow BrO + H_2O \quad \text{Eq. 2}$$

$$HCl + OH \rightarrow Cl + H_2O \quad \text{Eq. 3}$$

These reactions establish the initial pool of Br, BrO and HOBr/HOCl precursors that feed into the atmospheric halogen cycles observed later in the plume.

Gas-phase oxidation in the cooled plume

Once the plume cools to lower temperatures (hundreds of Kelvin), the chemistry transitions into the gas-phase halogen cycles:

$$Br + O_3 \rightarrow BrO + O_2 \quad \text{Eq. 4}$$

$$Cl + O_3 \rightarrow ClO + O_2 \quad \text{Eq. 5}$$

$$BrO + ClO \rightarrow BrCl + O_2 \quad \text{Eq. 6}$$

$$BrO + NO_2 + M \rightarrow BrONO_2 + M \quad \text{Eq. 7}$$

These reactions control the partitioning between Br, BrO and interhalogens and are directly relevant for interpreting the relative behavior of Br_2, BrCl. Eq. 6 and 7 provide gas-phase pathways to BrCl and $BrONO_2$, both plausible contributors to BrX.

Heterogeneous recycling and bromine explosion

SO_2 co-emitted with halogens is oxidized to sulfuric acid which then forms sulfate aerosol, providing acidic surfaces that promote multiphase halogen activation. A key reaction pathway is the acid-driven conversion of HOBr with dissolved halides into molecular halogens, exemplified by:

$$HOBr + Br^- + H^+ \rightarrow Br_2(g) + H_2O \quad \text{Eq. 8}$$

Analogous reactions with chloride produce BrCl and Cl_2 in the same mechanistic manner. In addition, hydrolysis of $BrONO_2$ regenerates HOBr:

$$BrONO_2 + H_2O \rightarrow HOBr + HNO_3 \quad \text{Eq. 9}$$

These heterogeneous reactions efficiently generate Br_2, BrCl and Cl_2, and regenerate HOBr, which sustains the autocatalytic bromine-explosion cycle. The molecular halogens formed in this way are short-lived and rapidly photolyzed, returning Br and Cl radicals to the gas phase and maintaining the continuous HOBr-driven recycling that characterizes this chemistry.

2 Motivation and aim

Despite major advances in the understanding of reactive halogen chemistry, several fundamental uncertainties remain regarding the temporal evolution, speciation and oxidation kinetics of halogen compounds in volcanic plumes. While the presence of reactive halogen species such as BrCl, Br_2 and Cl_2 has long been predicted by atmospheric chemistry models, their experimental detection and quantification in volcanic plumes had remained elusive. This lack of data is largely due to the analytical challenges of capturing short-lived species under the highly dynamic conditions of near-vent volcanic environments, where temperature, humidity and mixing ratios change on timescales of seconds.

The overarching goal of this dissertation is to advance the understanding of reactive halogen formation and transformation in volcanic plumes by developing and applying novel analytical approaches that combine UAV-based sampling, laboratory validation and mechanistic interpretation. A key motivation was the development of a compact and robust alkaline sampling system ("bubbler") specifically adapted for drone-based operation in volcanic plumes. This device, derived and optimized from established ground-based systems, enables the quantitative determination of total fluorine, chlorine, bromine and sulfur in the gas phase.

The inclusion of sulfur as a quasi-inert tracer is necessary, as the absolute concentrations of plume constituents decrease rapidly with distance from the vent due to atmospheric dilution and turbulences. Without an internal reference, apparent changes in halogen concentrations would reflect only mixing effects rather than chemical transformation. By normalizing halogen species to sulfur (e.g., Cl/S, BrX/S, BrCl/S), dilution-independent ratios can be derived that directly reflect the chemical evolution of the plume. Sulfur dioxide, which remains comparatively stable on short timescales and undergoes oxidation only slowly relative to reactive halogens, therefore serves as an effective internal standard to distinguish physical mixing from chemical conversion processes.

In addition to field sampling, this work establishes several laboratory-based components to support the quantitative accuracy of UAV-borne measurements. A new chlorine permeation source was developed to provide a stable release of chlorine gas over extended periods. This device complements existing bromine and

iodine permeation sources, forming a complete calibration set for halogen and interhalogen species used to validate analytical methods and collection efficiencies.

Furthermore, chemical derivatization filter techniques were developed and optimized for the selective detection of molecular and interhalogen compounds as well as reactive halogen species. Using *cis*-stilbene and trimethoxy benzene (TMB) as derivatization agents, these methods were systematically characterized to ensure quantitative conversion, reproducibility and stability of halogen adducts under laboratory and field conditions.

The combination of these techniques allows for the simultaneous determination of total halogens, molecular halogens, interhalogens, reactive halogens and sulfur species, providing a multi-dimensional view of plume composition and its evolution over time. The resulting time resolved concentration profiles will, for the first time, enable a quantitative assessment of the reactive halogen budget (e.g., Cl_2, BrCl and Br_2) in volcanic emissions. These datasets are intended to serve as validation benchmarks for atmospheric photochemical models, helping to constrain oxidation pathways and heterogeneous processes in multiphase plume chemistry.

Mt. Etna was selected as the field site due to its continuous degassing activity, high and well-characterized halogen flux and accessibility for UAV-based measurements. Its persistent emissions provide ideal conditions to test the newly developed instrumentation, evaluate the spatial evolution of halogen/sulfur ratios and link observed reactive halogen formation to the underlying chemical and physical processes in volcanic plume evolution. This methodological framework therefore underpins the experimental and interpretive components of the dissertation.

3 Volcanic sites

3.1 Mt. Etna

Mount Etna in northeastern Sicily, Italy is one of the world's most persistently active and strongly degassing volcanoes. Mt. Etna's geodynamic setting is complex and is influenced by the Ionian subduction zone and the interaction between the African and Eurasian plates (Díaz-Moreno et al., 2018). Long-term observational syntheses describe Mt. Etna as an evolving open-vent system with recurring cycles of summit and flank activity (Allard et al., 1991; Allard et al., 2006). The currently active summit area comprises the main crater complexes commonly referred to as Voragine, Bocca Nuova, Northeast Crater and the Southeast Crater complex and activity also frequently occurs from numerous flank vents.

Mt. Etna emits large volumes of volcanic gases, producing a sustained summit plume that is routinely used for flux monitoring and process studies. Published measurements demonstrate that Mt. Etna is a significant emitter of bromine and iodine to the troposphere compared with the limited global dataset (Aiuppa et al., 2005). The early plume environment is characterized by strong gradients and rapid chemical evolution driven by atmospheric mixing and photochemistry. For Mt. Etna specifically, BrO/SO_2 evolution has been observed from near-vent values below detection to elevated ratios downwind, implying fast formation of reactive halogen species on short transport timescales (Bobrowski et al., 2007). These properties, together with established ground-based monitoring approaches for volcanic SO_2 emissions (e.g., DOAS networks), make Mt. Etna a suitable source for studying halogen-to-sulfur ratios, primary halogen outputs and early transformation processes in a high-temperature volcanic plume.

3.2 Vulcano

Vulcano is part of the Aeolian arc north of Sicily, whose volcanism is linked to the complex plate-tectonic interaction between the African and Eurasian plates in the southern Tyrrhenian region (Barberi et al., 1974). The current active center is the La Fossa cone within the Fossa caldera, where activity since the late 19th century has been dominated by fumarolic degassing rather than sustained magmatic eruption.

Vulcano is characterized by a coupled magmatic–hydrothermal degassing system. Detailed geochemical studies of crater fumaroles show that the emitted fluids reflect a mixture of magmatic input and hydrothermal interaction and that both temperature and composition can vary substantially through time (Capasso et al., 1999; Chiodini et al., 1995). Reported fumarolic gases include dominant H_2O and CO_2 with sulfur species and acidic gases such as HCl and HF (Aiuppa et al., 2004).

Vulcano is also historically important because the 1888–1890 eruption provided the basis for the definition of the "Vulcanian" eruptive style (Mercalli and Silvestri, 1891). More recently, the 2021–2022 unrest was characterized by increases in fumarolic outlet temperatures and changes in acidic gas species, consistent with enhanced input of heat and magmatic volatiles to the shallow system (Federico et al., 2023). Because Vulcano's degassing is concentrated in a spatially confined fumarolic field at La Fossa, gases can be sampled at the point of discharge and compared across methods (direct sampling, FTIR, filter packs), supporting studies of near-source compositions.

3.3 Nyiragongo and Nyamuragira (DR Congo)

Nyiragongo and Nyamuragira are two highly active basaltic volcanoes in the Virunga region (eastern Democratic Republic of the Congo) and belong to the western branch of the East African Rift, a continental rift system dominated by extensional faulting (EBINGER, 1989).

Nyamuragira has been among the most prolific volcanic SO_2 sources observed from space for decades. Satellite analyses document exceptionally large SO_2 emissions from Nyamuragira and quantify major SO_2 output during both eruptive and passive-degassing phases (Carn and Bluth, 2003). In addition, combined satellite observations during the 2014 activity indicate sustained SO_2 emission rates on the order of tens to >100 kg s^{-1} (Campion, 2014).

Nyiragongo is characterized by persistent open-vent activity with a long-lived lava lake and continuous gas release. Combined ground-based remote-sensing measurements (UV-DOAS for SO_2 flux and open-path FTIR for gas composition) directly characterize the emitted plume, including major contributions from H_2O, CO_2 and SO_2 alongside acid gases (e.g., HCl, HF) (Sawyer et al., 2008). Long-term scanning-DOAS observations further demonstrate sustained quiescent SO_2 degassing over multi-year periods (Arellano et al., 2017).

Taken together, Nyiragongo and Nyamuragira provide a key natural laboratory for quantifying strong SO_2 emissions from an extensional rift setting and for linking gas flux variability to open-vent basaltic activity observed by ground-based and satellite techniques.

4 Analytical Instrumentation

4.1 Gas–liquid and gas–solid mass transfer

4.1.1 Alkaline trap "Bubbler"

Following the classical film theory of gas–liquid mass transfer with fast irreversible reaction as developed by "Gas–Liquid Reactions" (Danckwerts and Lannus, 1970), the uptake of acidic gases HA from a gas stream into an alkaline impinger begins with dissolution at the gas–liquid interface. At the interface, the concentration of dissolved HA is determined by Henry's law,

$$C^* = H_{\mathrm{HA}}\, p_{\mathrm{HA}} \qquad \text{Eq. 10}$$

where C^* is the equilibrium concentration of HA in the liquid phase, H_{HA} the Henry constant and p_{HA} the partial pressure of HA inside the bubble. This interfacial concentration establishes the driving force for transport through the liquid-side diffusion film. The flux across the interface follows the classical film expression

$$N = k_L(C^* - C) \qquad \text{Eq. 11}$$

with k_L the liquid-side mass-transfer coefficient and C the bulk concentration in the liquid. For HA in the presence of excess hydroxide, the neutralisation reaction

$$\mathrm{HA} + \mathrm{OH^-} \rightarrow \mathrm{A^-} + \mathrm{H_2O} \qquad \text{Eq. 12}$$

is extremely fast, so that the bulk concentration remains effectively zero ($C \approx 0$). This enhances the concentration gradient within the diffusion film and increases the apparent liquid-side mass-transfer coefficient, giving an effective value $k_{L,\mathrm{eff}}$ that combines film diffusion and reaction-induced enhancement.

Conventional volume-based gas hold-up formulations assume a homogeneous gas distribution, which does not apply to impingers operating with discrete rising bubbles. The absorption process is therefore expressed directly through the bubble residence time,

$$t_{\mathrm{bubble}} = \frac{H_L}{u_b} \qquad \text{Eq. 13}$$

where H_L is the liquid height and u_b the terminal rise velocity of the bubble. For a spherical bubble of diameter d_b, the interfacial area is $A_b = \pi d_b^2$ and the volume is $V_b = \pi d_b^3/6$, giving a surface-to-volume ratio of

$$\frac{A_b}{V_b} = \frac{6}{d_b} \qquad \text{Eq. 14}$$

Combining the liquid-side flux, the interfacial area and the bubble residence time yields a first-order decay of HA along the bubble path. Integration gives absorption efficiency,

$$\eta = 1 - \exp\left(-\frac{6\, k_{L,\text{eff}}\, H_L}{d_b\, u_b}\right) \qquad \text{Eq. 15}$$

Because impingers inherently operate under turbulent conditions, the liquid-side film is continuously thinned and renewed, which elevates $k_{L,\text{eff}}$ relative to quiescent conditions. Together with small bubble diameters and the defined vertical travel path, this ensures high absorption of reactive species as bubbles ascend through the alkaline solution.

4.1.2 Raschig tube system

A Raschig-ring absorption system provides a complementary approach to alkaline bubblers by extending gas–liquid mass transfer to a packed-film geometry with substantially larger wetted surface area. Raschig rings are hollow cylindrical packing elements widely used in chemical engineering to enhance contact between gases and reactive liquids. When wetted, their external surface hosts a thin liquid film through which diffusion and subsequent chemical reaction can proceed efficiently. This configuration is advantageous when high gas flow rates must be processed or when long sampling intervals are required, conditions under which discrete bubble formation becomes less efficient or more difficult to control.

Figure 2: Rotating Raschig tube system consisting of a glass vessel filled with Raschig rings, mounted on two motor-driven rollers to induce rotation and continuous rewetting of the packing; the gas pump is not shown.

In the configuration employed here, volcanic gases are directed through a horizontally rotating cylinder filled with Raschig rings and periodically wetted with alkaline solution (Fig. 2). Rotation ensures continuous renewal of the liquid film on the packing surfaces, maintaining a large and active absorption interface. Acidic volcanic gases such as HCl, HBr and SO_2 are absorbed into this film according to the same mass-transfer principles outlined earlier for bubble-based traps: diffusion through a stagnant liquid layer, followed by rapid neutralization in the alkaline

medium. In contrast to bubblers, where interfacial area is set by bubble size and gas hold-up, the Raschig system provides a continuous, high-area film controlled by packing density, rotation speed and liquid distribution.

This technique is especially suitable for ground-based fumarole sampling, where weight, size and power supply are not limiting factors. Compared to UAV-based traps, the Raschig system accommodates higher gas flow rates, larger sample volumes and longer continuous collection periods, allowing improved integration of low-concentration species and more stable operation in fluctuating vent conditions. Its mechanical complexity and mass, however, make it unsuitable for aerial deployment.

Packed-film traps of this type follow designs established in atmospheric and geochemical monitoring. A rotating Raschig-ring absorber for quantitative CO_2 trapping with NaOH is described in the ICOS Atmospheric Station specifications, where the technique is used for high-precision carbon isotope studies. A similar Raschig-tube configuration been applied in volcanic gas studies, for example in the acidic-gas sampling system described by Wittmer et al. (2014). These precedents demonstrate the robustness of the technique and provide a methodological basis for adapting packed-film absorbers to halogen and sulfur measurements at volcanic fumaroles.

4.1.3 Coated filters

In the limit of fast irreversible surface reaction and gas-side mass-transfer control, the classical film-theory framework can be reformulated for uptake on reactive filter coatings by replacing the gas-in-liquid residence-time description with a surface-based formulation (Danckwerts and Lannus, 1970). Here the gas contacts a thin reactive film coated on the filter surface and HA is consumed immediately upon arrival at the interface.

Replacing the bubble-specific quantities in Equation 15 by the corresponding filter parameters gives

$$\eta = 1 - \exp\left(-k_g\, A_{\text{filter}}/Q_g\right) \qquad \text{Eq. 16}$$

where k_g is the gas-side mass-transfer coefficient, A_{filter} the accessible coated surface area and Q_g the volumetric gas flow. Turbulent flow over the filter reduces the gas-side film thickness and increases k_g. Although the macroscopic gas–surface residence time is short compared to bubble residence times, the combination of a large surface area and a high $k_g$results in a mass-transfer timescale that remains much smaller than Q_g/A_{filter}. Consequently, quantitative uptake is achieved even at high flow rates.

4.2 Chemical derivatization on filter media

Analytical quantification of highly reactive halogen trace species relies on three coupled steps: (i) transfer of gaseous species to the derivatization medium, (ii) rapid chemical conversion into stable, selective reaction products, and (iii) instrumental detection. As established in Section 4.1, derivatization on coated filters is operated under conditions of gas-side mass-transfer control, such that chemical conversion occurs effectively instantaneously upon contact with the reactive layer.

Under these conditions, the collected amount is directly proportional to the sampled gas volume, minimizing kinetic losses and suppressing breakthrough. Poorly detectable halogen compounds are thereby converted into GC-detectable volatile derivatives, which are subsequently identified and quantified by GC–HRMS.

4.2.1 Electrophilic addition of halogens to *cis*-stilbene

The halogenation of *cis*-stilbene with electrophilic halogen and interhalogen species (XX, XY; with X, Y= F, Cl, Br, I) yields three stereoisomeric addition products: two *syn*-isomers (*R,R*/*S,S*) and one anti isomer (*meso*). These isomers differ in stereochemical configuration and originate from distinct mechanistic pathways. Under heterogeneous conditions, such as reaction between gaseous halogens and a liquid *cis*-stilbene film deposited on a filter, *syn*/*anti* mixtures are typically observed (Fig. 3 top). This behavior is consistent with a planar carbocation-type intermediate that allows nucleophilic attack from either face (Ruasse and Dubois, 1974). In contrast, halogenation in protic solvents proceeds through a concerted anti-addition pathway and yields the meso product (Fig. 3 bottom).

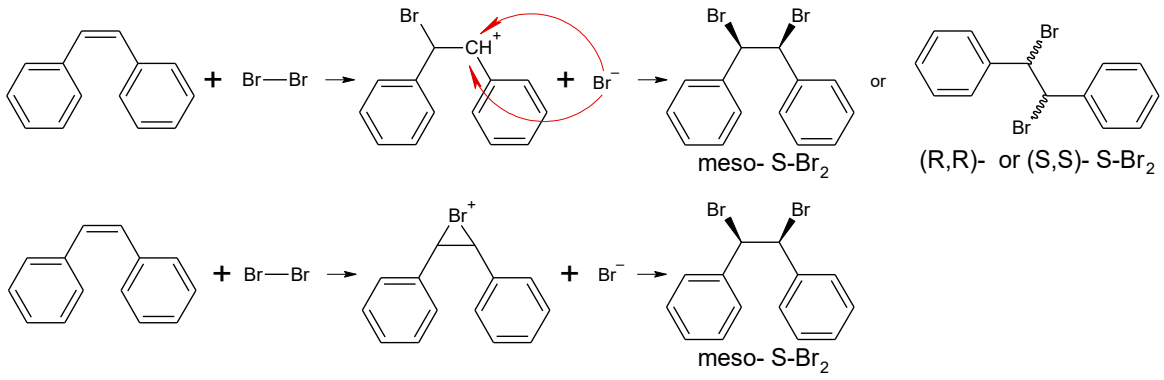

Figure 3: Schematic reaction pathways for the halogenation of *cis*-stilbene with Br_2 , illustrating gas-phase or heterogeneous conditions (top), which yield *syn*/*anti* addition products via a planar carbocation-type intermediate and reactions in protic solvents (bottom), which proceed via concerted anti addition and form the meso isomer.

4.2.2 Electrophilic substitution of reactive halogen species on TMB

Reactive halogen species generally undergo electrophilic substitution at 1,3,5-trimethoxybenzene (TMB). Such reactions require electrophilic, positively polarized halogens (e.g., Br_2, BrOH). In contrast to electrophilic additions, the information on the original gaseous precursor is only partially preserved because different electrophilic halogen species can lead to the same substitution product (Fig. 4). Accordingly, TMB provides a measure of the total reactive halogen fraction excluding radical halogens, which do not react with TMB under electrophilic conditions.

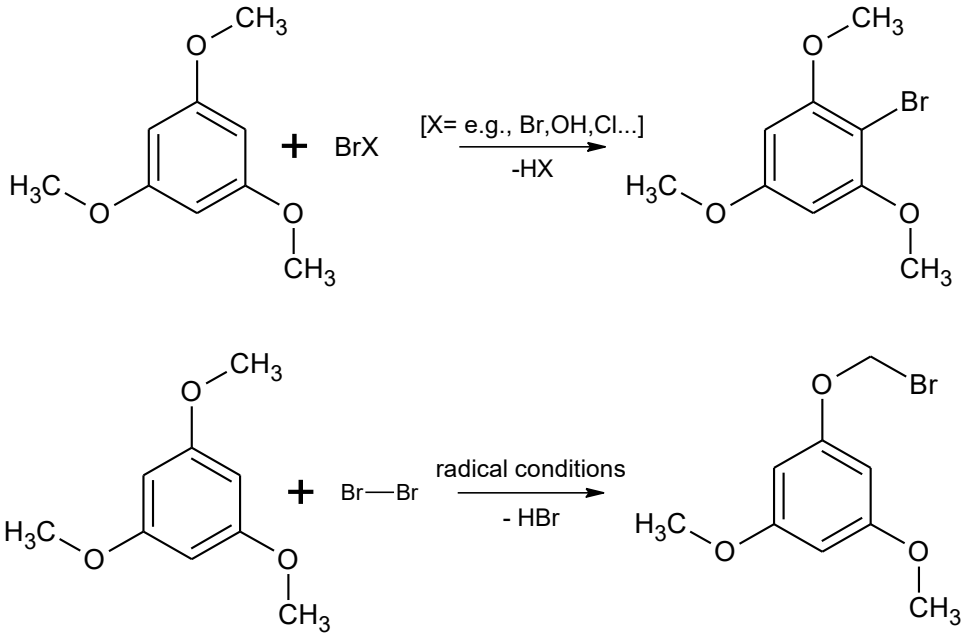

Figure 4: Schematic reaction of 1,3,5-trimethoxybenzene (TMB) with reactive bromine species, illustrating general electrophilic substitution by BrX (top) and, for comparison, the reaction with Br_2 under radical conditions (bottom).

4.3 Permeation

Permeation is the transport of a compound through a membrane. It is governed by the solubility S, the diffusion coefficient D and the thickness of membrane. The permeability P is defined as

$$P = D\,S \qquad \text{Eq. 17}$$

The flux through a material of thickness l is

$$J = \frac{P}{l}(p_1 - p_2) \qquad \text{Eq. 18}$$

where $p_1 - p_2$ is the driving pressure difference and J is the permeated flux.

The internal pressure of a chlorine permeation tube remains constant as long as liquid chlorine is present because evaporation maintains the saturated vapor pressure at fixed temperature. Under these steady-state conditions the output rate (OR) is constant over time. It is defined as the gas volume Q at standard temperature and pressure (STP, 273.15 K, 1 atm) per unit time t that permeates through a membrane with area A and thickness l. The driving force is the internal pressure p_1 and the permeability P_e has the unit $\mathrm{m^3(STP)\,m/(m^2\,h\,bar)}$. Eqs. 19 and 20 summarize the relations (Crank, 1975; Flaconneche et al., 2001):

$$\mathrm{OR} = \frac{Q}{t} = \frac{A}{l} P_e p_1 \qquad \text{Eq. 19}$$

$$P_e = \frac{Q l}{t A p_1} \qquad \text{Eq. 20}$$

4.4 Gas Chromatography – Orbitrap High-Resolution Mass Spectrometry (GC–HRMS)

GC–MS with electron ionization has been a cornerstone of analytical chemistry since the 1960s (Gross, 2019). The invention of Fourier-transform mass analyzers brought high resolution and high mass accuracy to GC applications (Marshall et al., 1998). Orbitrap technology, introduced by Alexander Makarov in 1999, evolved from earlier ion-trap and quadrupole systems. Within GC–Orbitrap configurations, quadrupole and multipole (octupole) ion guides focus and transfer ions from the EI source into the C-trap. These ion optics stabilize transmission and minimize energy dispersion before ions are injected into the Orbitrap analyzer (Hu et al., 2005).

General Principle of Gas Chromatography (Grob and Barry, 2004)

Gas chromatography (GC) separates volatile and semi-volatile compounds based on their partitioning between an inert carrier gas phase and a stationary liquid film immobilized inside a fused-silica capillary column. Analytes are introduced by injection, vaporized and transported by the carrier gas (typically helium) through a temperature-programmed oven. Retention is governed by volatility and intermolecular interactions with the stationary phase, film thickness and temperature ramps. In volcanic plume analytics employing derivatization-based trapping (e.g., halogenation adducts of unsaturated probes), GC provides high chromatographic resolution to separate target analytes from isomeric products and matrix components.

A highly sensitive and powerful instrument for the analysis of volatile molecules is the coupling of a gas chromatograph with a mass spectrometer, abbreviated GC–MS. The gas chromatograph separates the components of a mixture and the mass spectrometer subsequently characterizes the individual components of the mixture. The combination of these two techniques allows for the detection of chemicals in quantities as low as one picogram. Due to this very low detection limit, it is not surprising that GC–MS has a wide range of applications. It is extensively used in medicine, pharmacology, environmental science and forensic analysis.

Inside the column, compounds are separated based on their distribution equilibrium between the mobile phase (carrier gas) and the stationary phase. The choice of

stationary phase depends on the compounds to be separated. To enhance resolution and separation efficiency, the polarity of the stationary phase should match the polarity of the analytes, following the principle “like dissolves like.” The elution order is determined by both polarity and boiling point. In gas chromatography, capillary columns are primarily used. Their advantage lies in the low pressure drop along the column compared with packed columns. This allows the use of longer columns at identical flow rates, increasing the number of theoretical plates and thus improving separation. For compounds with high boiling points, a temperature program can shorten elution times and prevent signal broadening.

In addition to analyte volatility, the carrier gas influences signal shape and resolution. This relationship can be described using the Van-Deemter equation:

$$HETP = A + \frac{B}{v} + C * v \qquad \text{Eq. 20}$$

HETP represents the height equivalent to a theoretical plate, a measure of column efficiency and v denotes the carrier gas flow rate. The eddy diffusion term A describes the different path lengths analyte molecules may take through the column. This term can be neglected for capillary columns but is significant in packed columns. The longitudinal diffusion term B represents the random diffusion of analyte molecules along the column axis, while the mass transfer term C accounts for the time required to establish equilibrium between the mobile and stationary phases. At the optimal flow rate, represented by the minimum of each Van-Deemter curve, helium and hydrogen exhibit higher optimal flow velocities than nitrogen, resulting in shorter analysis times. In addition, the minima of helium and hydrogen are broader than that of nitrogen, which simplifies the optimization of flow conditions. Due to the risk of explosion, helium is generally preferred over hydrogen.

System Configuration and Components

A typical GC–Orbitrap system consists of an injector, a chromatographic column, a transfer line, an ion source, ion optics with a C-trap and an Orbitrap mass analyzer (Fig. 5).

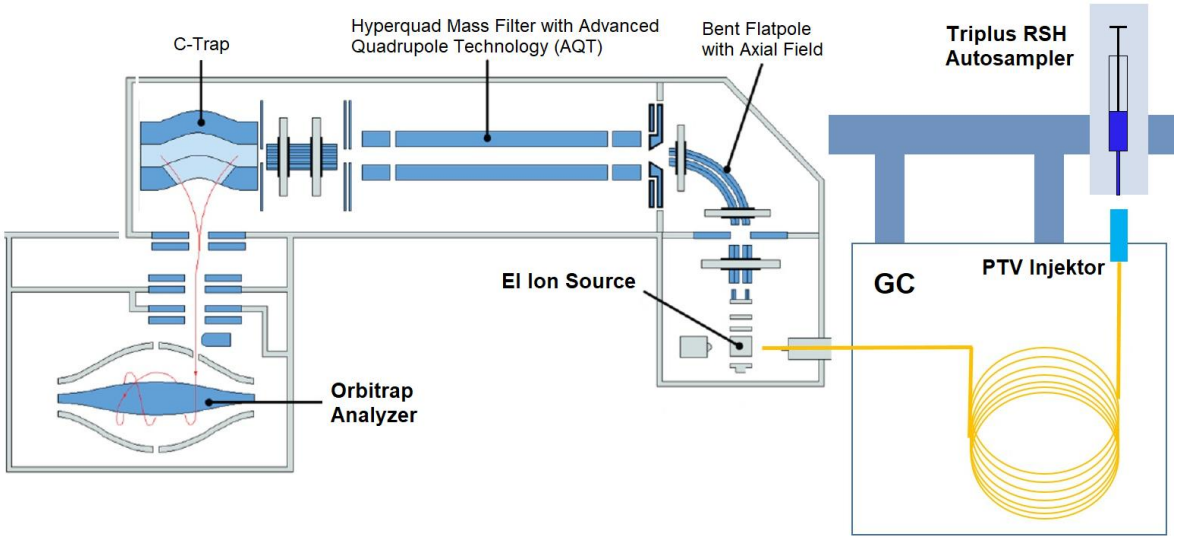

Figure 5: Schematic system of a GC–EI–Orbitrap mass spectrometer. Adapted from Thermo Fisher Scientific.

Injector and Columns

The sample is introduced into the system by means of an injector, which can be operated in either split or splitless mode. In splitless mode, the entire sample is transferred onto the column, resulting in lower detection limits but increasing the risk of column overload and potential damage. In split mode, only 0.1–5% of the injected sample enters the column, reducing sensitivity but preventing overloading. In the liner, the sample is vaporized before entering the column. Besides typical split/splitless (SSL) liners, programmable-temperature vaporization (PTV) liners are used for thermolabile analytes by carefully vaporizing the analyte using a temperature program rather than direct heating, reducing degradation.

Mass Spectrometer and Ion Source

After separation in the chromatographic column, analytes are transferred into the mass spectrometer, which consists of an ion source, a mass analyzer and a detector. In this setup, an electron impact (EI) ion source is employed. In an electron impact ion source, electrons are generated by thermal emission from a heated filament (usually tungsten) and accelerated by a potential gradient of 70 eV between filament and anode (Fig. 6).

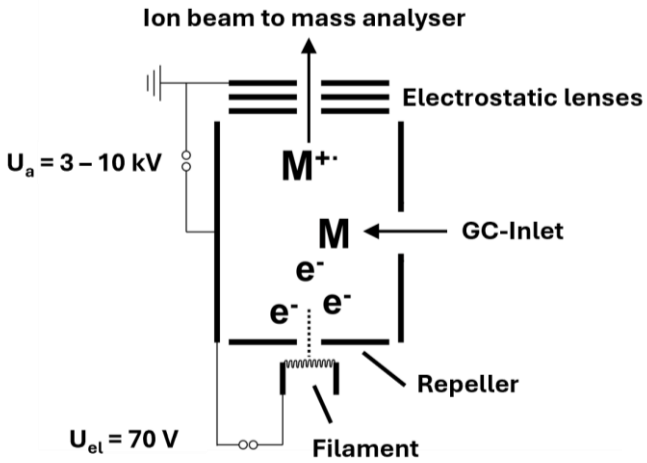

Figure 6: Electron ion impact system (schematic), (Gross, 2019).

The analyte molecules enter the ion source perpendicularly and collide with the accelerated electrons, generating positive or negative radical ions. The formation of radical cations is much more probable than that of radical anions.

$$M + e^- \rightarrow M^{+*} + 2e^- \qquad \text{Eq. 21}$$

Due to the high electron energy (70 eV), analyte molecules fragment after collision, producing characteristic fragmentation patterns for each compound. Reducing the electron energy (e.g., to 20 eV) decreases fragmentation and increases molecular-ion intensity, providing molecular weight information. After ionization, the positively charged repeller plate accelerates the ions toward the ion optics, which focus and direct them into the mass analyzer.

C-Trap / Ion Trap

Before ions can be analyzed in the Orbitrap, they must be accumulated, focused and injected as a temporally and spatially coherent packet. For this purpose, a C-trap (or ion trap) is placed between the ion source and the Orbitrap analyzer. The C-trap temporarily stores the ions and focuses them using dynamic electric fields. Once the desired ion population is accumulated and the trapping potential is released, ions are injected as a narrow, pulsed packet into the electrostatic field of the Orbitrap. This step is essential because the Orbitrap does not continuously accept ions. The detection principle relies on the measurement of collective ion oscillations in the electrostatic field, requiring a coherent ion packet with synchronized kinetic energy and spatial distribution. Without the intermediate accumulation and temporal focusing in the C-trap, ions would enter the Orbitrap with different velocities and phases, leading to signal dispersion, reduced resolution and inaccurate mass determination.

Orbitrap Analyzer

The Orbitrap analyzer traps and detects ions based on their oscillation frequencies in a purely electrostatic field. Ions are injected tangentially into the electrostatic field formed between a central spindle electrode and a coaxial outer barrel. They undergo axial oscillations while orbiting the spindle (Fig. 7).

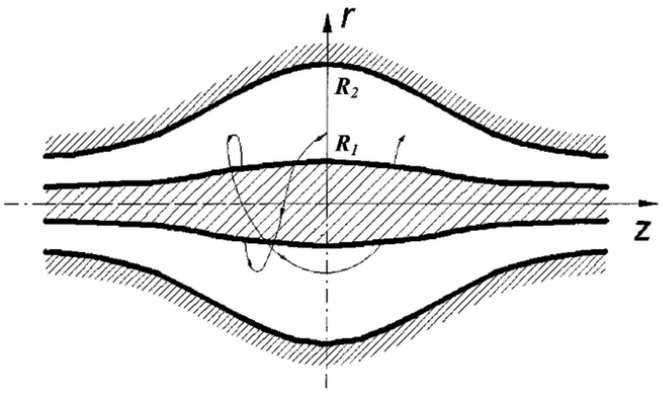

Figure 7: Schematic r–z cross section of an Orbitrap mass analyzer, illustrating the central spindle electrode, the outer electrode geometry (R_1, R_2) and the resulting ion trajectory oscillating along the axial (z) direction within the electrostatic trapping field (Makarov, 2000).

The oscillation frequency ω_z depends solely on the mass-to-charge ratio (m/z) and the force constant of the potential k and is independent of ion velocity (Makarov, 2000).

$$\omega_z = \sqrt{\frac{k}{m/z}} \qquad \text{Eq. 22}$$

The induced image current on detection plates is recorded as a time-domain transient and converted into a mass spectrum via Fourier transformation. This decoupling of frequency from kinetic energy prevents peak broadening typical of TOF (Time of Flight) or sector instruments. The Orbitrap thus combines high mass accuracy with excellent spectral sharpness, achieving resolving powers up to 1.000.000 and sub-ppm precision (Thermo Fischer, 2026).

Quantification, Calibration and Performance

High mass resolution and accuracy offer two advantages for complex volcanic samples. Exact mass measurements constrain elemental compositions of molecular and fragment ions, supporting formula assignment. For targeted quantification, selected ion monitoring (SIM) or narrow full-scan ranges centered on diagnostic ions improve sensitivity while retaining isotopic confirmation. Mass calibration is verified regularly using stable calibrants introduced via the source or transfer line; optional lock-mass correction stabilizes mass accuracy during long sequences. Quantitative performance in GC–Orbitrap analysis depends on chromatographic separation, ionization efficiency and stable transfer at elevated temperatures. Appropriate liner selection, deactivated transfer lines and minimized dead volumes reduce adsorption and thermal degradation of analytes. Calibration typically employs external standard series prepared in the extraction solvent. Method validation includes linearity, precision, limits of detection and quantification and mass accuracy across the working range.

4.5 Ion Chromatography with Suppressed Conductivity Detection (IC-CD)

Ion-exchange separations for inorganic ions emerged in the 1970s as a robust alternative to wet-chemical titrations and colorimetry (Small et al., 1975). The subsequent introduction of chemical and, later, electrolytic suppression transformed ion chromatography (IC) into a high-sensitivity, high-throughput technique that enables routine determination of anions and cations across analytical measurements. Over time, improvements in column chemistry, pump stability, suppressor design and thermal control have expanded the linear dynamic range and pushed detection limits into the low- to sub-micromolar regime for many analytes. High-precision eluent delivery is fundamental to the performance of ion chromatography. Modern systems employ dual-piston high-pressure pumps equipped with pulse dampers to ensure a constant and pulsation-free flow, which is critical for baseline stability in conductivity detection. The use of chemically inert materials such as PEEK throughout the pump head and tubing prevents corrosion and minimizes contamination by metal ions. These developments and with the introduction of integrated quaternary pump heads (Weiss, 2004), marked a major technological advance toward high-pressure, high-reproducibility ion chromatography.

General Principle (Small et al., 1975)

Ion chromatography separates inorganic and small organic ions by their differential retention on an ion-exchange stationary phase and detects them via conductivity after suppression of the background eluent conductivity. The mobile phase consists of the eluent and the dissolved analyte ions and is continuously pumped through the stationary phase inside the column. For anion chromatography, the stationary phase is a polymeric resin functionalized with positively charged quaternary (and in some materials ternary) ammonium groups. Separation is governed by reversible ion exchange between these fixed cationic sites and the anions present in the mobile phase. Under typical conditions, the eluent contains carbonate/bicarbonate or hydroxide; these anions compete with sample anions for exchange sites, continuously shifting the equilibrium and causing analytes to elute over time. Retention increases with stronger electrostatic interaction and decreases with greater solvation. Consequently, species with higher charge density and smaller solvated radii generally elute later than weakly interacting, strongly hydrated anions. The carbonate eluent

needs to be prepared freshly because of degradation of the carbonate eluent over time, changing its retention strength.

The retention behavior of analytes in ion chromatography is governed by ion-exchange equilibria and can be expressed quantitatively by the retention factor:

$$k' = (t_R - t_0)/t_0 \qquad \text{Eq. 23}$$

where t_R is the analyte retention time and t_0 the column dead time. Retention increases with stronger interaction between analyte ions and the charged sites of the stationary phase, which is influenced by the ionic charge, hydration radius and the eluent concentration. A rise in eluent ionic strength shifts the equilibrium toward the mobile phase, decreasing k′ and thus retention times. Selectivity between two ions A and B can be described by the selectivity coefficient:

$$\alpha = k'_A/k'_B \qquad \text{Eq. 24}$$

which reflects the ratio of their equilibrium constants. These relationships form the theoretical foundation for method optimization in IC, linking chromatographic parameters to ion-exchange thermodynamics as first elaborated by (Small et al., 1975), whose pioneering work established modern ion chromatography.

The competitive binding equilibrium for an analyte anion A^- and an eluent anion E^- can be written schematically as:

$$K = \left[\frac{c(A_s^-) \cdot c(E_m^-)}{c(E_s^-) \cdot c(A_m^-)}\right] \qquad \text{Eq. 25}$$

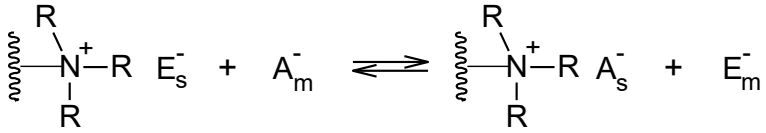

where subscripts m and s denote mobile and stationary phases, respectively. The chemical equilibria governing ion-exchange separation is strongly dependent on pH, ionic strength and temperature. Variations in pH can alter the speciation of weak acids or bases in the sample, thereby influencing their apparent charge and retention. For instance, polyprotic anions such as phosphate or citrate exhibit multiple ionization states and their retention behavior is therefore pH-sensitive. Increasing the ionic strength of the eluent suppresses electrostatic interactions between analyte

ions and the stationary phase functional groups, shortening retention times and potentially leading to co-elution of weakly retained species. Temperature affects both diffusion and solvation, modifying mass-transfer kinetics and selectivity; thus, thermostatted column compartments are essential for reproducibility. Early systematic studies on the temperature dependence of ion exchange (Haddad, 1990; Weiss, 2004) demonstrated that maintaining isothermal conditions can improve retention reproducibility by more than an order of magnitude.

System Configuration and Flow Path

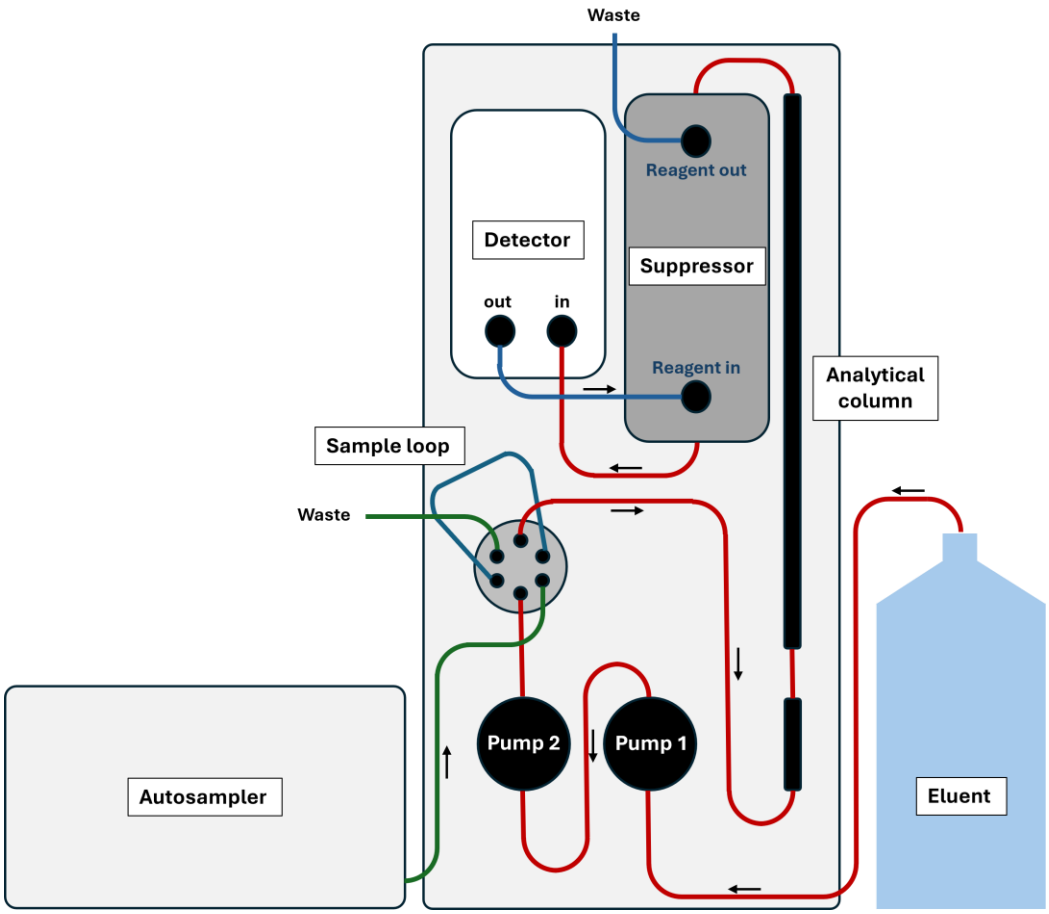

Figure 8: Schematic overview of the ion chromatography (IC) system used in this study, including autosampler, analytical column, chemical suppressor and conductivity detector.

A typical IC system includes an autosampler, a six-port injection valve with a defined sample loop, a high-precision isocratic or gradient pump, a guard column, an analytical ion-exchange column, a chemical or electrolytic suppressor and a conductivity detector (Fig. 8). The autosampler provides reproducible, rapid injections and minimizes operator-induced variability. The injection valve introduces the sample solution into the eluent stream while maintaining overall system pressure

and flow. The guard column, typically packed with the same stationary phase as the analytical column but shorter, protects the analytical column from particulates and strongly retained contaminants. Within the analytical column, separation arises from differential ion-exchange interactions between analyte ions, the stationary phase and competing eluent ions.

Suppression and Conductometric Detection (CD) (Weiss, 2004)

Downstream of the column, the suppressor converts the high-conductivity eluent into a weakly conducting form and simultaneously transforms analyte salts into their corresponding acids or bases, thereby enhancing analyte conductivity relative to the background. The so measured eluent can also serve as the solution that serves as proton donor for neutralization within the suppressor, so called self-regenerating suppressor system. Suppression is essential for sub-micromolar detection limits in IC-CD. In suppressed anion chromatography with carbonate/bicarbonate eluents, a cation-exchange suppressor replaces eluent cations (for example Na^+) with H^+. Carbonate and bicarbonate are protonated to carbonic acid, which decomposes to dissolved CO_2 and water, dramatically lowering the eluent's background conductivity. In parallel, analyte salts are converted to their acid forms (HF, HCl, HBr, etc.). Because these acids dissociate to highly mobile H^+ and the corresponding anions, the analyte conductivity increases relative to the strongly reduced background, improving the signal-to-noise ratio and thereby the detection limits. In electrolytic suppressors, water electrolysis continuously regenerates the exchange capacity *in-situ*, providing long-term stability and eliminating the need for chemical regenerants. In outcome is a low-conductivity baseline and enhanced analyte response at the detector.

Conductometric detection quantifies specific conductance (reported in S cm^{-1}) after the suppression. The measured signal depends on analyte concentration, molar conductivity (a function of charge and hydration) and temperature. Because conductivity varies by temperature, tight thermal control of the flow cell is essential. To avoid electrode polarization, the detector applies an alternating current. While conductivity detection is universal for ionic species, it is not inherently selective among anions with similar molar conductivities; selectivity is instead provided by the chromatographic separation. Method design must therefore consider potential co-elution (for example residual carbonate or small organic anions such as acetate) and

optimize resolution through appropriate column chemistry, particle size, column length and eluent strength or gradients.

Fluoride analysis is still state of the art using ion chromatography because fluoride cannot be reliably quantified by multi-element techniques such as ICP-MS or ICP-OES, where it forms volatile species or poorly ionizing fluorides that cause severe signal instability. IC, in contrast, allows direct, interference-free separation and quantification of fluoride with high sensitivity and reproducibility even in complex matrices.

IC–MS Coupling (Pacholec et al., 1986)

Although conductivity detection is the canonical pairing for IC, coupling IC to mass spectrometry (IC–MS) has become increasingly attractive where lower detection limits, molecular confirmation, or isotopic information are required. This coupling is technically demanding, particularly with respect to eluent volatility and ion-source compatibility, but promises additional selectivity and sensitivity, especially for weak or co-eluting signals and can provide structural information for organic acids and other ionizable species. The coupling of ion chromatography with mass spectrometry represents a significant evolution beyond classical conductivity detection, allowing both quantification and structural information of ionic and polar compounds. Successful interfacing requires the use of volatile eluents, such as ammonium bicarbonate or ammonium acetate, to ensure compatibility with electrospray ionization (ESI) sources. The suppressor plays a critical role in minimizing ion load to the MS by converting non-volatile eluents into neutral, volatile species like CO_2 and water. Despite the technical challenges, ion suppression and solvent load, IC–MS provides selectivity and lower detection limits, enabling the identification of trace anions and weak organic acids.

5 Method development

The following section is part of a planned publication entitled “On-Filter Derivatization and Alkaline Trap Sampling for UAV-Based Gas-Phase Halogen Speciation in Volcanic Plumes” which has been submitted to *Analytical and Bioanalytical Chemistry* and is currently under peer review; the authors are Bastien Geil, Nicole Bobrowski, and Thorsten Hoffmann, with Nicole Bobrowski and Thorsten Hoffmann having substantially contributed to the writing of the manuscript.

5.1 Alkaline trap

The alkaline trap used in this study was developed as a miniaturized alternative to classical impingers to reduce sample volume and overall payload during UAV deployment. Each trap consisted of a borosilicate vial fitted with a screw cap into which a 4 µm polyethylene frit (HPLC solvent filter, Techlab) was inserted and connected to the inlet line. For each experiment, two bubblers were charged with 4 mL of 0.5 M NaOH, while a third downstream bubbler remained empty and acted as a safety trap in case of liquid carry-over. The bubbler configuration and relevant technical details are shown in Figure 9. Laboratory sampling was typically performed at 250–500 mL min^{-1} for 15–30 min using Sensidyne GilAir Plus pumps. For UAV-based deployments, lightweight membrane pumps were used to minimize mass and power consumption while maintaining stable flow rates suitable for gas sampling (Karbach et al., 2022). During operation, the frit remained fully submerged to generate fine bubbles and ensure efficient gas–liquid transfer.

After sampling, 1 mL of the alkaline solution was oxidized by adding 2 µL of hydrogen peroxide and allowing the mixture to react for 24 h at room temperature. Excess peroxide was removed by adding a small amount of MnO_2 and leaving the suspension to react for 48 h. Samples were then neutralized using a cation-exchange resin that had been prewashed until free of anions.

In developing this approach, the handling of the bubbler system was evaluated and adapted. The design was originally inspired by filter-based techniques, impingers and Raschig tubes, all of which show specific advantages and limitations. Filters suffer from breakthrough and require an organic coating to stabilize NaOH, which can interfere with ion chromatography. Raschig tubes are robust but heavy and optimized

for long-duration sampling. The bubbler offers a lightweight alternative that is easily integrated into UAV platforms while avoiding the breakthrough behavior typical of filters.

The neutralization step was improved by replacing an external suppressor-based neutralization with the cation-exchange resin approach. This reduced sample volume requirements and provided a more robust and reproducible procedure (Geil, 2021). The resin was regenerated and freed from interfering anions by washing with 99.99 % HNO_3, which improved blank levels.

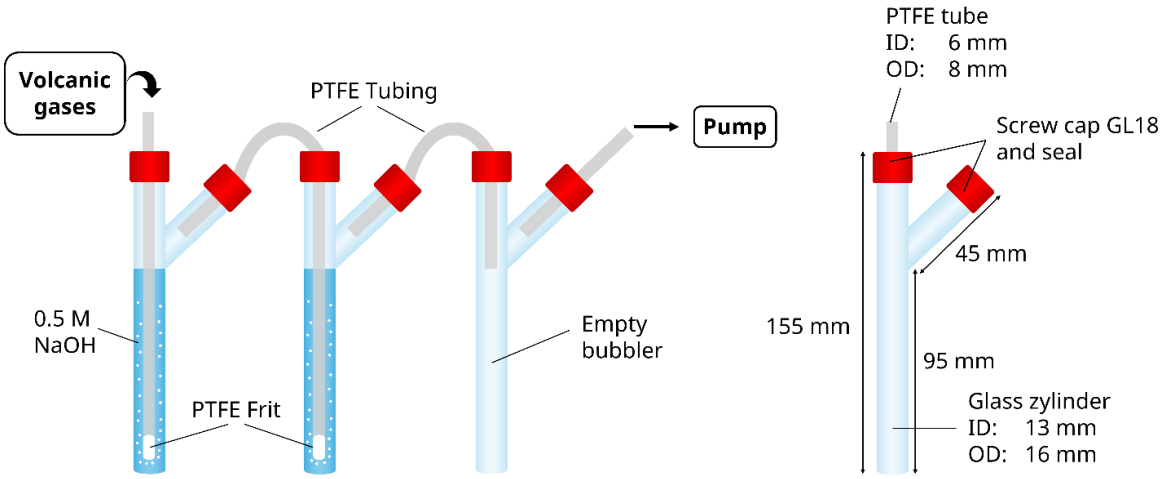

Figure 9: Schematic representation of the alkaline trap ("Bubbler") with some technical details.

Ion chromatographic measurements were performed using a Dionex ICS-1100 equipped with an AS14A analytical column and precolumn, 4 mm AERS suppressor (55 mA), a 100 µL injection loop and an autosampler. The eluent consisted of a carbonate/bicarbonate mixture (1 mM $NaHCO_3$ + 8 mM Na_2CO_3) delivered at 1.0 mL min^{-1}. The detector was set at 40 °C and all samples and standards were analyzed at least in duplicate. Chromeleon 7.1.2 was used for peak integration. Quantification was based on external calibration.

5.2 Chlorine test gas source

A reliable Cl_2 standard was required for filter characterization and a new source had to be developed because the approaches used for Br_2 and I_2 generation were not applicable to chlorine (Huang and Hoffmann, 2010). Two PTFE permeation sources were therefore constructed (Fig. 10) and filled with pre-cooled liquefied chlorine. Chlorine gas was produced by adding concentrated hydrochloric acid dropwise to potassium permanganate in a glass flask. The evolving gas was flushed with a gentle nitrogen stream into a glass collection tube placed in a −70 °C cooling bath, where it condensed as a yellow liquid. After filling, both permeation tubes were sealed with PTFE plugs.

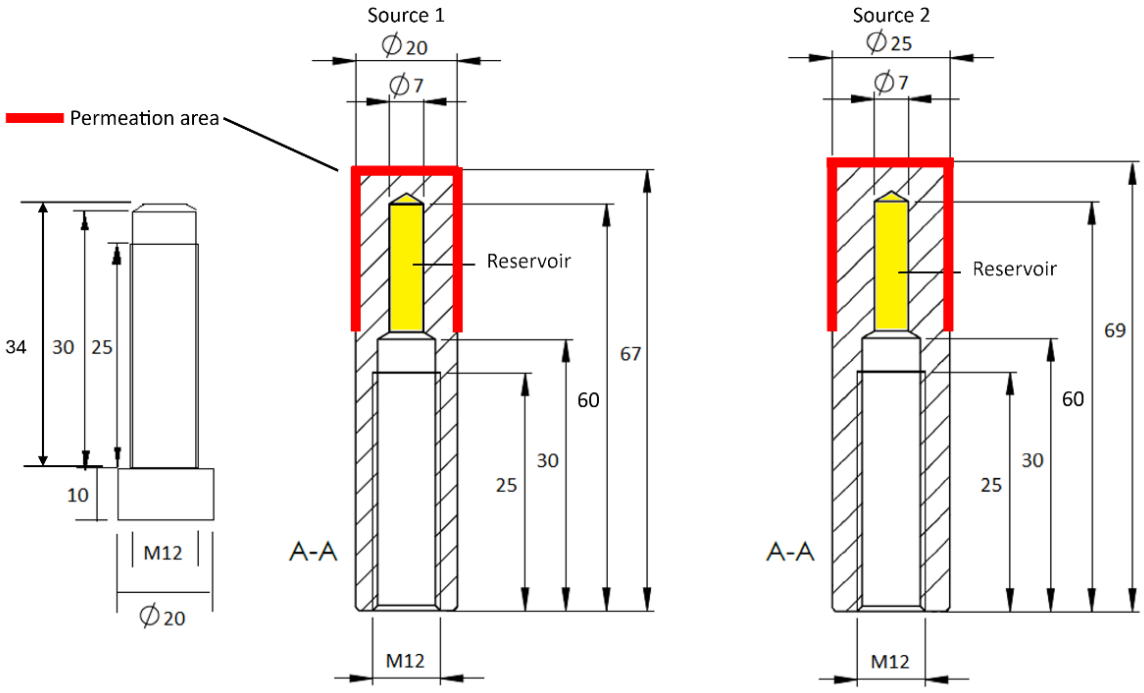

Figure 10: Chlorine permeation tubes, Source 1 (left) and Source 2 (right), all dimensions in mm, PTFE source (hatched area), chlorine reservoir (yellow), active permeation area (red).

Permeation behavior was characterized gravimetrically. Each device was placed in a temperature-controlled chamber at 30 °C and flushed continuously with nitrogen at 50 mL min^{-1}. Mass was recorded at weekly intervals over several months to determine the initial equilibration phase and the long-term stable output rate. Commercial chlorine sources exist, but they contain only gaseous Cl_2 inside the permeation body. Their output is less stable, they cannot be refilled and their operational lifetime is limited compared to the source developed here. Chlorine cylinders offer an alternative but are expensive and introduce substantial safety risks

in routine laboratory work. Another option would be to purchase premixed Cl_2 calibration gases at defined concentrations, but this is also costly in long-term applications.

5.3 Coated Filter for reactive halogen derivatization

Syringe filters (Macherey-Nagel GF-100/25, 25 mm diameter, 1 µm pore size) were used as substrates for the derivatization coatings. For *cis*-stilbene filters, 150 µL of a 30 mM solution of *cis* -stilbene (0.81 mg ± 2 %) in acetone was applied to each filter. The solvent was allowed to evaporate under a gentle stream of laboratory air. The filters were used immediately or sealed and stored at 5 °C to prevent isomerization. TMB filters were prepared analogously using 30 mM TMB (0.76 mg ± 2 %) in acetone; in contrast to *cis* -stilbene, TMB is not prone to isomerization and could therefore be stored at room temperature without detectable changes. After sampling, filters extracted in glass vials four times with 300 µL of acetone (for stilbene filters) or toluene (for TMB filters). Combined extracts were evaporated under nitrogen at 35 °C using a TurboVap system and reconstituted in 200 µL acetone before analysis. The extracts were sonicated twice for 5 min to ensure complete dissolution (Fig. 11).

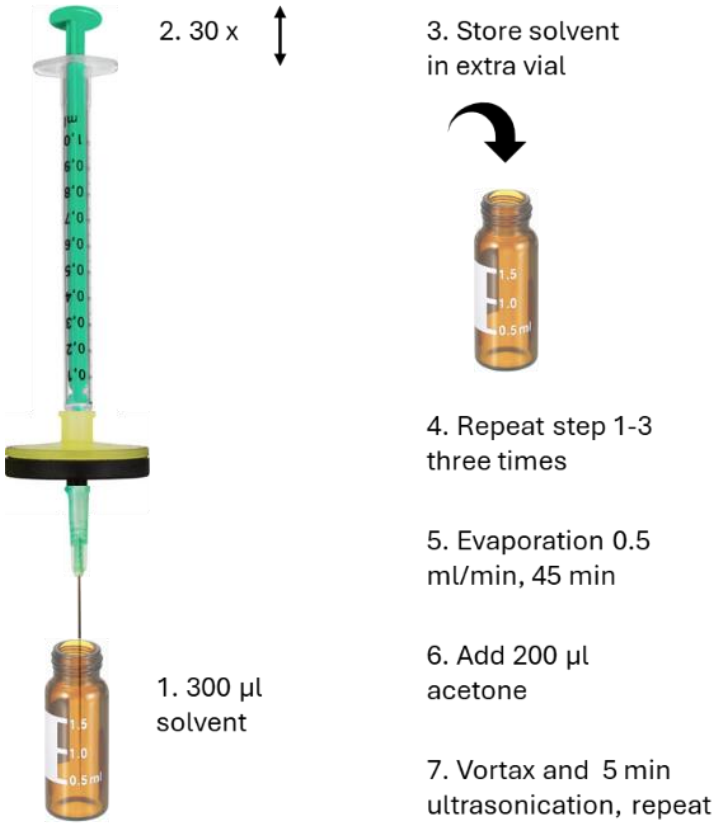

Figure 11: Procedure for extracting the syringe filters after sampling.

This technique builds on earlier work by Julian Rüdiger, who coated denuders with TMB (Rüdiger et al., 2017). However, denuders cannot retain liquid coatings such as *cis* -stilbene and are therefore unsuitable for this purpose. Therefore, the TMB coating approach was also transferred to filters to create a complementary two-filter system.

Analyses were performed using a Thermo TRACE 1610 gas chromatograph coupled to an Orbitrap Exploris high-resolution mass spectrometer operating in electron-impact mode (70 eV). A programmed-temperature-vaporization (PTV) injector was employed minimizing thermal decomposition. For the *cis* -stilbene products, the injector temperature was initially held at 70 °C and then ramped to 200 °C at 14.5 °C min^{-1}. The oven was operated according to the following program: 40 °C for 2 min, 30 °C min^{-1} to 160 °C, then 4 °C min^{-1} to 190 °C (3 min hold) and finally 80 °C min^{-1} to 260 °C (5 min). TMB derivatization products were analyzed using a separate program starting at 90 °C (3 min), followed by 10 °C min^{-1} to 210 °C, 7 °C min^{-1} to 235 °C and 20 °C min^{-1} to 250 °C (5 min hold). Quantification was carried out in SIM mode using characteristic fragment ions listed in Table 1. For stilbene derivatives, response factors of anti-isomers were used for quantifying syn-isomers in the absence of authentic standards.

Table 1: Characteristic ion fragments and retention times for reaction products of halogens with *cis* -stilbene and TMB.

Filter	Analyte	SIM (selected ion monitoring)	m/z	Retention time [min]
	S-Cl_2	C_7H_6Cl	125.0153	14.4 and 14.9
cis -stilbene	S-BrCl	$C_{14}H_{12}Cl$	215.0622	16.5 and 16.8
	S-Br_2	$C_{14}H_{12}Br$	259.0117	17.5 and 17.7
	Cl-TMB	$C_9H_{11}O_3Cl$	202.0391	13.0
TMB	Br-TMB	$C_9H_{11}O_3Br$	245.9886	14.0
	I-TMB	$C_9H_{11}O_3I$	293.9747	15.0

Collection efficiency experiments were performed in a 5 L dilution chamber through which halogen gases were introduced either in nitrogen (0 % RH) or in laboratory air (95 ± 5 % RH). Chlorine was introduced using the developed permeation tubes, while bromine and iodine sources followed previous studies (Huang and Hoffmann, 2010); bromine chloride was generated *in-situ* by simultaneous activation of bromine and chlorine sources in the dilution chamber.

Three filters or bubblers were connected in series; the targeted analyte substances were passed through the absorber and the amount of reaction product on each stage was quantified to evaluate breakthrough behavior (Fig 12). Collection efficiencies (CE) were calculated using Equation 26. Flow rates of 250, 500 and 750 mL min^{-1} were tested. Additional experiments evaluated the influence of humidity, oxygen and sampling duration. Recovery tests were conducted by applying known amounts of calibration standards directly onto filters, followed by the same extraction and analysis procedure as for sampled filters. The resulting recovery factors were incorporated into the determination of detection and quantification limits.

$$\text{CE}\,[\%] = \frac{n_1}{(n_1 + n_2 + n_3)} * 100 \qquad \text{Eq. 26}$$

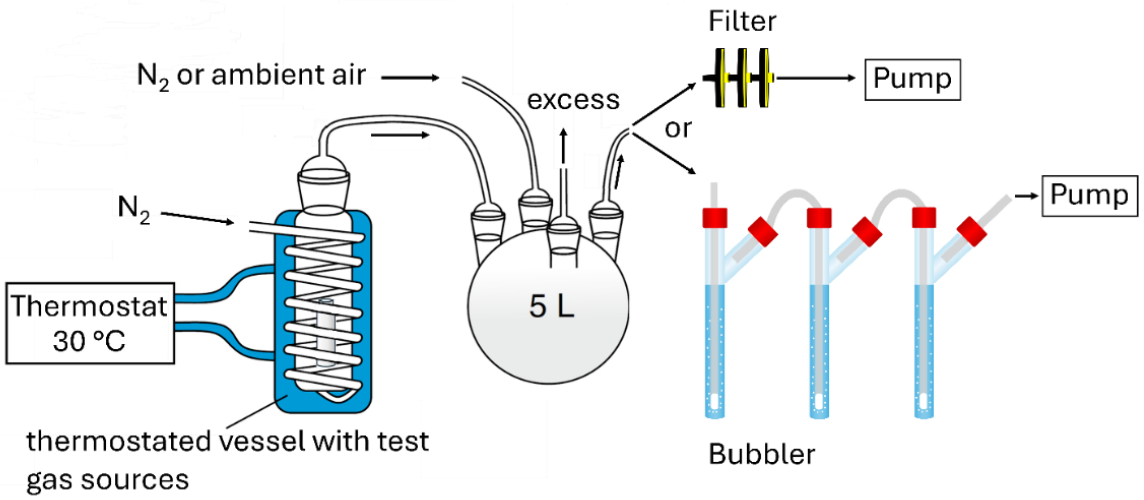

Figure 12: Experimental setup for collection efficiency measurements of alkaline traps and coated filters.

Any potential coating loss during preparation, laboratory handling or storage is inherently accounted for by the experimental design. This includes shelf-life aspects such as storage at room temperature or at reduced temperature, depending on the coating material. Filters were prepared, stored and handled in the same manner as for field deployment and subsequently subjected to collection efficiency experiments under deliberately extreme laboratory conditions with respect to flow rate, sampling duration and temperature.

5.4 Determination of detection and quantification limits

Limits of detection (LOD) and quantification (LOQ) were determined from calibration statistics. LODs were calculated as 3.3 times the standard deviation of the y-intercept of the calibration curve divided by the slope. LOQs were defined as three times the corresponding LOD.

Calibration data used for LOD and LOQ estimation were restricted to the low-concentration range relevant for trace-level detection. This ensures that the derived limits reflect instrumental noise and variability close to the detection threshold rather than signal behavior at higher concentrations.

5.5 Results and discussion

5.5.1 Performance and Analytical Stability of the Alkaline Trap

The alkaline trap was developed to provide quantitative absorption of acidic volcanic gases while keeping mass and sample volume low enough for routine UAV operation. Its performance was evaluated in controlled dilution-chamber experiments (Fig. 12), where the setup was challenged with both weak and strong acidic gases to assess overall trapping efficiency. To ensure that the system remained effective under demanding conditions, the applied gas flow rates and sampling durations were deliberately chosen to exceed those typically encountered during UAV plume measurements. This served as a practical stress test for the trap design.

In these experiments, CO_2 (550 ± 100 ppm) and SO_2 (22 mg in total) were passed through three bubblers arranged in series. Collection efficiencies were calculated according to Eq. 26. The results, summarized in Table 2, show that SO_2 was absorbed with an efficiency of 100 ± 1.0 %. CO_2, although only weakly acidic in aqueous solution, was still collected with an efficiency of 98 ± 5 %.

Table 2: Results of collection efficiency measurements for alkaline traps.

Method	Analyte	Flow [mL min^{-1}]	Sampling time [min]	Humidity [%]	Collection efficiency [%]
Alkaline trap	SO_2 (22 mg) CO_2 (550 ± 100 ppm)	500 ± 25	150	65 ± 10	100 ± 1 98 ± 5

These findings demonstrate that the gas–liquid transfer and subsequent neutralization inside the alkaline trap are highly effective. The system therefore offers sufficient capacity and reactivity to ensure near-quantitative uptake of hydrogen halides (HF, HCl, HBr), whose acid–base behavior in alkaline solution is considerably stronger than that of CO_2.

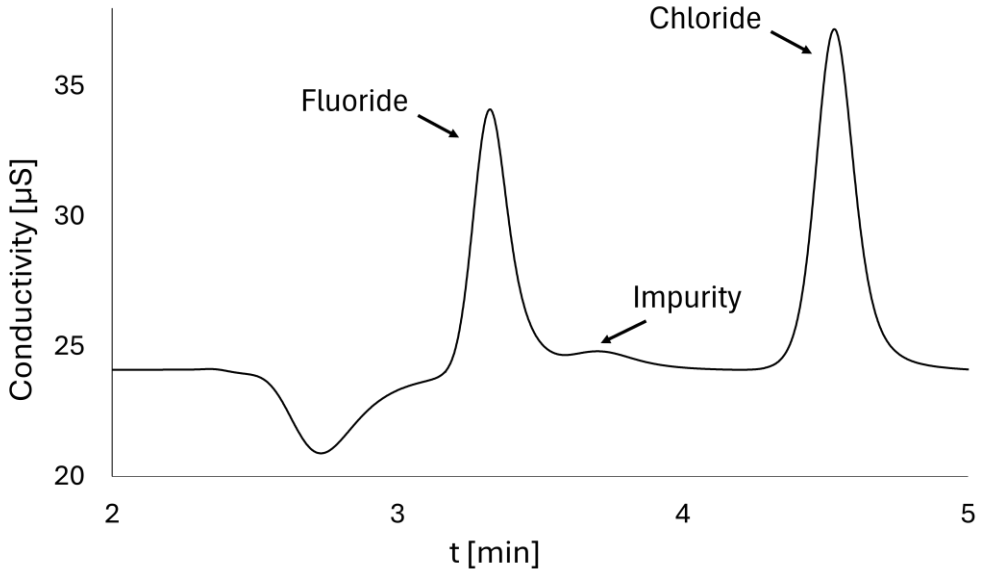

Figure 13: Standard solution of NaF and NaCl in 0.5 M NaOH after sample treatment showing an additional signal at 3.7 min, probably caused by a reaction of hydroxide with the plastic container after two days of storage.

A storage-time-dependent impurity peak at 3.7 min appeared in the IC chromatograms (Fig. 13). This peak is attributed to slow chemical interactions between the NaOH solution and the polymeric storage vial. Glass containers were not considered as an alternative, as concentrated alkaline solutions are known to attack glass surfaces, potentially releasing silicates and introducing additional artefacts relevant for anion analysis. Under normal handling conditions the impurity did not interfere with the fluoride or chloride peaks, but it became noticeable when alkaline solutions were stored for extended periods. This also highlights that the NaOH working solution should be prepared fresh, since prolonged storage before sampling increases the likelihood of impurity formation.

Cooling the alkaline solution to 5 °C markedly slowed the development of the impurity peak, indicating a temperature-dependent reaction that can be reduced but not fully suppressed. In contrast, once samples had been neutralized after collection, the resulting solutions showed stable behavior and no further impurity growth,

confirming that the instability is restricted to the alkaline storage phase. Prompt analysis of collected samples is therefore recommended to minimize storage-related artefacts. Under these conditions the trap delivers consistent and reliable analytical performance suitable for field deployments.

Recovery experiments demonstrated that neither the oxidation step with H_2O_2 nor the subsequent neutralization with cation-exchange resin introduces measurable bias into the analytical results. A reference solution and an identical solution that had undergone the full alkaline treatment were compared. All anions showed recoveries of 95 ± 5 %, indicating that both processing steps preserve the original halogen and sulfur content. In combination with the high collection efficiencies of the alkaline trap, this ensures that total halogen and total sulfur budgets can be quantified reliably.

The limits of detection and quantification were calculated from calibration standards, sampled air volume, flow rate, recovery and collection efficiency. The resulting values are listed in Table 3. LODs ranged from 0.012 µg for HBr to 1.7 µg for SO_2. Under typical UAV sampling conditions (250 mL min^{-1}, 15 min), these values correspond to sub-ppb to mid-ppb mixing ratios. Such detection limits are fully adequate for near-vent measurements at open-vent systems such as Mt. Etna, where halogen and sulfur concentrations commonly exceed these thresholds.

Table 3: Alkaline trap: LODs and LOQs in absolute amounts and in their mixing ratios at normal conditions using typical sampling settings, flow 250 mL min^{-1}, sampling time 15 min.

	Alkaline trap "Bubbler"			
Limit	**HF**	**HCl**	**HBr**	**SO_2**
LOD (µg)	0.022	0.62	0.011	0.51
LOD (ppbv)	6.6	100	0.84	47
LOQ (µg)	0.066	1.9	0.034	1.5
LOQ (ppbv)	20	310	2.5	140

5.5.2 Stability and Output Characteristics of the Chlorine Permeation Source

For characterization, the newly developed chlorine source was kept at 30 °C and its mass was recorded at weekly intervals. The resulting mass-loss curves, monitored over several months, showed an initial non-linear permeation stage followed by a well-defined linear regime. The transition to steady-state behavior occurred after approximately 6 weeks for Tube 1 and 9 weeks for Tube 2. Once this equilibrium was established, the permeation rate remained stable for 4–8 months, depending on the initial quantity of liquefied chlorine loaded into the device (Fig. 14).

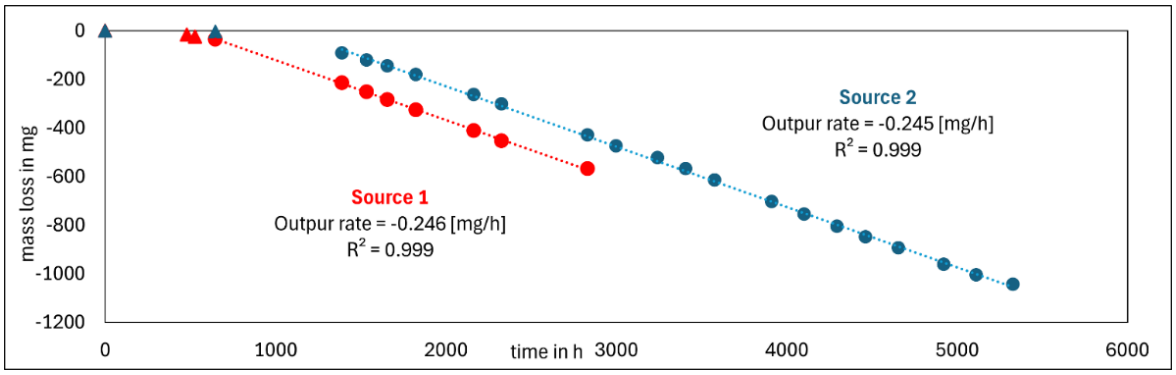

Figure 14: Output rate for two different chlorine sources.

Interestingly, both tubes – despite different wall thicknesses – exhibited identical output rates (0.245 and 0.246 mg h^{-1}). This is consistent with their nearly identical permeation-area-to-wall-thickness ratios (A/l), the dominant factor controlling permeation (Flaconneche et al., 2001; Crank, 1975). Permeability coefficients derived from the steady-state regime agreed well with literature values (Table 4), confirming that the PTFE devices behave predictably according to established permeation theory (Hägg, 2000).

Table 4: Permeability of Cl_2 in PTFE Membranes; $P_e = [m^3 \cdot (STP) \cdot m/(m^2 \cdot h \cdot bar)] \times 10^7$.

	A/l [m]	Output rate [mg/h]	P_e (this study) at 30 °C, 8.9 bar	P_e (Hägg, 2000) at 30 °C, 1-3 bar
Source 1	0.37	0.246	0.26	0.13
Source 2	0.36	0.245	0.26	

5.5.3 Performance of *cis* -Stilbene-Coated Filters

Cis -stilbene reacts readily with Cl_2, Br_2 and BrCl via electrophilic addition (Fig. 15), forming distinct di-halogenated stilbene products. For the chamber experiments, Cl_2 and Br_2 were introduced together into the dilution chamber, which resulted in the *in-situ* formation of BrCl. Because wall losses occurred and Cl_2 and Br_2 reacted with each other, the absolute concentrations of the individual gas-phase species could not be determined reliably. Despite this limitation, the experiments clearly showed that cis-stilbene captures all three halogen species with very high efficiency. Under extreme test conditions (750 mL min^{-1}, 30 min), the resulting collection efficiencies exceeded 100 % for all analytes. This confirms the strong reactivity of *cis*-stilbene toward molecular halogens and interhalogens.

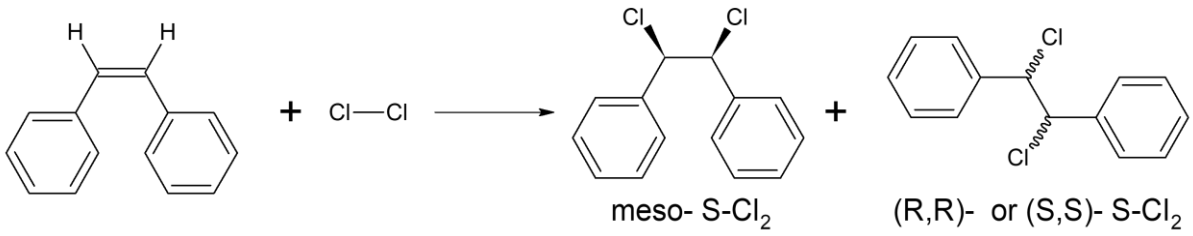

Figure 15: Reaction of cis stilbene with chlorine, analogous reaction for bromine and bromine chloride.

Table 5: Sampling conditions (T = 303.25 K) and collection efficiencies for cis-stilbene and TMB-coated filters.

Method	Analyte	Flow [mL min^{-1}]	Sampling time [min]	Humidity [%]	Collection efficiency for all analytes [%]
Cis-Stilbene	Cl_2 (5.2 ppmv) Br_2 (60 ppbv)	250 ± 12.5	30	0 (pure N_2)	100 ± 1
	Cl_2 (2.6 ppmv) Br_2 (30 ppbv)	500 ± 25	30	0 (pure N_2)	100 ± 1
	Cl_2 (1.7 ppmv) Br_2 (20 ppbv)	750 ± 37.5	30	95 ± 5 (lab air)	100 ± 1
	Cl_2 (2.6 ppmv) Br_2 (30 ppbv)	500 ± 25.0	60	0 (pure N_2)	48 ± 1 (Cl_2) 65 ± 1 (BrCl) 91± 1 (Br_2)
TMB	Cl_2 (1.7 ppmv) Br_2 (20 ppbv) I_2 (14 ppbv)	750 ± 37.5	60	95 ± 5 (lab air)	100 ± 1

Under extended and deliberately extreme sampling conditions (60 min, 500 mL min^{-1}), breakthrough was observed for the more volatile halogens. Cl_2 showed the strongest breakthrough (48 %), followed by BrCl (65 %), whereas Br_2 was retained to a much higher degree (91 %) (Tab. 5). The differing behavior likely reflects two factors: (i) partial loss of the *cis*-stilbene coating due to its limited volatility, which becomes relevant only under long, high-flow exposures and (ii) intrinsic differences in the reactivity of the halogen species toward the stilbene double bond. These experiments represent stress-test scenarios that exceed typical operational limits by a wide margin. UAV-based plume sampling rarely exceeds 10–20 min and flow rates are generally lower, making breakthrough under real field conditions unlikely.

The potential reactivity of *cis* -stilbene with hydrogen halides (HCl, HBr, HI), which occur in substantial concentrations in volcanic plumes, was also examined. Aqueous solutions (1 mL, 1 %) of each halide were evaporated under a nitrogen stream and passed through *cis*-stilbene-coated filters. No reaction products were detected, indicating that hydrogen halides do not interfere with or consume the coating under the tested conditions. Interference from other acidic gases such as HF is therefore considered unlikely, as HF is even less prone to electrophilic addition chemistry and was not tested explicitly for practical safety reasons.

Experiments with I_2, ICl and IBr likewise yielded no detectable stilbene derivatives. This is consistent with literature describing iodine-catalyzed *cis*-to-*trans* isomerization of stilbenes, where short-lived iodine addition products rapidly decompose to form trans-stilbene rather than stable di-iodinated molecules (Muizebelt and Nivard, 1965).

The brominated stilbene products exhibited notable thermal instability and degraded when analyzed using conventional split/splitless GC injection. For this reason, a programmed-temperature-vaporization (PTV) injection was required. In PTV mode, the solvent is removed before the analytes volatilize, which reduces thermal decomposition and preserves product integrity.

Recovery rates (Tab. 6) were measured by spiking known quantities of each target analyte onto blank filters, subjecting them to the complete extraction procedure and quantifying the resulting concentrations. These values were compared directly with reference solutions containing the same absolute analyte amounts. Combined recoveries for S-Cl_2, S-BrCl and S-Br_2 were 87 %, 92 % and 97 %, respectively, demonstrating that the extraction and analytical procedure provide robust and reproducible quantification across all derivatization products (Tab.6).

Table 6: Recovery rates (cis-stilbene products) for different amounts of analyte on syringe filters.

Method	Reaction product	Volumn [µL]	Concentration [µg/L]	Recovery rate [%]
Stilbene Filter	S-Cl_2 S-BrCl S-Br_2	200	50	85 ± 1 90 ± 1 96 ± 1
			750	89 ± 1 94 ± 1 98 ± 1

5.5.4 Performance of TMB-Coated Filters

TMB was evaluated using the same experimental strategy applied to *cis* -stilbene, with the addition that iodine was explicitly included because the electrophilic substitution of TMB by iodine species is well established. For this purpose, an iodine source was placed in the dilution-chamber feed together with the other halogens, enabling exposure of the coated filters to I_2 as well as to mixed halogen systems. As with *cis* -stilbene, the experiments were designed as stress tests, employing elevated flow rates, extended sampling durations and a wide humidity range to challenge the coating under conditions far more severe than typical UAV plume measurements.

TMB reacts via electrophilic aromatic substitution with halogen species in oxidation states 0 and +1 (Fig. 16). This includes Cl_2, Br_2, BrCl and I_2, all of which form stable halogenated TMB derivatives. In contrast to *cis* -stilbene, where limitations arise due to coating volatility and thermal sensitivity of the products, TMB coatings showed no measurable instability under the tested conditions. The reaction mechanism also differs fundamentally: *cis* -stilbene undergoes addition across the C=C bond, whereas TMB reacts through substitution on the aromatic ring, producing structurally stable products that resist thermal decomposition during analysis.

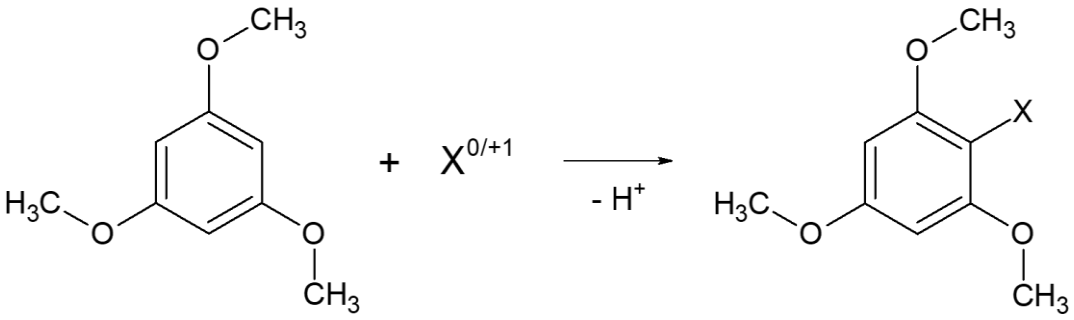

Figure 16: Reaction of TMB with halogen species (X) of oxidation state 0 and +1 yields the corresponding X–TMB adducts.

Across all tested conditions, including very low humidity (0 % RH, nitrogen atmosphere), high humidity (95 % RH, laboratory air) and prolonged high-flow exposures, collection efficiencies for Cl_2, Br_2, BrCl and I_2 were consistently above 99.9 %. These results, summarized in Table 5, demonstrate that TMB provides a robust and highly reactive coating for molecular halogens and interhalogens, complementing the *cis* -stilbene system.

Recovery rates (Tab. 7) were determined with the same procedure as for *cis* -stilbene filters with complete extraction process. Combined recovery rates were 87 % (Cl-TMB), 90 % (Br-TMB) and 95 % (I-TMB).

Table 7: Recovery rates (TMB products) for different amounts of analyte on syringe filters.

Method	Reaction product	Volumn [µL]	Concentration [µg/L]	Recovery rate [%]
TMB Filter	Cl-TMB Br-TMB I-TMB	200	50	82 ± 1 88 ± 1 97 ± 1
			750	92 ± 1 91 ± 1 92 ± 1

Possible reactions of TMB with hydrogen halides were examined in the same manner as for the *cis* -stilbene filters. As in the stilbene experiments, no reaction products were detected, confirming that halide acids (HCl, HBr, HI) do not interact with the TMB coating under the tested conditions.

In the context of volcanic plume chemistry, an additional question arises: could halogen radicals such as Br· or BrO· contribute to the formation of the observed TMB derivatives? To address this, TMB-coated filters were exposed to elemental bromine under controlled daylight and dark conditions. In darkness, bromine photolysis is suppressed and therefore no bromine radicals are produced, the resulting Br-TMB signals were consistently higher than under illuminated conditions. This clearly indicates that electrophilic substitution by molecular Br_2 is the dominant reaction pathway and that radical-driven reactions make no significant contribution.

This interpretation is further supported by mechanistic considerations. Radical substitution on aromatic systems such as TMB would be expected to occur preferentially at the methyl groups, leading to benzylic bromination and formation of R-CH_2Br species. No such products were observed in any experiment. Reactive uptake by BrO was also evaluated conceptually. However, generating controlled BrO concentrations in the laboratory is difficult and even if BrO were present, electrophilic aromatic substitution would be mechanistically disfavored because it

would require a hydroxyl radical to act as the leaving group. Such a pathway is not supported by known reaction kinetics or thermodynamics.

Combining these results demonstrate that the halogenated TMB products formed in these experiments arise exclusively from reactions with molecular halogens and interhalogens (Br_2, Cl_2, BrCl, I_2). Therefore, contributions from bromine radicals (Br·) or bromine oxide radicals (BrO·) to the analytical signals obtained with the TMB-based method can be excluded.

5.5.5 Detection Limits and Mixing Ratios for All Filter Systems

Detection limits for both filter types are summarized in Table 8. For stilbene filters, LODs ranged from 0.12 ng (BrCl) to 0.30 ng (Cl_2); TMB filters achieved similar sensitivities with LODs between 0.060 ng (I_2) and 0.16 ng (Br_2).

Table 8: Coated Filters: Determined LODs and LOQs in absolute amounts and in their mixing ratios at normal conditions using typical sampling conditions, flow 250 mL min^{-1}, sampling time 15 min at 1 atm.

	Stilbene-Filter			TMB-Filter		
Limit	**Cl_2**	**BrCl**	**Br_2**	**Cl_2**	**Br_2**	**I_2**
LOD (pg)	0.30	0.12	0.19	0.094	0.16	0.060
LOD (pptv)	7.1	2.7	3.3	2.2	3.7	1.1
LOQ (pg)	0.90	0.35	0.56	0.28	0.48	0.18
LOQ (pptv)	21	8.0	9.8	6.7	11	3.2

For typical UAV sampling (250 mL min^{-1}, 15 min), these values correspond to:

Cl_2: 7.1–21 pptv

BrCl: 2.7–8.0 pptv

Br_2: 3.3–9.8 pptv

I_2: 1.1–3.2 pptv

These detection limits represent a 1–2 orders of magnitude improvement over previously published denuder systems and enable detection of reactive halogen species at concentrations typical of ageing volcanic plumes; these Field measurements of reactive bromine species using TMB-based sampling at Mt Etna have reported mixing ratios in the low-ppbv range (Rüdiger et al., 2017). The pptv detection limits achieved are therefore well below concentrations observed close to the vent and demonstrate sufficient sensitivity for near-source plume conditions.

For other molecular halogen species targeted by the *cis* -stilbene filters, quantitative concentration data in volcanic plumes are generally scarce. The achieved detection limits indicate that these species can be addressed across a wide range of plume conditions, although interpretation of absolute mixing ratios remains challenging due to strong spatial and temporal variability and plume dilution during UAV-based sampling.

5.6 Conclusions

The suite of methods developed and evaluated in this study provides a coherent analytical framework for quantifying total halogen and sulfur species as well as speciated molecular halogens in volcanic plumes, with particular emphasis on UAV-based sampling. Each component of the workflow was optimized with respect to rapid analyte enrichment, low mass, short sampling durations and high analytical sensitivity, enabling robust deployment under the operational constraints of UAV platforms.

The alkaline trap represents a miniaturized alternative to classical impingers, specifically engineered to reduce sample volume, handling effort and instrument payload while maintaining quantitative absorption performance. Stress-test experiments in a controlled dilution chamber demonstrated near-complete uptake of both weak and strong acidic gases (CO_2, SO_2), confirming that hydrogen halides (HF, HCl, HBr) are collected with effectively quantitative efficiency. Oxidation with H_2O_2 and neutralization via cation-exchange resin were shown to preserve analyte integrity, yielding recoveries of 95 ± 5 % across all species. Once neutralized, samples remained chemically stable, whereas freshly prepared alkaline solutions were required to avoid storage-related artefacts. Absolute detection and quantification limits were 0.022 and 0.066 µg for HF, 0.62 and 1.9 µg for HCl, 0.011 and 0.034 µg for HBr and 0.51 and 1.5 µg for SO_2, corresponding to sub-ppb to mid-ppb mixing ratios under typical UAV sampling (250 mL min^{-1}, 15 min). These values are well suited for near-vent environments such as Mt Etna.

For speciated molecular halogens, *cis* -stilbene-coated syringe filters were developed to target chlorine, bromine and interhalogen species such as BrCl. Dilution chamber experiments, designed intentionally as extreme stress tests, confirmed reaction yields above 99.9 %, despite known challenges such as coating volatility and product

thermolability. *Cis* -stilbene coatings were unaffected by hydrogen halides (HCl, HBr, HI) and no iodinated products were observed, consistent with literature describing rapid iodine catalyzed *cis–trans* isomerization. To preserve the integrity of the thermally labile brominated products, PTV injection was required. Combined recoveries for S-Cl_2, S-BrCl and S-Br_2 were 87 %, 92 % and 97 %, respectively. The absolute detection and quantification limits were 0.30 and 0.90 ng for Cl_2, 0.12 and 0.35 ng for BrCl and 0.19 and 0.56 ng for Br_2

TMB-coated syringe filters provided a complementary derivatization pathway targeting halogens in oxidation states 0 and +1 via electrophilic aromatic substitution. The TMB method was evaluated using the same experimental design as for *cis* -stilbene, including additional tests with iodine species since their reaction with TMB is well characterized. Collection efficiencies consistently exceeded 100 % for Cl_2, Br_2, BrCl and I_2 across variations in humidity, flow rate and exposure duration. In contrast to *cis* -stilbene, TMB coatings and products showed high thermal stability and no measurable degradation under the tested analytical conditions. Systematic tests ruled out contributions from radical bromine species (Br· or BrO·): photolysis experiments yielded lower Br-TMB signals under illuminated conditions than in darkness and no radical-type benzylic bromination products (R-CH_2Br) were detected. The absolute detection and quantification limits achieved for TMB-coated filters were 0.094 and 0.28 ng for chlorine, 0.16 and 0.48 ng for bromine and 0.060 and 0.18 ng for iodine.

Together, the alkaline trap and the two coated-filter methods form a robust, UAV-compatible analytical system for volcanic plume research. The alkaline trap enables precise quantification of total halogen and sulfur budgets, while the *cis* -stilbene and TMB filters allow selective identification and quantification of reactive molecular halogens across several oxidation states. This integrated methodology substantially enhances the ability to characterize volcanic halogen chemistry, evaluate halogen activation pathways and derive ratios such as BrCl/Br and Br/S under realistic plume conditions.

Several limitations of the methods presented should be considered. Brominated stilbene reaction products exhibit pronounced thermal sensitivity, which necessitates mild injection conditions such as programmed-temperature vaporization and

represents an analytical constraint. The coated filter systems are selective and differ in their chemical scope. *Cis* -stilbene selectively traps molecular halogens and interhalogens while other halogen species are not retained. TMB reacts with halogen species in oxidation states 0 and +1; however, the exact reaction pathways and potential contributions from other reactive halogen species could not be independently verified. Radical halogen species are not actively trapped by either coating and may therefore contribute to the overall halogen budget without being reflected in the speciation results. Furthermore, UAV-based sampling is inherently limited in sampling duration and spatial coverage. Volcanic plumes are often highly heterogeneous in space and time and the measured concentrations therefore represent local plume snapshots rather than fully integrated plume compositions.

6 UAV-based measurements at Mt. Etna

6.1 Flight strategy and on-drone sampling system

Three UAV-based measurement campaigns were conducted at Mt. Etna in July 2022, June 2023 and September 2023. The July 2022 campaign was accompanied by minor strombolian activity and elevated degassing, while the subsequent campaigns were conducted during periods of passive, steady gas emission under moderate seismic conditions (INGV, 2022-2023). In all campaigns, the volcanic plume typically originated from the Bocca Nuova and Southeast Craters, with a focus on sampling the Bocca Nuova plume due to its consistent and concentrated output.

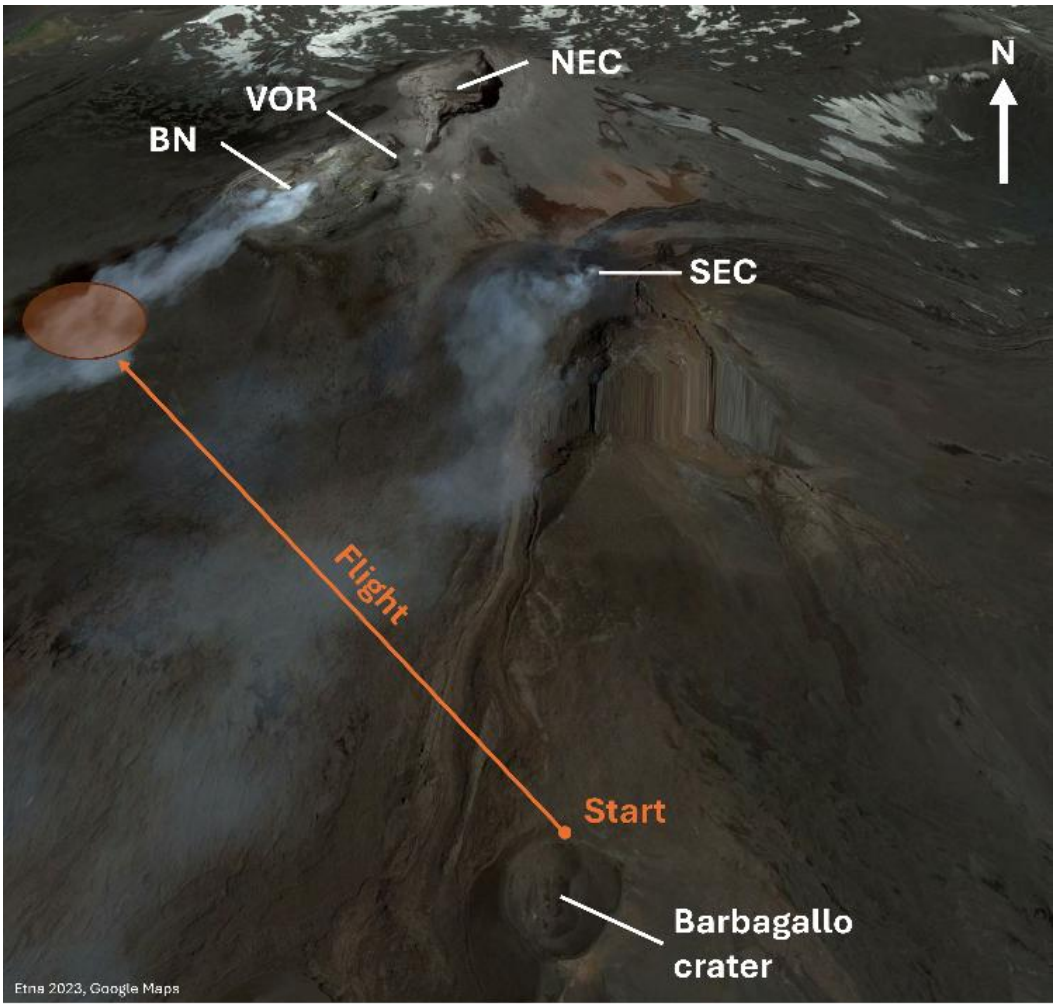

Figure 17: Flight site, with typical UAV flight from Barbagallo crater rim to Bocca Nuova (BN) plume. NEC = North east crater, SEC = South east crater, VOR = Voragine; Source: Google Maps.

UAV flights were primarily launched from the northern rim of Barbagallo Crater (N 37.736131, E 15.000249) (Fig. 17), a site offering clear line-of-sight to the active vents. The plume was located and tracked in real time using a compact onboard SO_2

sensor. Visual telemetry and live gas concentration data were used to guide the UAV into the core of the plume. During sampling, the UAV maintained a consistent downwind distance from the vent to enable the sampling of gas parcels of defined and comparable age. Typical flight durations ranged from 25 to 30 minutes, with in-plume sampling lasting approximately 15 to 20 minutes per flight. Positioning was determined using GPS data and Google Earth, while wind data was recorded by the UAV's internal software. The plume age was derived from GPS positioning, wind speed data provided by the drone and additional manual time measurements. These manual time estimations were performed using a wristwatch by tracking the movement of visible gas structures in the plume on the onboard camera footage. Distinct emission events or gas puffs were visually followed to estimate the transport time between emission and sampling position.

6.2 Analytical methods and data processing

To quantify halogen and sulfur species in the volcanic plume, three complementary derivatization and absorption methods were applied using a UAV-based sampling platform. The analytical setup consisted of an alkaline trap (NaOH bubbler) for total halogens and sulfur, a *cis*-stilbene filter for selective detection of molecular halogens (Cl_2, Br_2, BrCl) and a TMB filter for unspecific reactive halogen species (ClX, BrX, IX).

All sampling and analytical procedures, including preparation, extraction and chromatographic analysis, followed the protocols described previously in section 5. In brief, acidic gas-phase species were collected by chemical absorption or electrophilic addition reactions, stabilized on the respective collection media and subsequently analyzed by ion chromatography (IC) or gas chromatography coupled with high-resolution mass spectrometry (GC-HRMS).

The alkaline trap provided total halogen and sulfur concentrations through the quantitative absorption of acidic gases (e.g., HF, HCl, HBr, SO_2) in sodium hydroxide, with resulting products determined as halide and sulfate ions by ion chromatography. The *cis*-stilbene filters selectively captured molecular halogens via di-halogen addition, while TMB-coated filters trapped a broader range of reactive halogen intermediates. Together, these methods yield complementary information on total, molecular and reactive halogen species and form the analytical basis for the datasets presented in this study.

All halogen species were normalized to the total sulfur content obtained from the alkaline trap, allowing for dilution-independent comparison of halogen-to-sulfur ratios. This normalization enables the direct interpretation of halogen chemistry as a function of plume age and mixing state. These combined data facilitate the interpretation of halogen oxidation dynamics in the early plume and support the identification of halogen formation pathways and precursor–product relationships.

6.3 Measurement Data and Interpretation of Halogen/Sulfur Ratios

In 2022, eleven measurement points were made between 20 and 5300 m downwind of the vent, corresponding to approximately 0.1 – 32 min after emission. In 2023, seven measurements were collected between 140 and 860 m, corresponding to 0.5-2.8 min after emission. Thus, the later plume stages (> 3 min) were only covered in 2022. Volcanic activity was slightly elevated in 2023 compared to 2022. The Cl/S ratios remained relatively stable across both years, whereas Br/S and likely I/S showed substantial interannual differences, with significantly higher values in 2022. Bromine was quantifiable in eight out of nine samples in 2022, whereas in 2023 bromine fell below the detection limit in four of eight samples, reflecting the generally lower halogen abundance in that year. While absolute Cl/S ratios ranged from 0.14–3.1 (2022) and 0.7–4.3 (2023), Br/S ratios were significantly higher in 2022 (25–47 $\times 10^{-4}$) than in 2023 (7–9 $\times$ 10^{-4}).

Tables 9a and b summarize the results of ion chromatographic measurements of total halogens and sulfur from alkaline trap solutions for 2022 and 2023, respectively. The listed concentrations refer to standard conditions for air, as the exact dilution by entrained ambient air during sampling could not be quantified.

Table 9 a and b: Results for total halogens from IC measurements of alkaline solutions in 2022 (a) and 2023 (b). The specified time refers to the visual emission of volcanic gases from the vent. The concentration data for halogens and sulfur refer to the alkaline solution. The actual concentration in the volcanic plume cannot be measured because unknown quantities of ambient air were sampled. N.d. = not detectable, time estimation was impossible due to weather conditions. < LOD = below detection limit.

a)

Time [min]	F [nmol/L]	Cl [µmol/L]	Br [nmol/L]	Sulfur [µmol/L]	F/S	Cl/S	Br/S x10^{-4}
0.33	<LOD	0.0989 ± 0.005	0.140 ± 0.01	0.0353 ± 0.001	-	2.8 ± 0.1	39 ± 2.0
0.55	32.5 ± 1.6	0.624 ± 0.03	0.873 ± 0.04	0.306 ± 0.006	0.11 ± 0.01	2.0 ± 0.1	29 ± 1.4
0.75	47.7 ± 2.4	0.0973 ± 0.005	0.625 ± 0.03	0.253 ± 0.005	0.19 ± 0.01	0.38 ± 0.02	25 ± 1.2
1.9	21.0 ± 1.1	0.0146 ± 0.001	0.360 ± 0.02	0.102 ± 0.002	0.21 ± 0.01	0.14 ± 0.01	35 ± 1.8
1.3	25.7 ± 1.3	0.0353 ± 0.002	0.457 ± 0.02	0.113 ± 0.002	0.23 ± 0.01	0.31 ± 0.02	40 ± 0.2
6.0	17.0 ± 0.9	0.0644 ± 0.003	0.228 ± 0.01	0.0485 ± 0.001	0.35 ± 0.02	1.3 ± 0.1	47 ± 2.3
3.4	24.4 ± 1.2	0.335 ± 0.02	0.296 ± 0.01	0.107 ± 0.002	0.23 ± 0.01	3.1 ± 0.2	28 ± 1.4
31.8	23.2 ± 1.2	0.152 ± 0.01	<LOD	0.0572 ± 0.001	0.40 ± 0.02	2.7 ± 0.1	-
0.90	31.9 ± 1.6	0.190 ± 0.01	0.726 ± 0.04	0.156 ± 0.003	0.20 ± 0.01	1.2 ± 0.1	47 ± 2.3
7.7	19.2 ± 1.0	0.117 ± 0.01	0.186 ± 0.01	0.0583 ± 0.001	0.33 ± 0.02	2.0 ± 0.1	32 ± 1.6

b)

Time [min]	F [nmol/L]	Cl [µmol/L]	Br [nmol/L]	Sulfur [µmol/L]	F/S	Cl/S	Br/S x10^{-4}
1.0	83.3 ± 4.2	0.945 ± 0.05	0.990 ± 0.05	1.34 ± 0.03	0.062 ± 0.003	0.71 ± 0.04	7.4 ± 0.4
0.52	116 ± 6	0.887 ± 0.04	<LOD	0.559 ± 0.01	0.21 ± 0.01	1.6 ± 0.1	<LOD
n.d.	197 ± 10	3.24 ± 0.2	0.961 ± 0.05	1.11 ± 0.02	0.18 ± 0.01	2.9 ± 0.1	8.7 ± 0.4
1.4	164 ± 8	1.66 ±0.1	1.40 ± 0.07	1.74 ± 0.03	0.094 ± 0.005	0.95 ± 0.05	8.0 ± 0.4
2.8	113 ± 6	2.71 ± 0.1	<LOD	0.743 ± 0.02	0.15 ± 0.01	3.6 ± 0.2	<LOD
1.7	64.7 ±3.2	2.43 ± 0.1	<LOD	0.917 ± 0.02	0.071 ± 0.004	2.6 ± 0.1	<LOD
2.3	162 ±8	3.78 ± 0.2	<LOD	0.871 ± 0.02	0.19 ± 0.01	4.3 ± 0.2	<LOD

6.4 Halogen speciation in volcanic plumes – UAV-Measurements at Mt. Etna in 2022 and June 2023

During this campaign, chlorine (Cl_2), bromine (Br_2), bromine chloride (BrCl), RHS of undefined molecular form (ClX, BrX, IX) as well as total halogen (F, Cl, Br) and sulfur were quantified. The measurements focused on the evolution of halogen speciation in relation to plume age. Linking reactive halogen abundance to plume age and volcanic activity could improve the understanding of oxidation kinetics and the formation pathways of short-lived halogen species in early volcanic plumes.

To investigate the chemical evolution of halogen species in the volcanic plume time-resolved data collected during UAV-based sampling flights at Mt. Etna in 2022 and 2023 was analyzed. During each flight, all halogen species were measured simultaneously with total sulfur via the alkaline trap. The live data of the SO_2 sensor was used to confirm plume presence and flight positioning but not for quantitative evaluation, as high concentrations within the core plume led to sensor saturation.

Each sampling unit was operated by a remotely controlled pump, allowing precise timing of sample intake during plume encounters. GPS data were used to record flight altitude, distance from the vent and flight trajectory, while wind speed data from UAV onboard sensors were used to estimate the plume age of sampled gas parcels.

6.4.1 Temporal evolution of halogen species

To illustrate the temporal evolution of halogen species in the volcanic plume, the normalized ratios of individual halogen compounds to sulfur (X/S, Tab.10) are plotted as a function of time after emission (Fig. 18). The data combines measurements from both campaigns in 2022 and 2023 and represents total and reactive halogen species derived from filter and bubbler analyses. This visualization highlights the rapid near-vent activation of bromine, the comparatively lower oxidation of chlorine and the faster decline of reactive halogen species, especially iodine, in later stages. In the following sections, these trends are described for bromine, chlorine and iodine, respectively.

Table 10a and b: Results for halogen species, normalized to sulfur and additional results for RHS BrX and ClX normalized to their total halogen content 2022 and 2023. <LOD = below limit of detection; n.d. = not detected because of malfunction of the pump, the system or unable to determine the wind speed and emission time. Error values are 20% for time estimation.

a)

Time [min]	Cl_2/S [10^{-6}]	BrCl/S [10^{-6}]	Br_2/S [10^{-6}]	ClX/S [10^{-6}]	BrX/S [10^{-6}]	IX/S [10^{-6}]	S [mol/L] [10^{-6}]	BrX/ Br	ClX/Cl [10^{-3}]
0.10	2.4 ± 0.4	11 ± 2	0.76 ± 0.12	n.d.	n.d.	n.d.	0.179	n.d.	n.d.
0.33	n.d.	n.d.	n.d.	270 ± 40	300 ± 50	2.9 ± 0.5	0.0353	0.076 ± 0.013	0.097 ± 0.016
0.55	5.3 ± 0.8	9.3 ± 1.5	1.2 ± 0.2	220 ± 40	460 ± 70	17 ± 3	0.306	0.16 ± 0.03	0.11 ± 0.02
0.75	7.9 ± 1.3	56 ± 9	4.6 ± 0.7	300 ± 50	1000 ± 200	27 ± 4	0.253	0.42 ± 0.07	0.78 ± 0.13
1.9	59 ± 9	44 ± 7	4.1 ± 0.7	2600 ± 400	3500 ± 600	67 ± 11	0.102	0.98 ± 0.17	18 ± 3
1.3	74 ± 12	260 ± 40	19 ± 3	2200 ± 300	3100 ± 500	76 ± 12	0.113	0.76 ± 0.13	7.1 ± 1.2
6.0	15 ± 2	59 ± 9	1.9 ± 0.3	1200 ± 200	890 ± 140	8.8 ± 1.4	0.0458	0.19 ± 0.03	0.92 ± 0.15
6.0	16 ± 3	55 ± 9	1.4 ± 0.2	1200 ± 200	890 ± 140	8.8 ± 1.4	0.0458	0.19 ± 0.03	0.92 ± 0.15
3.4	30 ± 5	45 ± 7	1.2 ± 0.2	900 ± 100	1200 ± 190	22 ± 4	0.107	0.45 ± 0.08	0.29 ± 0.05
32	12 ± 2	15 ± 2	2.0 ± 0.3	500 ± 80	310 ± 50	0.64 ± 0.10	0.0572	<LOD	0.19 ± 0.03
0.90	28 ± 4	180 ± 30	22 ± 4	1000 ± 170	3700 ± 600	71 ± 11	0.156	0.80 ± 0.14	0.86 ± 0.14
7.7	7.1 ± 1.1	67 ± 11	1.8 ± 0.3	1400 ± 200	900 ± 140	6.8 ± 1.1	0.0583	0.28 ± 0.05	0.70 ± 0.11

b)

Time [min]	Cl_2/S [10^{-6}]	BrCl/S [10^{-6}]	Br_2/S [10^{-6}]	ClX/S [10^{-6}]	BrX/S [10^{-6}]	IX/S [10^{-6}]	S [mol/L] [10^{-6}]	BrX/ Br	ClX/Cl [10^{-3}]
1.00	18 ± 3	9.1 ± 1.4	<LOD	270 ± 40	200 ± 30	4.3 ± 0.7	1.34	0.27 ± 0.05	0.38 ± 0.06
0.52	2.8 ± 0.4	0.29 ± 0.05	<LOD	44 ± 7	23 ± 4	0.75 ± 0.12	0.559	0.029 ± 0.005	0.028 ± 0.005
n.d.	58 ± 9	6.0 ± 1.0	0.14 ± 0.02	190 ± 30	200 ± 30	2.6 ± 0.4	1.11	0.23 ± 0.04	0.063 ± 0.010
1.4	140 ± 20	25 ± 4	2.2 ± 0.4	590 ± 90	650 ± 103	12 ± 2	1.74	0.81 ± 0.14	0.62 ± 0.10
2.8	1.9 ± 0.3	0.12 ± 0.02	<LOD	330 ± 50	220 ± 35	3.3 ± 0.5	0.743	0.28 ± 0.05	0.092 ± 0.015
1.7	5.9 ± 0.9	0.23 ± 0.04	<LOD	710 ± 100	660 ± 105	13 ± 2	0.917	0.82 ± 0.14	0.27 ± 0.04
2.3	1.0 ± 0.2	0.066 ± 0.010	<LOD	360 ± 60	320 ± 50	3.5 ± 0.5	0.871	0.40 ± 0.07	0.083 ± 0.014

Figure 18 shows sulfur-normalized mixing ratios of measured halogen species (X/S) as a function of plume age for two field campaigns conducted in 2022 and 2023. Normalization to sulfur is used to account for dilution effects and to enable direct comparison between species and campaigns. For clarity, individual data points are shown without uncertainty bars; measurement uncertainties are discussed summarized in Table 10.

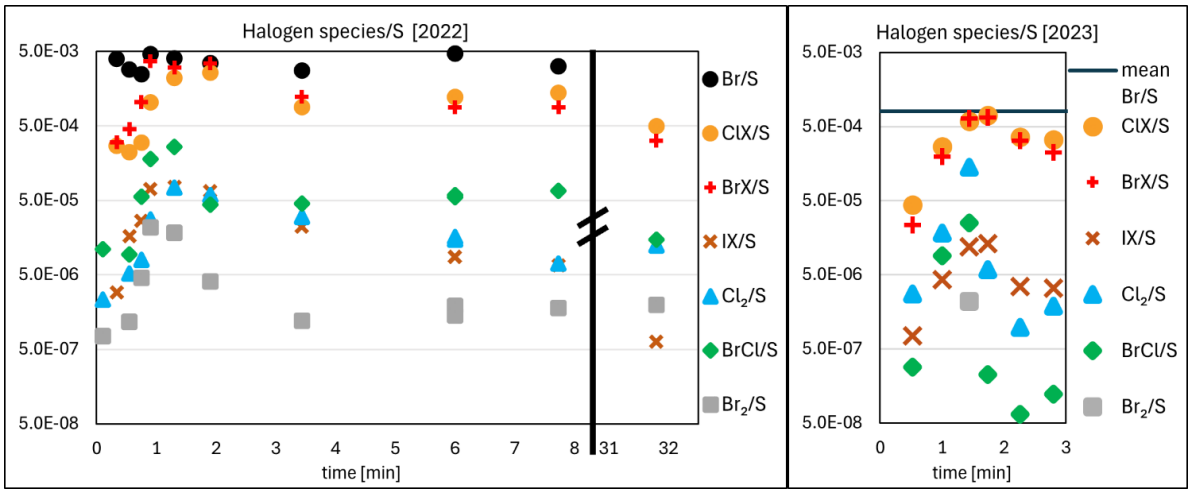

Figure 18: Temporal evolution for halogen species during two Etna campaigns in 2022 and 2023, in 2023 the mean value of Br/S is shown due to limited data.

Bromine

Close to the vent, within the first minutes after emission, bromine was rapidly activated in both years. In 2022, BrX/S increased steeply within 0.5–2 min plume age to values between 3.0×10^{-4} and 3.5×10^{-3} whereas in 2023 values were lower, ranging between 2.3×10^{-5} and 6.6×10^{-4} (Fig. 19a). After reaching a maximum at approximately 2 min plume age, the measured BrX/S signal in 2022 decreased with further plume aging. This decrease reflects a reduction in the detectable BrX signal relative to sulfur.

A consistent behavior is observed in the BrX/Br ratio, which reached values of up to 0.98 in 2022 and approximately 0.8 in 2023 (Fig. 19b). In 2022, BrX/Br likewise decreased after ~2 min plume age, indicating that an increasing fraction of bromine was no longer captured in the measured BrX signal.

Halogen and interhalogen species were detected in both years, but their contribution to total bromine remained small compared to BrX. In 2022, BrCl/Br ranged between 0.003 and 0.065, while Br_2/Br was $\leq$ 0.005, indicating that Br_2 and BrCl together represented only a minor fraction of total bromine (Fig. 19c). Following the decline in BrX/Br after ~2 min plume age in 2022, the individual detectable bromine species normalized to total bromine also decreased, demonstrating that the reduction affects the complete measurable bromine pool rather than a single compound class.

In 2023, the same qualitative pattern was observed close to the vent; however, the dataset is restricted to the near-source region. Measurements in that year were intentionally focused on young plumes, and no observations were obtained at plume ages beyond approximately 3 min. This limitation reflects sampling constraints, primarily due to meteorological conditions, rather than insufficient analytical sensitivity. Consequently, the evolution of BrX at later plume ages in 2023 cannot be assessed quantitatively. BrCl decreased noticeably over the observed plume lifetime in 2023, while remaining relatively constant in 2022 (Fig. 19d).

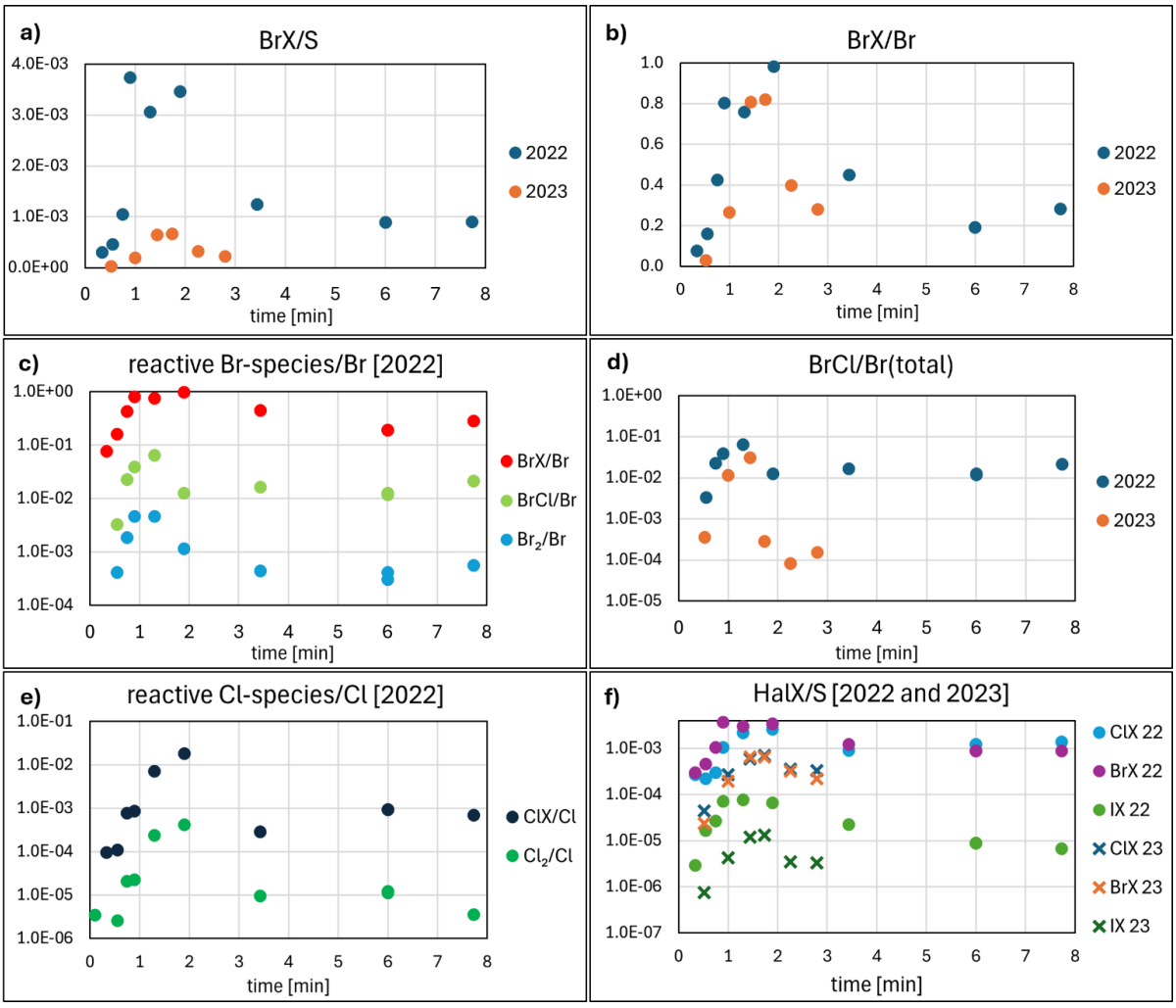

Figure 19a-f: Different time resolving plots of halogen oxidation with interannual comparison.

Chlorine

Chlorine activation was far less efficient than bromine activation. Similar to bromine, molecular chlorine represented only a very minor fraction of total chlorine, with Cl_2/Cl(total) not exceeding ~4.2 × 10^{-4} (Fig. 19e). Furthermore, Cl_2 accounted for only about 2 % of the total reactive chlorine (ClX) signal, indicating that most of reactive chlorine species were present in other oxidized forms. Both years showed Cl_2/S ratios of similar order, although the temporal peaks occurred at different plume ages. Overall, oxidized halogen-to-sulfur ratios were lower in 2023, consistent with reduced bromine and iodine abundances. Chlorine activation remained consistently weak in both years and largely independent of its total abundance relative to sulfur. However, a clear interannual difference was observed: in 2022, ClX/Cl(total) reached up to 1.8 %, whereas in 2023 the maximum remained below 0.1 % (Fig. 19f). Despite similar Cl(total)/S ratios between the two years, this indicates that chlorine oxidation

was markedly less efficient in 2023, while bromine activation proceeded nearly complete in both campaigns.

Iodine

Iodine, detected as IX/S, mirrored the early increase of BrX/S but at lower absolute levels. In 2022 the IX/S maxima was (6-8)×10^{-5} during the first ~2 min, while in 2023 the maximum reached only ~1.3×10^{-5} and at later plume ages (≥ 6 min; covered only in 2022), BrX/S and ClX/S decreased by roughly one order of magnitude, whereas IX/S decreased by nearly two orders of magnitude while in 2023, a decline in BrX/S, ClX/S and IX/S with plume age was also observed, though less pronounced due to the shorter distance range covered (Fig. 19f). The datasets therefore complement each other, with the 2022 measurements extending further downwind and showing the progressive decrease more clearly. Although the 2023 measurements did not extend far enough downwind to resolve the decay phase, the consistent initial IX/S maxima and BrX–IX co-variability indicate that iodine activation follows similar early-plume dynamics as bromine. Ratios at the times of maximum halogen activation highlight the interannual contrast in total halogen abundance:

$$(BrX/S)_{2022} / (BrX/S)_{2023} \approx 5.7 \quad \text{Eq. 27}$$

$$(IX/S)_{2022} / (IX/S)_{2023} \approx 5.8 \quad \text{Eq. 28}$$

These differences reflect the generally higher halogen-to-sulfur ratios in 2022, as confirmed by alkaline trap measurements of Br/S. The lower IX/S in 2023 likely reflects reduced total iodine content, although total iodine could not be quantified directly.

6.4.2 Discussion

The discussion in the following sections is based on time-resolved UAV measurements that provide short but direct in-plume observations of volcanic halogens. Although each individual flight captures only a few minutes of plume evolution, the campaigns in 2022 and 2023 independently exhibit the same key features in halogen speciation and activation. This consistency demonstrates that the central observations—namely rapid near-source bromine activation and the dominance of BrX shortly after emission—are reproducible across years.

Small-scale fluctuations in absolute concentrations and derived ratios are nevertheless observed within individual flights. These variations could be attributed to natural plume heterogeneity, including turbulent mixing, wind-driven displacement, and UAV movement between denser plume cores and more dilute edge regions, rather than to systematic differences in plume chemistry. Despite efforts to position the UAV as deeply as possible within the plume, variations in wind speed, thermal updrafts, and spatial gradients in plume density inevitably influence the measured concentration profiles. Consequently, the derived temporal evolution of reactive halogen species should be interpreted as representing the range of plume chemistry encountered under near-source conditions, rather than as strictly time-resolved kinetics at a fixed spatial point.

Despite these limitations, consistent patterns across multiple flights and both campaign years indicate that the observed temporal trends are robust. The following discussion therefore focuses on identifying the dominant chemical processes governing the rapid activation, transformation and decay of halogen species within the first minutes after emission.

Rapid Oxidation of Halogens in Volcanic Plumes

Halogens in volcanic gases undergo rapid oxidation within the first minutes after emission. In both campaigns, HBr oxidation progressed very quickly and BrX reached its maximum at approximately two minutes of plume age. The similar rise rates of BrX relative to Br(total) in 2022 and 2023 show that the apparent reaction timescale is largely independent of the initial bromine concentration. This observation indicates pseudo-first-order behavior controlled mainly by how fast ambient air is entrained into the plume rather than by intrinsic chemical rate constants.

The most likely oxidants are OH and HO_2, which initiate the early gas-phase conversion of HBr into oxidized bromine through the familiar reaction chain:

$$HBr + OH \rightarrow Br + H_2O \quad \text{Eq. 29}$$

$$Br + O_3 \rightarrow BrO + O_2 \quad \text{Eq. 30}$$

$$HO_2 + HBr \rightarrow HOBr + H_2O \quad \text{Eq. 31}$$

$$BrO + HO_2 \rightarrow HOBr + O_2 \quad \text{Eq. 32}$$

The efficient formation of HOBr explains why BrX clearly dominates over Br_2 and BrCl at early plume age. HOBr reacts with TMB and is therefore included in the BrX signal, whereas Br radicals are not detected and Br_2 or BrCl are only captured by the *cis* -stilbene filter. The comparatively low Br_2, BrCl and Cl_2 signal indicates that heterogeneous activation plays only a minor role during the first minutes of plume evolution and that gas-phase oxidation of HBr to HOBr is the dominant early pathway.

Although HBr is not measured directly, the strong anti-correlation between BrX and the remaining non-BrX bromine fraction suggests that HBr and BrX together represent most of Br(total) during the earliest phase. Contributions from radical species such as BrO are expected to be small at this stage, based on the established understanding that BrO is a secondary, photochemically produced species that tends to peak later in the plume (Bobrowski and Giuffrida, 2012). The overall behavior is consistent with the kinetic picture proposed by Nies et al. (2025), in which HO_x produced during high-temperature air entrainment initiates rapid HBr oxidation that continues as the plume cools.

The high-temperature part of the Nies et al. 2025 model offers additional insight (Fig. 20 left). For the first ten seconds after emission, the simulations show the strongest HBr oxidation at 1323 K, slightly weaker but still efficient oxidation at 1123 K and substantially slower oxidation at 923 K. The measurements, however, begin at approximately 0.1 min after visual confirmation of plume release rather than modelled emission time directly above the magma reservoir and therefore do not directly resolve this initial high-temperature regime. The observed exponential increase in BrX/HBr allows a rough back-extrapolation toward earlier times, which should be interpreted as indicative rather than as a direct constraint on the immediate post-degassing chemistry, given the unknown temporal offset between magma degassing and plume visibility. This approximation suggests that in 2022 the inferred Br(oxidized)/HBr ratio lies below the 1123 K trajectory but above the 923 K case, whereas in 2023 the inferred ratio falls even below the 923 K case. These relative differences correspond to the distinct initial BrX/HBr values observed in the two years and may reflect differences in source temperature, degassing intensity or melt composition (Fig. 20 right).

A slightly higher effective magmatic temperature during the 2022 activity, or differences in degassing intensity or melt composition, could shift halogen partitioning toward a larger initial gas-phase bromine fraction. Although these interpretations remain tentative without direct magmatic measurements, the alignment between observational differences and modelled temperature sensitivity suggests that variations in vent conditions influenced the early bromine oxidation behavior between the two campaigns.

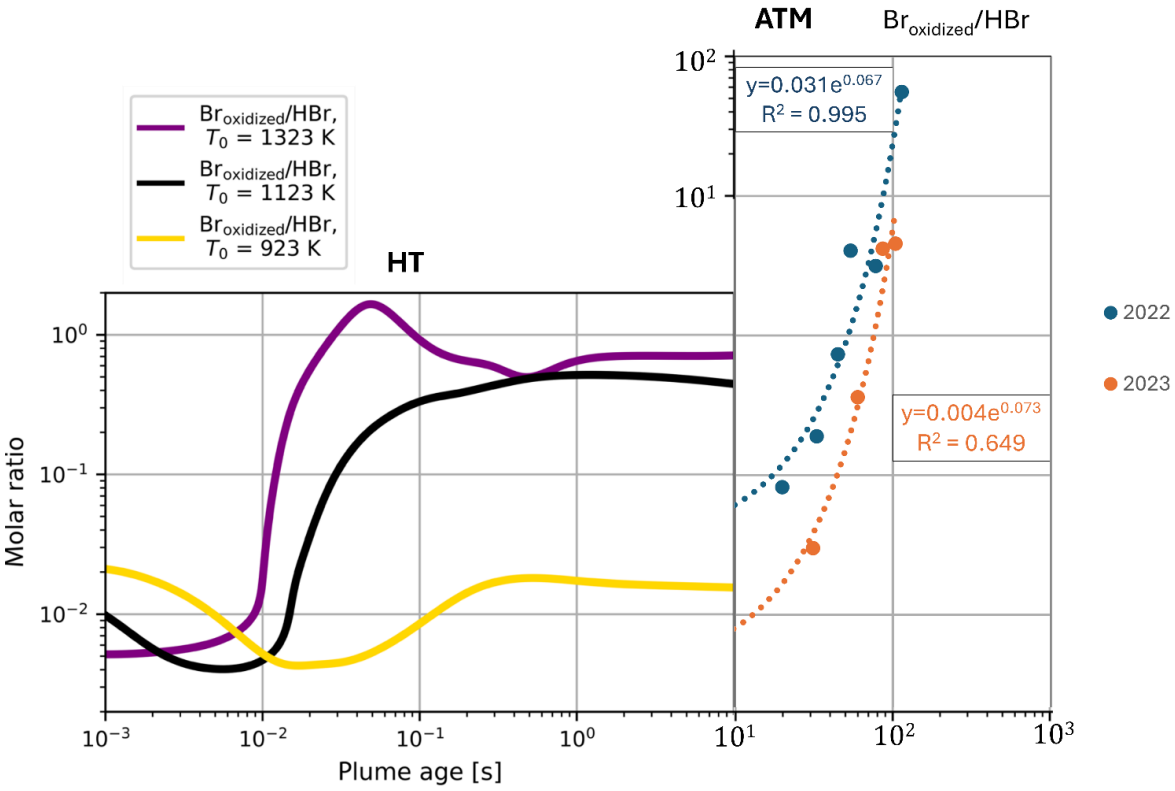

Figure 20: Comparison of the high-temperature (HT) bromine oxidation model of Nies et al. (2025) for initial temperatures of 923, 1123 and 1323 K (left) with atmospheric measurements (ATM) of $Br_{oxidized}$/HBr at Mt. Etna during the 2022 and 2023 campaigns (right), highlighting the continuation of bromine oxidation from the high-temperature regime into the atmospheric plume and the correspondence between the 1123 K model case and the observed oxidation trends.

The atmospheric model of Nies et al. (2025) explored bromine oxidation for three initial temperatures (923, 1123 and 1323 K). Among these simulations, the 1123 K case produced the fastest HBr oxidation within the modelled parameter space. Importantly, this simulation also provides an explicit time axis: at 1123 K, HBr is almost completely consumed after roughly three minutes of plume evolution (Fig. 21 left). The measurements show a maximum of BrX relative to Br(total) at around two minutes. The model and the observations therefore converge on a similar timescale, with the measurements suggesting slightly faster conversion (Fig 21 right). Despite

differences in model geometry, mixing assumptions and the definition of oxidized bromine, both indicate that the bulk of HBr is oxidized within only a few minutes after emission.

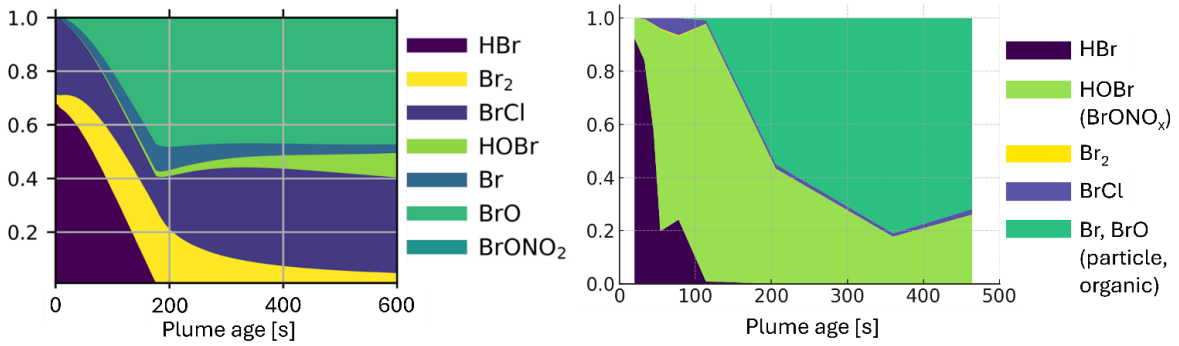

Figure 21: Comparison of bromine speciation as a function of plume age between the atmospheric chemistry model of Nies et al. (2025) for an initial temperature of 1123 K (left) and ground-based measurements at Mt. Etna (right), showing the temporal evolution of HBr and oxidized bromine species and illustrating comparable oxidation timescales within the first few minutes after emission.

The model, however, produces higher early fractions of Br_2 and BrCl than inferred from the observations. In the available data, the BrO fraction appears delayed and remains low during the BrX maximum. After this point, the decline of BrX suggests a shift in bromine partitioning toward radicals and interhalogens rather than re-formation of HBr. This behavior is consistent with a gradual transition from HOBr-dominated early oxidation to a regime in which BrO, bromine radicals, and multiphase recycling increasingly control bromine speciation.

Overall, while differences in absolute speciation exist between the model and the measurements, both agree on the central conclusion: most of the emitted HBr is oxidized within the first few minutes of plume evolution and the earliest bromine chemistry is highly sensitive to the initial thermal and compositional conditions of the volcanic gas.

The results of this study complement earlier UAV-based observations of reactive halogens in volcanic plumes. (Rüdiger et al., 2018) investigated near-vent chemistry at Masaya volcano using a similar TMB derivatization technique combined with model simulations of bromine activation. Although their measurements did not directly quantify Br_2 or BrCl, they observed rapid bromine activation and their model suggested that Br_2 constituted a major fraction of total bromine. This contrasts with the present Etna results, where both Br_2 and BrCl represent only minor components of total reactive bromine and BrX clearly dominates. The discrepancy may reflect

differences in model assumptions and parameterizations rather than true compositional variations, as uncertainties in heterogeneous uptake coefficients can influence predicted Br_2 and BrCl abundances. Similar model tendencies toward elevated Br_2 and BrCl have been reported in previous studies (Roberts et al., 2009; Roberts et al., 2014). Rüdiger et al. further reported no detectable decay of reactive halogens with plume age, although their measurement uncertainties would allow for such a trend. One UAV data point indicated a possible transient BrX maximum, but the authors interpreted it cautiously due to short sampling duration and the limited sensitivity of the SO_2 sensor.

At Masaya, (Gutmann et al., 2021) measured HBr and HCl using UAV-borne derivatization techniques and reported rapid HBr depletion with distance from the vent, implying fast near-vent oxidation consistent with the presented measurements. The bulk halogen ratios (Br/S $\approx 10^{-4}$–10^{-2}) reviewed by (Gutmann et al., 2018) for Mt. Etna provide a useful reference framework. The 2022 data indicate comparatively high bromine levels that remain within the range of earlier Etna measurements, while 2023 values are fully consistent with typical Br/S ratios for passive degassing.

Competition between HOBr + HBr and HOBr + HCl

The relative importance of reactions

$$HOBr + HBr \rightarrow Br_2 + H_2O \quad \text{Eq. 34}$$

$$HOBr + HCl \rightarrow BrCl + H_2O \quad \text{Eq. 35}$$

depends strongly on the availability of their acidic reactants. Although the HOBr + HBr pathway is intrinsically faster (Burkholder et al., 2020), the concentration of HBr decreases rapidly due to oxidation near the vent, while HCl remains abundant. Consequently, the reaction of HOBr with HCl becomes the dominant heterogeneous pathway, producing higher BrCl relative to Br_2.

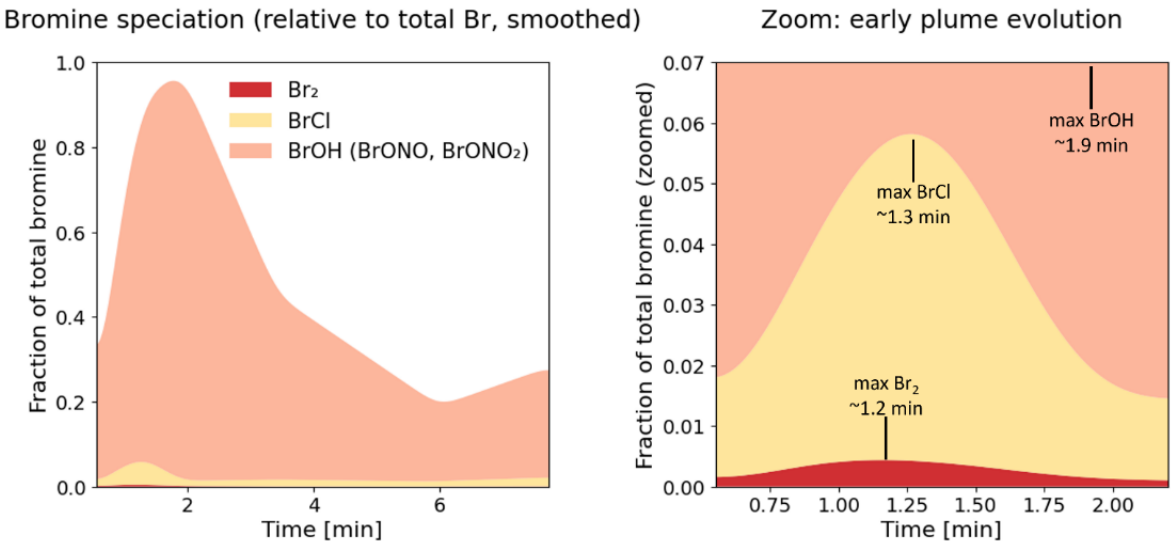

Figure 22: Bromine speciation, molecular Bromine, Chlorine and Bromine chloride and their maxima, compared to total bromine during the first campaign in 2022.

This chemical progression is reflected in the observed temporal evolution of molecular bromine species during the first minutes after emission (Fig. 22). The maxima of Br_2 and BrCl occur early in the plume and within a narrow time window (~1.2–1.3 min), consistent with initial heterogeneous activation while HBr is still present. Given the temporal resolution of plume-age reconstruction, these two maxima cannot be robustly separated from one another. In contrast, the BrX maximum, interpreted to be dominated by HOBr, is clearly delayed (~1.9 min), indicating a subsequent oxidation stage.

The consistent ordering of these maxima, rather than their exact timing, is the key constraint provided by the data. The delayed BrX peak points to a transition from early heterogeneous interhalogen formation toward a regime dominated by gas-phase oxidation and recycling of bromine. After release from the aerosol phase, Br_2 and BrCl photolyze rapidly and can contribute to a reaction cascade that sustains HOBr production, consistent with the observed dominance of BrX at slightly later plume ages.

Cl_2 dynamics differed between the two campaigns. Despite similar Cl_2/S oxidation ratios overall, one particularly high value was recorded in 2023. This difference may reflect incomplete sampling of the Cl_2 peak in 2022, or it could indicate that initial Cl_2 formation proceeded through pathways largely independently of bromine such as:

$$HCl + O_3 \rightarrow HOCl + O_2 \qquad \text{Eq. 36}$$

$$HOCl + HCl \rightarrow Cl_2 + H_2O \qquad \text{Eq. 37}$$

The occurrence of higher Cl_2 concentrations in 2023 despite lower Br and BrCl levels suggests that Cl_2 formation became more efficient under bromine-poor conditions. Reduced competition from the $HO_2 + HBr \rightarrow HOBr$ pathway would leave more HO_2 radicals available to react with HCl, enhancing HOCl formation and thereby favoring the subsequent $HOCl + HCl \rightarrow Cl_2$ reaction. This mechanism, consistent with (Roberts et al., 2009), provides a plausible explanation for the relative enhancement of Cl_2 observed in 2023. The coincidence of the Cl_2 maximum (~2 min) with the BrX maximum further supports the idea that once HBr is depleted, chlorine oxidation proceeds more freely. However, given the limited number of Cl_2 observations and uncertainties in plume-age reconstruction, this interpretation should be regarded as indicative rather than definitive.

Bromine versus Chlorine Activation Kinetics

The pronounced disparity between bromine and chlorine activation observed in both years aligns with established kinetic data. Laboratory studies show that the rate coefficient for

$$OH + HBr \rightarrow Br + H_2O \quad \text{Eq. 38}$$

exceeds that of

$$OH + HCl \rightarrow Cl + H_2O \quad \text{Eq. 39}$$

by nearly an order of magnitude under tropospheric conditions (Burkholder et al., 2020). Consequently, bromine activation proceeds much faster than chlorine oxidation, leading to near-complete bromine conversion (BrX/Br ~1) while chlorine remains kinetically limited to a few percent (ClX/Cl ~ 0.02).

Bromine-mediated reactions can, in principle, contribute to chlorine activation via the formation of BrCl. However, reactions such as

$$ClO + HBr \rightarrow HOCl + BrO \quad \text{Eq. 40}$$

$$HOCl + HBr \rightarrow HCl + BrOH \quad \text{Eq. 41}$$

primarily act as deactivation or recycling steps. These pathways convert reactive chlorine back to HCl while generating reactive bromine species (BrO or HOBr). Thus, cross-family reactions tend to redistribute reactivity rather than produce a net activation of chlorine, consistent with the persistently low ClX/Cl ratios observed in both years.

Decay of Reactive Halogen Species and Iodine Behavior

A pronounced time-dependent decrease of reactive halogen species (ClX, BrX, IX) was observed in the aging volcanic plume. This decline marks the transition to a late oxidation regime in which several processes contribute to the loss of detectable reactive halogens. The most fundamental mechanism is photolysis, which rapidly converts halogen species into halogen radicals. These radicals are not detected by the TMB-coated filters which leads to a loss of HalX signal. Photolysis rates follow the known order I >> Br > Cl, implying that iodine-containing species are removed fast from the detectable reactive halogen pool (Burkholder et al., 2020).

A second potential sink is the formation of halocarbon compounds via reactions between halogen radicals and hydrocarbons. Such processes have been experimentally demonstrated and volcanic plumes are known to contain a variety of halogenated organic compounds, including chlorinated, brominated and iodinated species (Jordan et al., 2000). Formation pathways typically require halogen radicals, methane or unsaturated hydrocarbons and often transition-metal catalysts present in volcanic gas–rock interaction zones. Examples include:

$$2\,\mathrm{Cl} + \mathrm{C}_x\mathrm{H}_y \rightarrow \mathrm{C}_x\mathrm{H}_{y-1}\mathrm{Cl} + \mathrm{HCl} \qquad \text{Eq. 42}$$

These reactions represent chemically stable sinks and can contribute to the observed decline of BrX and ClX. Reaction kinetics between halogen radical and hydrocarbons, however, favor chlorine radicals over bromine and iodine in the order Cl >> Br >> I, whereas photolytic loss proceeds in the opposite order (Burkholder et al., 2020). Thus, the combined halogen loss pattern in the data provides insight into the relative importance of these pathways.

In the present dataset, ClX decreases significantly with plume age, but the decline remains less pronounced than for BrX and especially IX. This behavior is inconsistent with hydrocarbon reactions acting as the dominant sink, because the fast radical–hydrocarbon kinetics of chlorine would otherwise produce a steeper decline in ClX than in BrX. In contrast, the measurements show a much stronger decline of IX, followed by BrX and a comparatively weaker decrease of ClX. This halogen-specific decay pattern is therefore most consistent with photolytic loss dominating over hydrocarbon reactions.

For iodine, the observed two-orders-of-magnitude decrease of IX (in 2022) is readily explained by its very fast photolysis, which exceeds that of BrO and ClO by an order of magnitude. In addition, iodine oxides are well known to nucleate new particles under atmospheric conditions (Hoffmann et al., 2001), forming I-rich aerosols that cannot be detected by TMB coatings. Such particle formation offers a second efficient sink for reactive iodine and explains the disproportionately rapid disappearance of IX compared to BrX and ClX. Whether similar particle-mediated losses occur for bromine at volcanic temperatures and humidities remains uncertain, but available data suggest that iodine is uniquely efficient at initiating aerosol formation (Saiz-Lopez and Glasow, 2012).

Taken together, the combined decline of ClX, BrX and IX in the aging plume can most plausibly be attributed to (1) halogen-specific photolysis, followed by (2) species-dependent secondary processes, including organic halide formation and, in the case of iodine, aerosol nucleation. The decay pattern with IX > BrX > ClX decreasing in that order is therefore consistent with the known relative photolysis rates and the potential loss of iodine due to particle formation, whereas reactions with hydrocarbons appear to play a comparatively minor role in the loss of reactive halogens under the conditions sampled. This interpretation aligns with experimental observations of volcanic halocarbons formation (Jordan et al., 2000), but also with the small and highly variable abundance of such compounds in volcanic plumes, suggesting that their formation does not dominate reactive halogen loss on the timescales probed in this study.

6.5 Conclusion of Etna measurements

This study presents comprehensive UAV-based in-plume measurements of reactive halogen species at Mt. Etna, combining alkaline traps for total halogens and sulfur with selective derivatization filters for molecular and unspecific reactive halogens. The results show that bromine activation occurs within the first minutes after emission and proceeds largely independently of total halogen abundance or mixing ratio. The steep rise of BrX relative to Br_2 and BrCl indicates that early bromine oxidation is dominated by gas-phase formation of HOBr, with heterogeneous interhalogens playing only a secondary role near the vent. Chlorine activation remains comparatively weak, yet brief Cl_2 peaks indicate HOCl-mediated formation once HBr is depleted. Reactive iodine decays fastest, implying efficient conversion or particle-associated losses.

Interannual variability and implications for magmatic control

The interannual comparison reveals markedly higher bromine and iodine abundances in 2022, yet both campaigns exhibit the same oxidation sequence and timing. This demonstrates that early halogen oxidation at Mt. Etna is governed primarily by mixing and oxidant availability, while the absolute halogen levels—and therefore halogen/S ratios—reflect underlying magmatic conditions. Small differences in Br/S between 2022 and 2023 are mirrored in the oxidation behavior and in the inferred high-temperature oxidation states. Because model trajectories are highly sensitive to initial halogen inventories and temperature, these observations confirm that even subtle magmatic changes produce measurable shifts in early plume chemistry. The inverse holds as well: changes in reactive halogen oxidation can be diagnostic of evolving magmatic conditions.

Role of UAVs in resolving rapid near-vent chemistry

The UAV-based sampling system proved robust, reliable and analytically sensitive. Crucially, UAVs enable dense, high-frequency sampling directly inside the young plume, capturing chemical transitions that occur on timescales of seconds to minutes and are not accessible by ground-based or remote sensing approaches. UAVs also allow simultaneous detection of multiple halogen species (BrX, Br_2, BrCl, Cl_2, IX), making it possible to disentangle the coupled oxidation pathways governing early

plume evolution. These capabilities are essential because the chemical system is extremely sensitive and small variations in source conditions generate detectable differences in halogen speciation. Operationally, UAVs enhance safety and accessibility in hazardous near-vent environments and can target plume regions that cannot be instrumented permanently or reached during active degassing.

Bridging the gap between near-vent chemistry and remote sensing

A central outcome of this work is that UAV observations help bridge the long-standing gap between high-temperature, near-source oxidation processes and remote sensing measurements of the aging plume. Satellite and DOAS observations are ideal for long-range plume monitoring but inherently integrate over older, cooler plume sections. The presented methods constitute a critical missing link: they experimentally verify model predictions for the earliest oxidation stages and provide boundary conditions for interpreting remote-sensing–derived BrO/SO_2 satellite data. As such, they contribute to reducing uncertainties when using halogen ratios as indicators of magmatic changes and volcano unrest.

7 Ground-based Halogen Measurements at Vulcano

In September 2023, near-source halogen measurements were conducted at fumarole F0 on Vulcano (Fig. 23). Two independent sampling systems were used: alkaline traps (Raschig tube or bubbler) for total halogens and sulfur and *cis* -stilbene filters for the quantification of Cl_2, BrCl and Br_2. Sampling was carried out at plume age times of approximately 1–10 s after emission, allowing direct investigation of the earliest stages of halogen activation. Plume age was determined by visually tracking individual gas puffs rather than by combining distance and wind measurements, which provided more robust and precise plume-age estimates under the prevailing conditions.

The fumarole field at Vulcano is spatially dense, with numerous vents located only a few meters apart. Rapidly changing wind conditions can cause overlap of gas plumes and in some cases an unambiguous assignment of sampled gas to a single vent was not possible. This introduces an inherent, but unavoidable, source of variability in both near-source and long-term datasets.

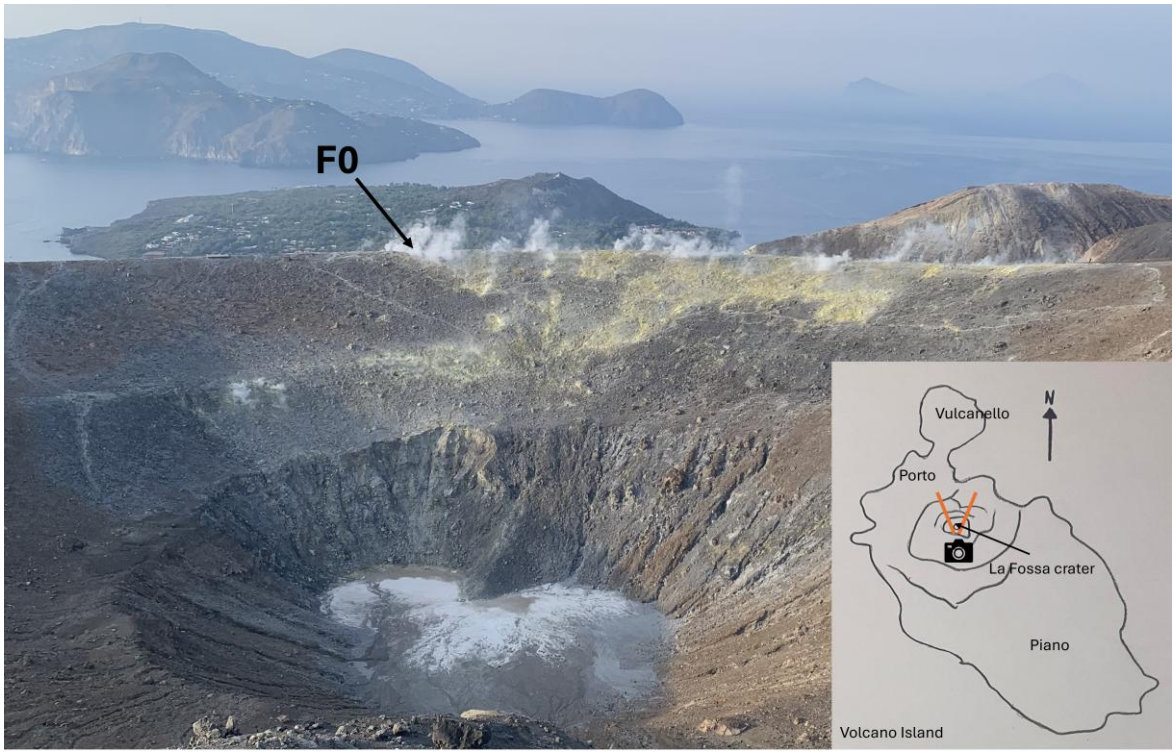

Figure 23: View of the La Fossa crater on Vulcano Island showing the active fumarole field, with the fumarole F0 explicitly indicated; the inset provides a schematic map of Vulcano Island illustrating the location of the La Fossa crater and the measurement site.

To place the 2023 measurements into a broader geochemical context, fumarole gas samples collected by Sergio Calabrese (INGV) between November 2021 and December 2022 were analyzed using the same procedures. These samples cover the 2021–2022 period of volcanic unrest, during which strongly elevated CO_2 and SO_2 emissions, increased fumarole temperatures and geochemical evidence for enhanced magmatic input were reported. An additional 1:1 dilution step prior to neutralization was required due to the high initial hydroxide concentrations in these samples.

The combined datasets provide complementary perspectives: the 2023 measurements resolve rapid photochemical processes in the early plume, while the 2021–2022 samples document long-term variability in fumarolic composition during and after a period of intensified magmatic input.

To place these measurements and the unrest-period samples into a broader context published fumarole data (2020-2023) from (Capecchiacci et al., 2025) were also considered. These data represent multi-year mean F/S and Cl/S ratios from the main fumarolic field and provide a long-term reference against which the 2021–2022 and 2023 datasets can be compared.

7.1 September 2023 measurements

The September 2023 dataset comprises daytime and nighttime samples. The average F/S, Cl/S and Br/S ratios were $(6.8 \pm 1.1) \times 10^{-3}$, $(2.8 \pm 0.5) \times 10^{-1}$ and $(7.7 \pm 1.2) \times 10^{-5}$, respectively. The complete dataset (Tab. 11) also includes halogen speciation of *cis* -stilbene filter measurements with Cl_2, BrCl and Br_2 quantification at day- and nighttime.

Table 11: Halogen-to-sulfur ratios (F/S, Cl/S, Br/S) and speciated molecular halogen ratios (Cl_2/S, BrCl/S) measured in the near-source plume at Vulcano during September 2023, including daytime and nighttime samples at plume ages between 1 and 10 s. Halogen speciation was obtained from *cis* -stilbene filter samples. Values below the detection limit are reported as <LOD.

Time	Age [s]	F/S [10^{-3}]	Cl/S [10^{-1}]	Br/S [10^{-4}]	Cl_2/S	BrCl/S
day	1 ± 1	11 ± 2	0.75 ± 0.15	1.3 ± 0.3	< LOD	< LOD
day	4 ± 1	2.5 ± 0.4	2.5 ± 0.5	< LOD	$(5.2 \pm 0.5) \cdot 10^{-10}$	$(3.8 \pm 0.4) \cdot 10^{-11}$
day	1 ± 1	9.3 ± 1.4	1.7 ± 0.3	1.1 ± 0.3	< LOD	< LOD
day	4 ± 1	6.5 ± 1.0	4.0 ± 0.8	0.90 ± 0.23	$(1.2 \pm 0.1) \cdot 10^{-9}$	$(7.5 \pm 0.8) \cdot 10^{-11}$
night	4 ± 1	8.2 ± 1.2	3.1 ± 0.6	0.53 ± 0.13	$(7.4 \pm 0.7) \cdot 10^{-12}$	$(2.6 \pm 0.3) \cdot 10^{-13}$
night	1 ± 1	7.2 ± 1.1	2.5 ± 0.5	0.87 ± 0.22	< LOD	< LOD
day	5 ± 1	1.5 ± 0.2	2.0 ± 0.4	0.25 ± 0.06	$(1.5 \pm 0.2) \cdot 10^{-9}$	$(6.9 \pm 0.7) \cdot 10^{-11}$
night	10 ± 1	4.3 ± 0.6	2.6 ± 0.5	0.39 ± 0.10	$(2.7 \pm 0.3) \cdot 10^{-10}$	$(1.0 \pm 0.1) \cdot 10^{-11}$
day	2 ± 1	10 ± 2	6.2 ± 1.2	0.84 ± 0.21	$(1.4 \pm 0.2) \cdot 10^{-10}$	$(1.2 \pm 0.1) \cdot 10^{-11}$

Daytime values of Cl_2/S and BrCl/S were consistently higher than nighttime values, with maxima of 1.5×10^{-9} and 7.5×10^{-11} observed during the day, compared to nighttime maxima of 2.7×10^{-10} and 1.0×10^{-11}. Br_2 was not detectable in any sample.

Figure 24 illustrate Cl_2/S and BrCl/S as a function of plume age and time of day. The results demonstrate low but measurable molecular halogens in the near-source plume, except 1 second after emission and a systematic daytime–nighttime difference.

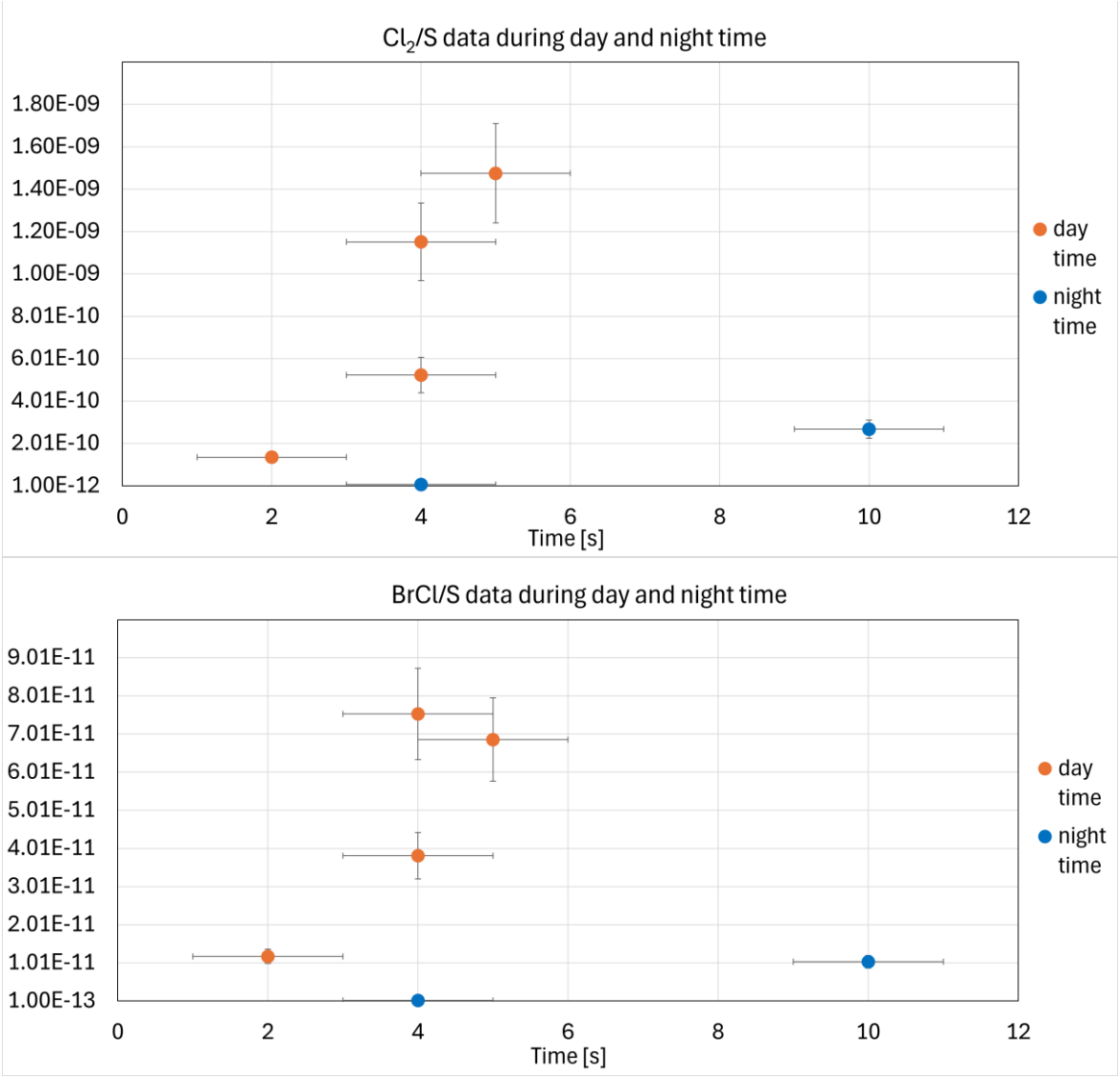

Figure 24: Cl_2/S (top) and BrCl/S (bottom) ratios plotted against plume age for daytime and nighttime measurements in September 2023.

The eleven fumarole samples collected between November 2021 and December 2022 (S. Calabrese) capture the elevated degassing activity associated with the unrest (Tab. 12). Early samples (Nov 2021–Feb 2022) show Cl/S ratios of approximately 0.2–0.4 and Br/S ratios up to 4.9×10^{-4}, while F/S ranges between 3×10^{-3} and 2×10^{-2}. Moderately elevated values persisted through spring and summer 2022. A

pronounced anomaly occurred on 1 December 2022, with Cl/S reaching ~1.2 and Br/S nearly 8.7×10^{-4}.

In contrast, the September 2023 samples show substantially lower ratios, with Cl/S values between 0.07 and 0.62 and Br/S values between 2.4×10^{-5} and 1.3×10^{-4}. F/S shows no consistent trend. Overall, the data indicate a return to fumarolic compositions more typical of hydrothermally buffered degassing.

Table 12: Halogen-to-sulfur ratios (F/S, Cl/S, Br/S) and sulfur concentrations measured in alkaline trap samples from the Vulcano fumarole field between November 2021 and December 2022 (S. Calabrese), covering the period of elevated degassing activity during volcanic unrest. Uncertainties represent analytical variability.

Date	Alkaline solution			
	F/S [10^{-3}]	Cl/S [10^{-1}]	Br/S [10^{-4}]	S [mol/L] [10^{-4}]
17.11.21	7.3 ± 1.1	2.0 ± 0.4	1.4 ± 0.4	8.34 ± 0.08
18.11.21	3.0 ± 0.5	1.9 ± 0.4	0.50 ± 0.13	19.5 ± 0.2
14.12.21	11 ± 2	2.4 ± 0.5	3.2 ± 0.8	20.7 ± 0.2
02.02.22	18 ± 3	3.8 ± 0.8	4.9 ± 1.2	4.21 ± 0.04
03.02.22	20 ± 3	3.8 ± 0.8	1.2 ± 0.3	5.11 ± 0.05
03.02.22	7.9 ± 1.2	2.5 ± 0.5	0.28 ± 0.07	3.58 ± 0.04
11.04.22	9.4 ± 1.4	3.7 ± 0.7	1.2 ± 0.3	8.84 ± 0.09
12.04.22	18 ± 3	2.4 ± 0.5	2.3 ± 0.6	1.87 ± 0.2
22.06.22	25 ± 4	3.2 ± 0.6	2.2 ± 0.6	5.97 ± 0.06
22.06.22	6.6 ± 1.0	4.0 ± 0.8	0.48 ± 0.12	18.8 ± 0.2
01.12.22	4.5 ± 0.7	12 ± 2	8.7 ± 2.2	4.21 ± 0.04

Figures 25 additionally compare the new September 2023 measurements (yellow), the 2021–2022 samples (blue) and the published values (mean values) from Capecchiacci et al. (grey). The red marker represents the September 2023 mean. For F/S, the published dataset spans values of approximately 4.0×10^{-3} to 1.1×10^{-2} throughout 2020–2023, overlapping with the ranges observed in both the unrest-period samples and the September 2023 measurements. For Cl/S, the Capecchiacci data show low values during 2020–2021, a clear increase during late 2021 and early 2022 and a decline toward 2023. Br/S was not determined in the dataset and is therefore shown only for the 2021–2022 and 2023 samples.

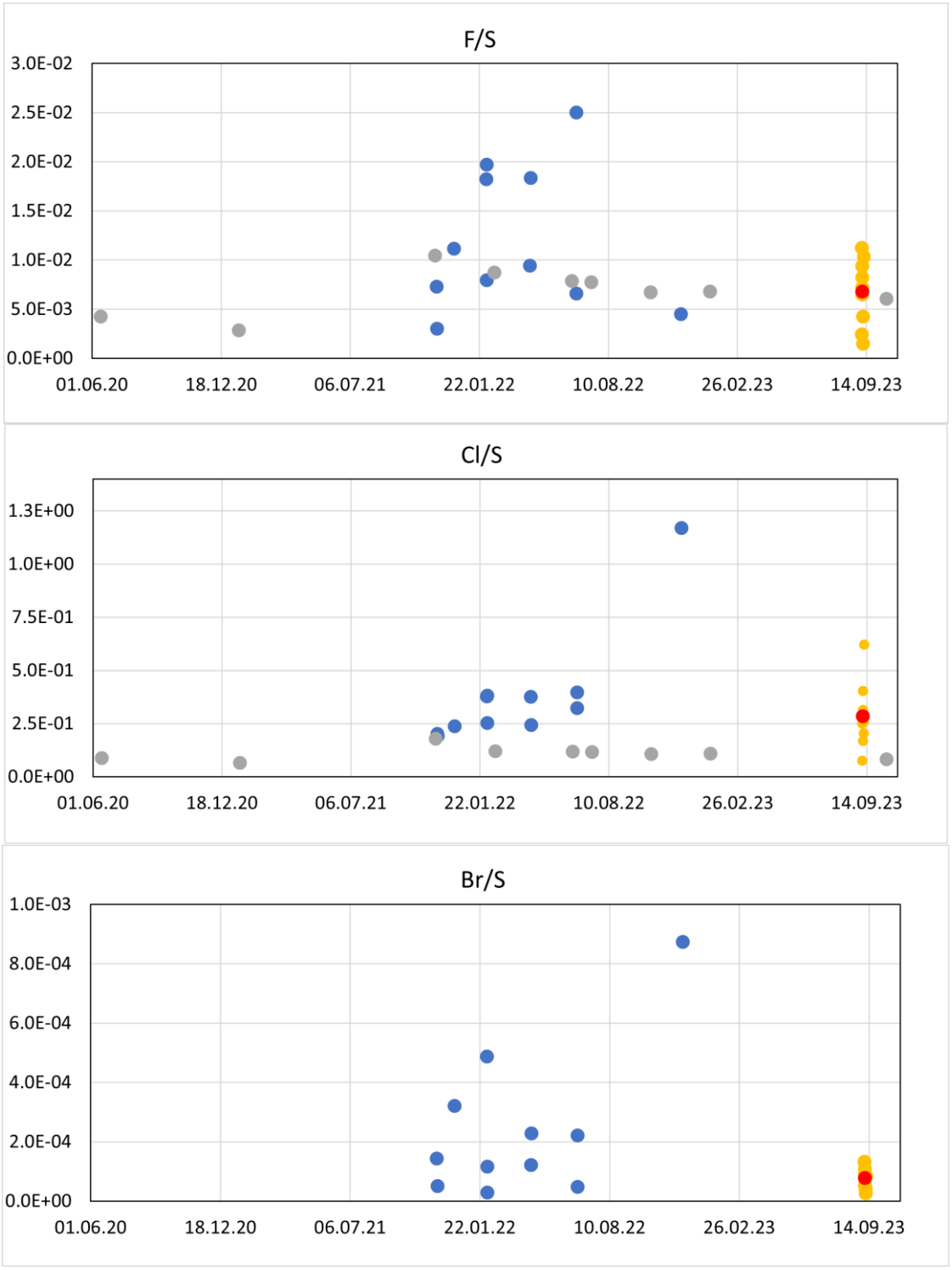

Figure 25: Temporal evolution of F/S (top), Cl/S (middle) and Br/S ratios (bottom) at the Vulcano fumarole field, comparing published mean values from Capecchiacci et al. (grey), samples collected during the 2021–2022 unrest period (blue) and new measurements from September 2023 (yellow). The red marker indicates the mean value of the September 2023 dataset.

7.2 Discussion

7.2.1 Near-source photochemical halogen activation (2023)

The marked daytime–nighttime contrast in Cl_2 and BrCl abundances reflects the fundamental photochemical behavior of halogens in volcanic plumes. Radical-mediated pathways initiated by the photolysis of halogen oxides (e.g. HOBr, BrO, $BrONO_2$) and ozone-related activation reactions operate efficiently only under sunlight. Nighttime measurements show strongly reduced Cl_2 and BrCl, consistent with the collapse of the radical pool in ambient air after sunset. This behavior is supported by observations and modelling studies such as Bobrowski et al. (2007), von Glasow and Crutzen (2003), Roberts et al. (2009) and Saiz-Lopez and von Glasow (2012).

The short plume ages demonstrate that halogen activation begins within seconds after emission but remains strictly light-dependent. Br_2 was below detection in all samples, consistent with its short photolytic lifetime and low abundance at Vulcano fumarolic gases.

No Cl_2, BrCl, or Br_2 were detected in the samples collected at a plume age of ~1 s. This suggests that bromine and molecular halogens are not emitted directly at the source but are produced rapidly after emission through plume chemistry.

The dense structure of the fumarole field introduces uncertainty, as rapid changes in wind direction can cause plumes from nearby vents to merge. Although plume age was determined with high temporal precision by visual tracking, full certainty regarding vent-specific origin cannot be guaranteed for every measurement. This introduces variability but does not alter the interpretation of the pronounced photochemical day–night differences.

7.2.2 Halogen/S ratios and long-term changes in volatile sources (2021–2022 vs. 2023)

Halogen-to-sulfur ratios provide robust indicators of magmatic versus hydrothermal contributions to volcanic gases. Elevated Cl/S and Br/S ratios characterize periods of increased magmatic input, whereas reduced ratios reflect more efficient hydrothermal scrubbing and enhanced water–gas interaction (Chiodini et al., 1993; Symonds et al., 2001).

The elevated Cl/S and Br/S values observed from late 2021 through mid-2022 align with the volcanic unrest at Vulcano, which was marked by increased CO_2 and SO_2

emissions, high fumarole temperatures and geochemical indications of enhanced magmatic gas supply (INGV Bulletins, 2021–2022). The extreme Cl/S and Br/S anomaly on 1 December 2022 could reflect the transient arrival of hotter, less hydrothermally processed magmatic gas. However, this was only one data point and measurements before and after do not support this and uncertainties are high whether this is an artifact or not.

By September 2023, the halogen/S ratios had significantly decreased, indicating a return to a hydrothermally buffered regime. This interpretation is consistent with the decline in unrest indicators reported by INGV throughout 2023. The long-term trends reported by Capecchiacci et al. (2020–2023) are consistent with this pattern. The published data show low Cl/S and F/S ratios during 2020–2021, followed by a pronounced increase beginning in late 2021 and extending into early 2022, mirroring the elevated values observed in the 2021–2022 samples analyzed here. The decline in Cl/S and F/S ratios throughout 2023 documented by Capecchiacci et al. agrees with the lower ratios measured in September 2023, indicating a return to a more hydrothermally buffered degassing regime. As Br/S was not determined in the published dataset, bromine trends rely solely on the 2021–2022 and 2023 measurements.

Differences among halogens also support this interpretation. Chlorine and bromine are highly soluble in aqueous phases and are efficiently removed during hydrothermal water–gas interaction, whereas fluorine displays different solubility and sorption behavior. This can explain why F/S remains comparatively stable, while Cl/S and Br/S exhibit stronger responses to changes in hydrothermal buffering and magmatic input.

As in the near-source measurements, the close spacing of vents and variable wind conditions may contribute to variability within the dataset. However, the magnitude and systematic nature of the changes between 2021–2022 and 2023 are consistent with a transition from magmatically dominated degassing during the unrest to hydrothermally moderated conditions in 2023.

7.3 Conclusion of Vulcano measurements

Ground-based near-source measurements at the Vulcano fumarole field demonstrate that halogen activation in volcanic plumes begins within seconds after emission and is strongly controlled by photochemical processes. The combined use of alkaline traps and *cis* -stilbene filter sampling allowed simultaneous quantification of total halogen-to-sulfur ratios and speciated molecular halogens at plume ages between 1 and 10 s. Molecular halogens (Cl_2 and BrCl) were detectable at plume ages $\geq$ 2 s, while no molecular halogens were observed at ~1 s after emission, indicating that they are not emitted directly at the source but are formed rapidly within the plume.

Comparison with fumarole samples collected during the 2021–2022 unrest period reveals pronounced temporal variability in halogen-to-sulfur ratios at Vulcano. Elevated Cl/S and Br/S ratios during the unrest contrast with the substantially lower values observed in September 2023, while F/S ratios remain comparatively stable. These patterns are consistent with a transition from magmatically influenced degassing during the unrest to more hydrothermally buffered conditions in 2023, in agreement with independent geochemical observations and published long-term datasets.

Together, the near-source plume measurements and the longer-term fumarole records provide complementary constraints on halogen behavior at Vulcano. The results highlight the importance of combining high-time-resolution plume measurements with multi-year fumarolic datasets to resolve both rapid photochemical processes and longer-term changes in volatile sources in active volcanic systems.

8 Halogen-to-sulfur ratios at Nyamuragira and Nyiragongo in the context of previous studies

Samples from Nyamuragira and Nyiragongo were collected during a measurement campaign in 2020 by Nicole Bobrowski and submitted for analysis. The samples were analyzed following the same procedures as those applied to the Vulcano fumarole samples provided by S. Calabrese. The analyzed samples and the corresponding halogen-to-sulfur ratios are summarized in Table 13.

Table 13: Halogen-to-sulfur ratios (F/S, Cl/S, Br/S) and sulfur concentrations measured in alkaline trap samples collected at Nyamuragira and Nyiragongo during the 2020 measurement campaign.

Location	Date	Alkaline solution			
		F/S [10^{-2}]	Cl/S	Br/S [10^{-5}]	S [mol/L * 10^{-4}]
Nyamuragira	06.02.20	2.2 ± 0.4	0.21 ± 0.03	<LOD	9.5 ± 0.2
Nyiragongo 3rd terrace	10.02.20	8.9 ± 3.1	1.4 ± 0.6	<LOD	0.56 ± 0.03
Nyiragongo 3rd terrace	12.02.20	6.2 ± 1.5	0.45 ± 0.14	<LOD	2.0 ± 0.1
Nyiragongo 3rd terrace	13.02.20	11 ± 2.2	0.11 ± 0.02	7.1 ± 1.8	29 ± 1.4

This study provides ground-based measurements of total halogen-to-sulfur ratios at Nyamuragira and Nyiragongo obtained using Raschig tube. The results can be placed in context with previous studies that employed spectroscopic techniques targeting specific gas-phase species.

At Nyiragongo, the alkaline trap measurements yield F/S ratios on the order of 10^{-2} and Cl/S ratios ranging from 10^{-1} to approximately 1, while Br/S ratios are predominantly below detection limits, with only a single detection at the 10^{-5} level. FTIR-based measurements at Nyiragongo report HCl/SO_2 and HF/SO_2 ratios on the order of 10^{-2} –10^{-1} and 10^{-2}, respectively (Sawyer et al., 2008). The Cl/S ratios obtained from alkaline trap samples in this study reach higher values, while F/S ratios fall within a similar order of magnitude. Bromine was not quantified in the FTIR studies.

For Nyamuragira, the alkaline trap data indicate F/S ratios of approximately 10^{-2} and Cl/S ratios on the order of 10^{-1}, while Br/S remains below detection limits. Comparable alkaline trap measurements conducted during the 2014–2015 lava lake activity at Nyamuragira reported Cl/S ratios of 0.13 and 0.17, F/S ratios of 0.06 and

0.11 and ratios for Br/S of 2.3×10^{-4} and 1.0×10^{-4} for 2014 and 2015 (Bobrowski et al., 2017). The values obtained in the present study therefore fall within the same order-of-magnitude range as those earlier measurements.

Previous spectroscopic observations at Nyiragongo and Nyamuragira have focused primarily on reactive bromine, reporting BrO/SO_2 ratios typically on the order of 10^{-5} (Bobrowski et al., 2015). These measurements are not directly comparable to the total Br/S ratios reported here, as BrO represents only a fraction of total bromine and is subject to rapid plume chemistry. Nevertheless, the generally low Br/S ratios observed in the alkaline trap samples are consistent in magnitude with the overall picture of bromine being a minor halogen component in the bulk gas emissions of these volcanoes.

Overall, despite the use of different measurement techniques and target species, the halogen-to-sulfur ratios obtained in this study fall within the same order-of-magnitude ranges as those reported in previous work. This indicates broad consistency among datasets and supports the use of alkaline trap measurements as a complementary approach for characterizing bulk halogen emissions.

9 Advances, Remaining Challenges and Future Directions in Volcanic Plume Chemistry

This work addresses several long-standing limitations in volcanic plume halogen measurements by (i) providing quantitative constraints on halogen speciation in young volcanic plumes with high temporal resolution, (ii) developing and validating UAV-based methods for the quantification of both total and speciated halogen compounds, and (iii) demonstrating reproducible performance at low detection limits under field conditions. Together, these advances reveal new and more specific knowledge gaps, many of which only become accessible through the methodological and observational framework established in this work, and which define the next generation of research in volcanic plume chemistry.

1. Outstanding Chemical Knowledge Gaps

A deeper understanding of volcanic plume chemistry requires resolving several unknown aspects of halogen oxidation pathways. Key uncertainties include the formation, reaction mechanisms and concentrations of radical halogens, the production of halogen-containing alkanes and the microphysical processes associated with particle formation and related chemistry. While this work constrains the evolution of stable inorganic and organically bound halogen reservoirs in young plumes, it simultaneously highlights that a potentially significant fraction of the total halogen budget may transiently reside in radical form during later oxidation stages.

Radical chemistry remains particularly poorly constrained and may represent a major fraction of the halogen inventory during later stages of plume oxidation. These radicals are extremely difficult to detect *in-situ*. Although derivatization could theoretically stabilize them, organic derivatization agents that react with radicals tend to form new radicals and unstable products. Organo-metallic trapping concepts may represent a speculative but potentially promising alternative, as certain metal–halogen radical complexes could exhibit sufficient stability for analytical detection; however, such approaches would require fundamental validation of reaction pathways and product stability.

Additional chemical sinks may include the formation of halogenated alkenes, which have been qualitatively detected in past studies. Another important target for future

research is the measurement of OH radicals, which play a controlling role in oxidation kinetics. Future work should also integrate simultaneous measurements of particles and volatile species to capture the coupled processes that govern multiphase halogen activation.

2. Analytical Method Development

Improved analytical techniques are essential for lowering detection limits and expanding the range of detectable halogen species. One promising direction involves quantifying halogens collected in alkaline solutions via GC-MS. This approach requires converting aqueous halides into GC-measurable compounds and would enable total halogen analysis via GC instead of ion chromatography. Derivatization of halides into organic compounds represents a key methodological step toward this goal.

Such derivatization-based approaches could improve detection limits and allow fluoride to be measured alongside bromide and chloride, overcoming limitations of current ICP-MS methods. In this framework, alkaline traps would remain the primary sampling tool but would require an additional derivatization step prior to analysis. Existing halide derivatization methods on denuders (measured via HPLC-MS) demonstrate feasibility but currently suffer from comparatively high detection limits. Development of new GC-measurable derivatization coatings applied on filters or for derivatization of anions trapped in alkaline solution could advance speciation capability and significantly lower detection limits when analyzed by GC-HRMS.

A particularly promising future direction may involve the use of (perfluorophenyl)methyl-p-Tosylate (CAS 32974-36-0) as a derivatization reagent capable of directly converting halide anions (F^-, Cl^-, Br^-, I^-) collected in alkaline traps into GC-measurable organic derivatives. Such an approach could, in principle, enable total halogen analysis by GC–HRMS and further reduce detection limits compared to existing ion chromatographic methods. Preliminary exploratory experiments indicate that this compound may also facilitate direct derivatization of halide species from the gas phase, suggesting the potential for filter-based or in-line derivatization strategies; however, these observations remain qualitative and require systematic validation with respect to reaction efficiency, selectivity, recovery and stability.

3. UAV-Based Remote Sensing and *In-Situ* Instrumentation

Based on the successful UAV-based sampling and quantification strategies demonstrated in this work, future UAV platforms should aim to integrate complementary sensing techniques. Remote sensing methods for volcanic gases have undergone substantial miniaturization over recent decades. Drone-based DOAS systems and UV cameras have already been successfully deployed. The optimal future configuration would combine multiple sensor types on a single UAV platform to maximize spatial coverage and achieve high-resolution point measurements of halogen species within volcanic plumes.

A more ambitious long-term technological goal is the development of a drone-based GC system. A pulse discharge detector (PDD) is a promising candidate for such an instrument because it can detect a wide range of compounds following chromatographic separation.

4. Integration with Chemical and Geological Models

Comprehensive datasets from advanced analytical methods and UAV-based systems will enable significant improvements in chemical models of plume evolution. Such models could finally link magmatic composition and geological parameters with atmospheric halogen chemistry. Integrating these domains would provide critical insights into volcanic processes and may contribute to improved forecasting of volcanic and eruptive behavior.

5. Advances in Drone Technology and Measurement Automation

Recent progress in UAV technology has resulted in commercially available platforms with increased payload capacity, flight time and operational safety. These developments open the possibility of fully automated volcanic gas measurements using onboard sensors, eliminating the need for researchers to approach summit or vent areas with substantial safety risks.

Automated UAV operations equipped with advanced analytical instruments would dramatically enhance spatial and temporal coverage of volcanic gas data and represent a major step forward for routine plume monitoring. Such automated systems would be particularly powerful when combined with chemically selective

sampling and derivatization approaches, enabling routine, high-frequency measurements of reactive halogen species.

10 References

Aiuppa, A., Federico, C., Franco, A., Giudice, G., Gurrieri, S., Inguaggiato, S., Liuzzo, M., McGonigle, A. J. S., and Valenza, M.: Emission of bromine and iodine from Mount Etna volcano, Geochem Geophys Geosyst, 6, https://doi.org/10.1029/2005GC000965, 2005.

Aiuppa, A., Burton, M., Murè, F., and Inguaggiato, S.: Intercomparison of volcanic gas monitoring methodologies performed on Vulcano Island, Italy, Geophysical Research Letters, 31, https://doi.org/10.1029/2003GL018651, 2004.

Allard, P., Carbonnelle, J., Dajlevic, D., Le Bronec, J., Morel, P., Robe, M. C., Maurenas, J. M., Faivre-Pierret, R., Martin, D., Sabroux, J. C., and Zettwoog, P.: Eruptive and diffuse emissions of CO2 from Mount Etna, Nature, 351, 387–391, https://doi.org/10.1038/351387a0, 1991.

Allard, P., Behncke, B., D'Amico, S., Neri, M., and Gambino, S.: Mount Etna 1993–2005: Anatomy of an evolving eruptive cycle, Earth-Science Reviews, 78, 85–114, https://doi.org/10.1016/j.earscirev.2006.04.002, 2006.

Arellano, S., Yalire, M., Galle, B., Bobrowski, N., Dingwell, A., Johansson, M., and Norman, P.: Long-term monitoring of SO2 quiescent degassing from Nyiragongo's lava lake, Journal of African Earth Sciences, 134, 866–873, https://doi.org/10.1016/j.jafrearsci.2016.07.002, 2017.

Barberi, F., Innocenti, F., Ferrara, G., Keller, J., and Villari, L.: Evolution of Eolian arc volcanism (Southern Tyrrhenian Sea), Earth and Planetary Science Letters, 21, 269–276, https://doi.org/10.1016/0012-821X(74)90161-7, 1974.

Bobrowski, N. and Giuffrida, G.: Bromine monoxide / sulphur dioxide ratios in relation to volcanological observations at Mt. Etna 2006–2009, Solid Earth, 3, 433–445, https://doi.org/10.5194/se-3-433-2012, 2012.

Bobrowski, N., Giuffrida, G. B., Arellano, S., Yalire, M., Liotta, M., Brusca, L., Calabrese, S., Scaglione, S., Rüdiger, J., Castro, J. M., Galle, B., and Tedesco, D.: Plume composition and volatile flux of Nyamulagira volcano, Democratic Republic of Congo, during birth and evolution of the lava lake, 2014–2015, Bull Volcanol, 79, https://doi.org/10.1007/s00445-017-1174-0, 2017.

Bobrowski, N., Glasow, R. von, Giuffrida, G. B., Tedesco, D., Aiuppa, A., Yalire, M., Arellano, S., Johansson, M., and Galle, B.: Gas emission strength and evolution of

the molar ratio of BrO/SO 2 in the plume of Nyiragongo in comparison to Etna, J. Geophys. Res., 120, 277–291, https://doi.org/10.1002/2013JD021069, 2015.

Bobrowski, N., Glasow, R. von, Aiuppa, A., Inguaggiato, S., Louban, I., Ibrahim, O. W., and Platt, U.: Reactive halogen chemistry in volcanic plumes, J. Geophys. Res., 112, https://doi.org/10.1029/2006JD007206, 2007.

Bobrowski, N., Hönninger, G., Galle, B., and Platt, U.: Detection of bromine monoxide in a volcanic plume, Nature, 423, 273–276, https://doi.org/10.1038/nature01625, 2003.

Burkholder, J. B., Sander, S.P., Abbatt, J., and Barker J.R.: Chemical kinetics and photochemical data for use in atmospheric studies, Evaluation No. 19, Tech. Rep. JPL Publication 19-5, Jet Propulsion Laboratory, Pasadena, CA, available at: https://jpldataeval.jpl.nasa.gov/, 2020.

Campion, R.: New lava lake at Nyamuragira volcano revealed by combined ASTER and OMI SO 2 measurements, Geophysical Research Letters, 41, 7485–7492, https://doi.org/10.1002/2014GL061808, 2014.

Capasso, G., Favara, R., Francofonte, S., and Inguaggiato, S.: Chemical and isotopic variations in fumarolic discharge and thermal waters at Vulcano Island (Aeolian Islands, Italy) during 1996: evidence of resumed volcanic activity, Journal of Volcanology and Geothermal Research, 88, 167–175, https://doi.org/10.1016/S0377-0273(98)00111-5, 1999.

Capecchiacci, F., Tassi, F., Vaselli, O., and Venturi, S.: The 2021–2023 unrest of Vulcano Island volcanic system (Aeolian Islands, Italy): geochemical evidence from fumarolic gas discharges and well waters, Bull Volcanol, 87, https://doi.org/10.1007/s00445-025-01810-7, 2025.

Carn, S. A. and Bluth, G. J. S.: Prodigious sulfur dioxide emissions from Nyamuragira volcano, D.R. Congo, Geophysical Research Letters, 30, https://doi.org/10.1029/2003GL018465, 2003.

Chiodini, G., Cioni, R., Marini, L., and Panichi, C.: Origin of the fumarolic fluids of Vulcano Island, Italy and implications for volcanic surveillance, Bull Volcanol, 57, 99–110, https://doi.org/10.1007/BF00301400, 1995.

Chiodini, G., Cioni, R., and Marini, L.: Reactions governing the chemistry of crater fumaroles from Vulcano Island, Italy, and implications for volcanic surveillance, Applied Geochemistry, 8, 357–371, https://doi.org/10.1016/0883-2927(93)90004-Z, 1993.

Crank, J.: The mathematics of diffusion: Part 4: Diffusion in a plane Sheet, 2. ed., Clarendon Press, Oxford, 414 pp., 1975.

Danckwerts, P. V. and Lannus, A.: Gas-Liquid Reactions, J. Electrochem. Soc., 117, 369C, https://doi.org/10.1149/1.2407312, 1970.

Daniel, J. S., Solomon, S., Portmann, R. W., and Garcia, R. R.: Stratospheric ozone destruction: The importance of bromine relative to chlorine, J. Geophys. Res., 104, 23871–23880, https://doi.org/10.1029/1999JD900381, 1999.

Díaz-Moreno, A., Barberi, G., Cocina, O., Koulakov, I., Scarfì, L., Zuccarello, L., Prudencio, J., García-Yeguas, A., Álvarez, I., García, L., and Ibáñez, J. M.: New Insights on Mt. Etna's Crust and Relationship with the Regional Tectonic Framework from Joint Active and Passive P-Wave Seismic Tomography, Surveys in geophysics, 39, 57–97, https://doi.org/10.1007/s10712-017-9425-3, 2018.

EBINGER, C. J.: Tectonic development of the western branch of the East African rift system, Geological Society of America Bulletin, 101, 885–903, https://doi.org/10.1130/0016-7606(1989)101<0885:TDOTWB>2.3.CO;2, 1989.

Federico, C., Cocina, O., Gambino, S., Paonita, A., Branca, S., Coltelli, M., Italiano, F., Bruno, V., Caltabiano, T., Camarda, M., Capasso, G., Gregorio, S. de, Diliberto, I. S., Di Martino, R. M. R., Falsaperla, S., Greco, F., Pecoraino, G., Salerno, G., Sciotto, M., Bellomo, S., Di Grazia, G., Ferrari, F., Gattuso, A., La Pica, L., Mattia, M., Pisciotta, A. F., Pruiti, L., and Sortino, F.: Inferences on the 2021 Ongoing Volcanic Unrest at Vulcano Island (Italy) through a Comprehensive Multidisciplinary Surveillance Network, Remote Sensing, 15, 1405, https://doi.org/10.3390/rs15051405, 2023.

Finnegan, D. L., Kotra, J. P., Hermann, D. M., and Zoller, W. H.: The use of7LiOH-impregnated filters for the collection of acidic gases and analysis by instrumental neutron activation analysis, Bull Volcanol, 51, 83–87, https://doi.org/10.1007/BF01081977, 1989.

Flaconneche, B., Martin, J., and Klopffer, M. H.: Transport Properties of Gases in Polymers: Experimental Methods, Oil & Gas Science and Technology - Rev. IFP, 56, 245–259, https://doi.org/10.2516/ogst:2001022, 2001.

Geil, B.: Methodenentwicklung zur Halogenbestimmung von vulkanischen Systemem mittels basischer Fallen und Diffusionsabscheidern/Entwicklung einer permeablen Chlorgasquelle, Master thesis, Mainz, Johannes Gutenberg-Universität, Mainz, 2021.

Giggenbach, W. F.: A simple method for the collection and analysis of volcanic gas samples, Bull Volcanol, 39, 132–145, https://doi.org/10.1007/BF02596953, 1975.

Glasow, R. von and Crutzen, P. J.: Model study of multiphase DMS oxidation with a focus on halogens, 2003.

Glasow, R. von: Atmospheric chemistry in volcanic plumes, Proceedings of the National Academy of Sciences of the United States of America, 107, 6594–6599, https://doi.org/10.1073/pnas.0913164107, 2010.

Glasow, R. von, Bobrowski, N., and Kern, C.: The effects of volcanic eruptions on atmospheric chemistry, Chemical Geology, 263, 131–142, https://doi.org/10.1016/j.chemgeo.2008.08.020, 2009.

Gliß, J., Bobrowski, N., Vogel, L., Pöhler, D., and Platt, U.: OClO and BrO observations in the volcanic plume of Mt. Etna – implications on the chemistry of chlorine and bromine species in volcanic plumes, Atmos. Chem. Phys., 15, 5659–5681, https://doi.org/10.5194/acp-15-5659-2015, 2015.

Grob, R. L. and Barry, E. F.: Modern Practice of Gas Chromatography, Wiley, 2004.

Gross, J. H.: Massenspektrometrie, Springer Berlin Heidelberg, Berlin, Heidelberg, 2019.

Gutmann, A., Bobrowski, N., Liotta, M., and Hoffmann, T.: Bromine speciation in volcanic plumes: new in situ derivatization LC-MS method for the determination of gaseous hydrogen bromide by gas diffusion denuder sampling, Atmos. Meas. Tech., 14, 6395–6406, https://doi.org/10.5194/amt-14-6395-2021, 2021.

Gutmann, A., Bobrowski, N., Roberts, T. J., Rüdiger, J., and Hoffmann, T.: Advances in Bromine Speciation in Volcanic Plumes, Front. Earth Sci., 6, https://doi.org/10.3389/feart.2018.00213, 2018.

Haddad, P. R.: Ion chromatography: Principles and applications, Journal of chromatography library, v. 46, Elsevier, New York, 776 pp., 1990.

Hägg, M.-B.: Membrane purification of Cl2 gas, Journal of Membrane Science, 177, 109–128, https://doi.org/10.1016/S0376-7388(00)00455-5, 2000.

Hoffmann, T., O'Dowd, C. D., and Seinfeld, J. H.: Iodine oxide homogeneous nucleation: An explanation for coastal new particle production, Geophysical Research Letters, 28, 1949–1952, https://doi.org/10.1029/2000GL012399, 2001.

Hu, Q., Noll, R. J., Li, H., Makarov, A., Hardman, M., and Graham Cooks, R.: The Orbitrap: a new mass spectrometer, Journal of mass spectrometry JMS, 40, 430–443, https://doi.org/10.1002/jms.856, 2005.

Huang, R.-J. and Hoffmann, T.: Diffusion technique for the generation of gaseous halogen standards, Journal of chromatography. A, 1217, 2065–2069, https://doi.org/10.1016/j.chroma.2010.01.078, 2010.

INGV: Bollettino Settimanale sul monitoraggio multiparametrico del vulcano Etna, https://www.ct.ingv.it/index.php/monitoraggio-e-sorveglianza/prodotti-del-monitoraggio/bollettini-settimanali-multidisciplinari, last access: 1 December 2025, 2022-2023.

Jordan, A., Harnisch, J., Borchers, R., Le Guern, F., and Shinohara, H.: Volcanogenic Halocarbons, Environ. Sci. Technol., 34, 1122–1124, https://doi.org/10.1021/es990838q, 2000.

Karbach, N., Bobrowski, N., and Hoffmann, T.: Observing volcanoes with drones: studies of volcanic plume chemistry with ultralight sensor systems, Scientific reports, 12, 17890, https://doi.org/10.1038/s41598-022-21935-5, 2022.

Kuhn, J., Bobrowski, N., and Platt, U.: The Interface Between Magma and Earth's Atmosphere, Geochem Geophys Geosyst, 23, https://doi.org/10.1029/2022GC010671, 2022.

La Spina, A., Burton, M., Salerno, G., and Caltabiano, T.: Insights into magma dynamics at Etna (Sicily) from SO2 and HCl fluxes during the 2008–2009 eruption, Geology, 51, 419–423, https://doi.org/10.1130/G50707.1, 2023.

Makarov, A.: Electrostatic axially harmonic orbital trapping: a high-performance technique of mass analysis, Analytical chemistry, 72, 1156–1162, https://doi.org/10.1021/ac991131p, 2000.

Marécal, V., Voisin-Plessis, R., Roberts, T. J., Aiuppa, A., Narivelo, H., Hamer, P. D., Josse, B., Guth, J., Surl, L., and Grellier, L.: Halogen chemistry in volcanic plumes: a 1D framework based on MOCAGE 1D (version R1.18.1) preparing 3D global chemistry modelling, Geosci. Model Dev., 16, 2873–2898, https://doi.org/10.5194/gmd-16-2873-2023, 2023.

Marshall, A. G., Hendrickson, C. L., and Jackson, G. S.: Fourier transform ion cyclotron resonance mass spectrometry: A primer, Mass Spectrom. Rev., 17, 1–35, https://doi.org/10.1002/(SICI)1098-2787(1998)17:1<1:AID-MAS1>3.0.CO;2-K, 1998.

Martin, R. S., Mather, T. A., and Pyle, D. M.: High-temperature mixtures of magmatic and atmospheric gases, Geochem Geophys Geosyst, 7, https://doi.org/10.1029/2005GC001186, 2006.

Mather, T. A., Tsanev, V. I., Pyle, D. M., McGonigle, A. J. S., Oppenheimer, C., and Allen, A. G.: Characterization and evolution of tropospheric plumes from Lascar and Villarrica volcanoes, Chile, J. Geophys. Res., 109, https://doi.org/10.1029/2004JD004934, 2004.

Mercalli and Silvestri: Le eruzioni dell'isola di Vulcano, incominciate il 3 Agosto 1888 e terminate il 22 Marzo 1980, Ann Uff Cent Meteor Geodin 10(4):10-50, 1891, 1891.

Moretti, R., Métrich, N., Arienzo, I., Di Renzo, V., Aiuppa, A., and Allard, P.: Degassing vs. eruptive styles at Mt. Etna volcano (Sicily, Italy). Part I: Volatile stocking, gas fluxing, and the shift from low-energy to highly explosive basaltic eruptions, Chemical Geology, 482, 1–17, https://doi.org/10.1016/j.chemgeo.2017.09.017, 2018.

Muizebelt, W. J. and Nivard, R. J. F.: The mechanism of the iodine-catalyzed thermal isomerization of substituted ethylenes, Chem. Commun. (London), 148, https://doi.org/10.1039/C19650000148, 1965.

Narivelo, H., Hamer, P. D., Marécal, V., Surl, L., Roberts, T., Pelletier, S., Josse, B., Guth, J., Bacles, M., Warnach, S., Wagner, T., Corradini, S., Salerno, G., and Guerrieri, L.: A regional modelling study of halogen chemistry within a volcanic plume of Mt Etna's Christmas 2018 eruption, Atmos. Chem. Phys., 23, 10533–10561, https://doi.org/10.5194/acp-23-10533-2023, 2023.

Nies, A., Roberts, T. J., Dayma, G., Fischer, T. P., and Kuhn, J.: Reactive bromine in volcanic plumes confines the emission temperature and oxidation of magmatic gases at the atmospheric interface, Science advances, 11, eadt8607, https://doi.org/10.1126/sciadv.adt8607, 2025.

Pacholec, F., Eaton, D. R., and Rossi, D. T.: Characterization of mixtures of organic acids by ion-exclusion partition chromatography-mass spectrometry, Anal. Chem., 58, 2581–2583, https://doi.org/10.1021/ac00125a051, 1986.

Platt, U. and Stutz, J.: Differential Absorption Spectroscopy, in: Differential Optical Absorption Spectroscopy, Springer Berlin Heidelberg, Berlin, Heidelberg, 135–174, https://doi.org/10.1007/978-3-540-75776-4_6, 2008.

Pyle, D. M. and Mather, T. A.: Halogens in igneous processes and their fluxes to the atmosphere and oceans from volcanic activity: A review, Chemical Geology, 263, 110–121, https://doi.org/10.1016/j.chemgeo.2008.11.013, 2009.

Roberts, T. J., Vignelles, D., Liuzzo, M., Giudice, G., Aiuppa, A., Coltelli, M., Salerno, G., Chartier, M., Couté, B., Berthet, G., Lurton, T., Dulac, F., and Renard, J.-B.: The primary volcanic aerosol emission from Mt Etna: Size-resolved particles with SO2 and role in plume reactive halogen chemistry, Geochimica et Cosmochimica Acta, 222, 74–93, https://doi.org/10.1016/j.gca.2017.09.040, 2018.

Roberts, T. J., Jourdain, L., Griffiths, P. T., and Pirre, M.: Re-evaluating the reactive uptake of HOBr in the troposphere with implications for the marine boundary layer and volcanic plumes, Atmos. Chem. Phys., 14, 11185–11199, https://doi.org/10.5194/acp-14-11185-2014, 2014.

Roberts, T. J., Braban, C. F., Martin, R. S., Oppenheimer, C., Adams, J. W., Cox, R. A., Jones, R. L., and Griffiths, P. T.: Modelling reactive halogen formation and ozone depletion in volcanic plumes, Chemical Geology, 263, 151–163, https://doi.org/10.1016/j.chemgeo.2008.11.012, 2009.

Rüdiger, J., Tirpitz, J.-L., Moor, J. M. de, Bobrowski, N., Gutmann, A., Liuzzo, M., Ibarra, M., and Hoffmann, T.: Implementation of electrochemical, optical and denuder-based sensors and sampling techniques on UAV for volcanic gas measurements: examples from Masaya, Turrialba and Stromboli volcanoes, Atmos. Meas. Tech., 11, 2441–2457, https://doi.org/10.5194/amt-11-2441-2018, 2018.

Rüdiger, J., Bobrowski, N., Liotta, M., and Hoffmann, T.: Development and application of a sampling method for the determination of reactive halogen species in volcanic gas emissions, Analytical and bioanalytical chemistry, 409, 5975–5985, https://doi.org/10.1007/s00216-017-0525-1, 2017.

Saiz-Lopez, A. and Glasow, R. von: Reactive halogen chemistry in the troposphere, Chemical Society reviews, 41, 6448–6472, https://doi.org/10.1039/C2CS35208G, 2012.

Sawyer, G. M., Carn, S. A., Tsanev, V. I., Oppenheimer, C., and Burton, M.: Investigation into magma degassing at Nyiragongo volcano, Democratic Republic of the Congo, Geochem Geophys Geosyst, 9, https://doi.org/10.1029/2007GC001829, 2008.

Schönhardt, A., Richter, A., Theys, N., and Burrows, J. P.: Space-based observation of volcanic iodine monoxide, Atmos. Chem. Phys., 17, 4857–4870, https://doi.org/10.5194/acp-17-4857-2017, 2017.

Small, H., Stevens, T. S., and Bauman, W. C.: Novel ion exchange chromatographic method using conductimetric detection, Anal. Chem., 47, 1801–1809, https://doi.org/10.1021/ac60361a017, 1975.

Stoiber, R. E., Williams, S. N., and Huebert, B.: Annual contribution of sulfur dioxide to the atmosphere by volcanoes, Journal of Volcanology and Geothermal Research, 33, 1–8, https://doi.org/10.1016/0377-0273(87)90051-5, 1987.

Surl, L., Roberts, T., and Bekki, S.: Observation and modelling of ozone-destructive halogen chemistry in a passively degassing volcanic plume, Atmos. Chem. Phys., 21, 12413–12441, https://doi.org/10.5194/acp-21-12413-2021, 2021.

Symonds, R. B., Gerlach, T. M., and Reed, M. H.: Magmatic gas scrubbing: implications for volcano monitoring, Journal of Volcanology and Geothermal Research, 108, 303–341, https://doi.org/10.1016/S0377-0273(00)00292-4, 2001.

Symonds, R. B., Rose, W. I., and Reed, M. H.: Contribution of C1- and F-bearing gases to the atmosphere by volcanoes, Nature, 334, 415–418, https://doi.org/10.1038/334415a0, 1988.

Thermo Fischer: Orbitrap mass spectrometers offer the highest levels of accuracy and precision, https://www.thermofisher.com/de/de/home/industrial/mass-spectrometry/liquid-chromatography-mass-spectrometry-lc-ms/lc-ms-systems/orbitrap-lc-ms.html, 2026.

Weiss, J.: Handbook of Ion Chromatography, Wiley, 2004.

Wittmer, J., Bobrowski, N., Liotta, M., Giuffrida, G., Calabrese, S., and Platt, U.: Active alkaline traps to determine acidic-gas ratios in volcanic plumes: Sampling techniques and analytical methods, Geochem Geophys Geosyst, 15, 2797–2820, https://doi.org/10.1002/2013GC005133, 2014.

11 Appendix

A Tables

B Figures

C: Supplemental Information

1 Standard preparation

1-Iodo-2,4,6-trimethoxybenzene (I-TMB)

2 mmol of each 1,3,5-Trimethoxybenzene (0,336 mg) and Iodine (0.508 g) were solved in 20 mL glacial acetic acid and stirred at RT for 48 hours in the dark. 1 Liter of pure water was added until there was no more precipitation. The residue was filtered, solved in 15 mL of DCM and washed three times with 10 mL of 0.01 M NaOH followed by three times with 10 mL water. The solution was dried with 2 g of $MgSO_4$. The organic solvent was evaporated under reduced pressure. The solid was recrystallized two times using 5 mL of ethanol. The yellow crystals were characterized by GC-HRMS m/z: 294.9747 (M+); 0.48 g (81 %).

1-bromo-2-chloro-1,2-diphenylethane (Stilbene bromide chloride, S-BrCl)

19 mmol of trans-stilbene (3.5 g) and 19 mmol of N-bromoacetamide (2.6 g) were solved in 100 mL MTBE and 50 mL Ethanol and stirred for 30 min. 4 mL HCl (30 %) was added dropwise. The solution first turned yellowish and became clear after stirring for 1 hour. A colorless solid precipitated after colling to – 20 °C. The solid was filtered, washed with cool water (3 x 10 mL), recrystallized in petroleum ether and characterized by GC-HRMS m/z: 215.0622 ($C14H10Br^+$), 168.9648 ($C7H6Br^+$); 3.82 g (68 %)

2 Extraction process filter

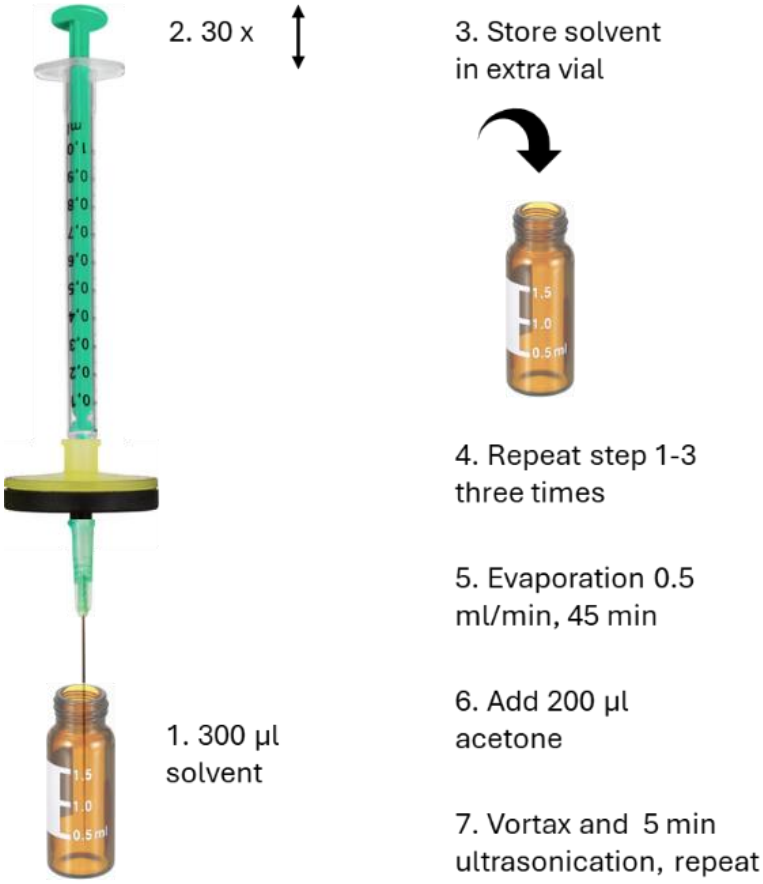

Figure 26: Extraction process scheme for derivatization filters.

Fill 300 µL of solvent in a GC-Vial, extract the solvent thirty times through the filter with a syringe and transfer the solution into another GC-Vial. Repeat this step again 3 times to a total of 1.2 ml of solution. Evaporate the solvent, add 200 µL of acetone. Vortex the solution and sonicate it for 5 min, repeat this step.

3 Output rate Chlorine Source

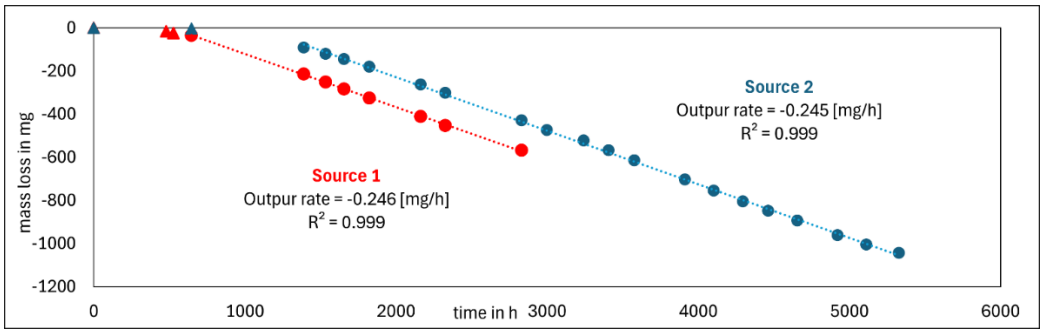

Figure 27: Mass loss of chlorine permeation sources with corresponding output rates. Triangles: non steady state.

Date	Time	Time Difference	Aver. Cl1	Aver Cl2	Mass loss Cl1	Mass loss Cl2
		[h]			[mg]	[mg]
19.03.24	10:30	0	50.2200	78.2700	0.00	0.00
08.04.24	10:30	480.00	50.2037	78.2743	-16.3	4.3
10.04.24	10:30	528.00	50.1970	78.2710	-23.0	1.0
15.04.24	09:30	647.00	50.1851	78.2671	-34.9	-2.9
16.05.24	11:00	1391.00	50.0060	78.1783	-214.0	-91.7
22.05.24	10:15	1534.25	49.9689	78.1498	-251.1	-120.2
27.05.24	13:00	1657.00	49.9371	78.1249	-282.9	-145.1
03.06.24	12:30	1824.50	49.8949	78.0899	-325.1	-180.1
17.06.24	15:00	2163.00	49.8092	78.0083	-410.8	-261.7
24.06.24	10:00	2326.00	49.7671	77.9696	-452.9	-300.4
15.07.24	11:15	2831.25	49.6523	77.8419	-567.7	-428.1
22.07.24	11:15	2999.25	49.6246	77.7964	-595.4	-473.6
30.07.24	14:00	3241.75	49.5996	77.7472	-620.4	-522.8
06.08.24	10:30	3406.25	49.5817	77.7024	-638.3	-567.6
13.08.24	14:00	3577.75	49.5659	77.6553	-654.1	-614.7
27.08.24	13:30	3913.25	49.5400	77.5674	-680.0	-702.6
04.09.24	11:30	4103.25	49.5288	77.5151	-691.2	-754.9
12.09.24	11:00	4294.75	49.5190	77.4657	-701.0	-804.3
19.09.24	11:00	4462.75	49.5110	77.4215	-709.0	-848.5
27.09.24	13:00	4656.75	49.5034	77.3771	-716.6	-892.9
08.10.24	14:00	4921.75	49.4948	77.3091	-725.2	-960.9
16.10.24	13:00	5112.75	49.4890	77.2655	-731.0	-1004.5
25.10.24	13:30	5329.25	49.4825	77.2260	-737.5	-1044.0
18.11.24	15:30:	5907.25	49.4696	77.1380	-750.4	-1132.0

4 GC-Measurements

PTV

PTV (Stilbene)	Rate [°C/s]	T [°C]	Hold time [min]	Split flow [mL/min]
Start		70		
Injection		70	3	
Transfer	14.5	200	1	
Cleaning	14.5	280	1	50

Oven program

Time [min]	Rate [°C/min]	T [°C]	Hold time [min]
2	0	40	2
6	30	160	0
16.5	4	190	3
22.4	80	260	5

PTV

PTV (TMB)	Rate [°C/s]	T [°C]	Hold time [min]	Split flow [mL/min]
Start		270		
Injection		270	0	
Transfer	14.5	270	1	
Cleaning	14.5	310	3	100

Oven program

Time [min]	Rate [°C/min]	T [°C]	Hold time [min]
0	0	90	3
15	10	210	0
18.6	7	235	0
24.3	20	250	5

4.1 HRMS-Spectra

Stilbene derivates Chromatograms, chamber experiments

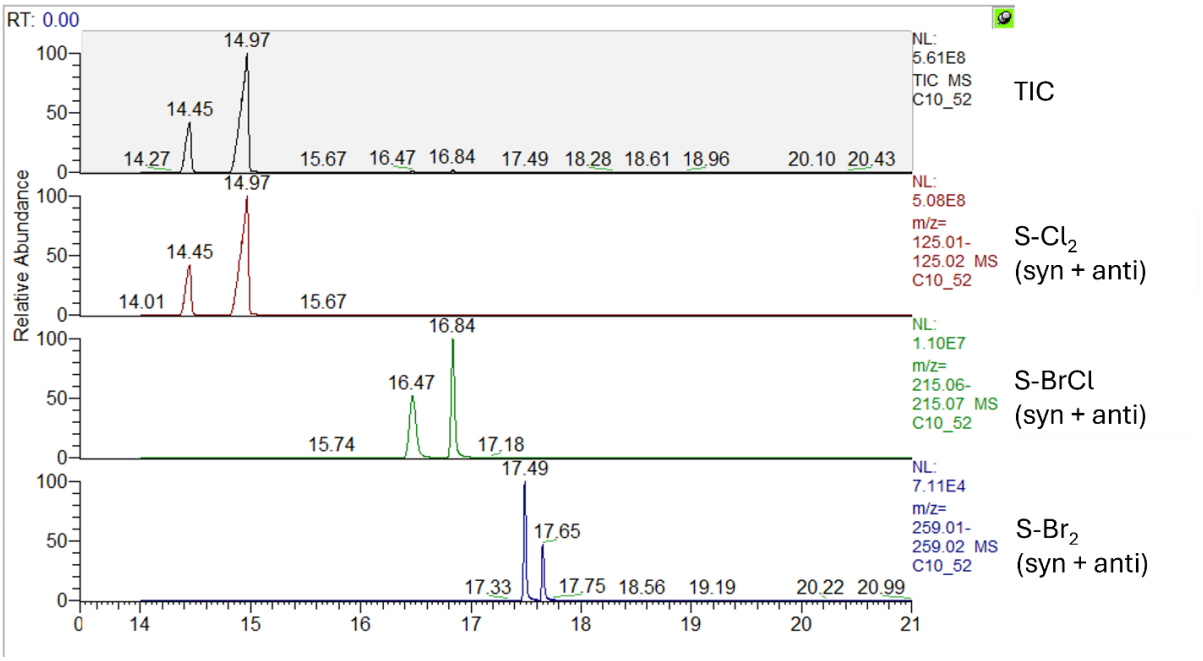

S-Cl2

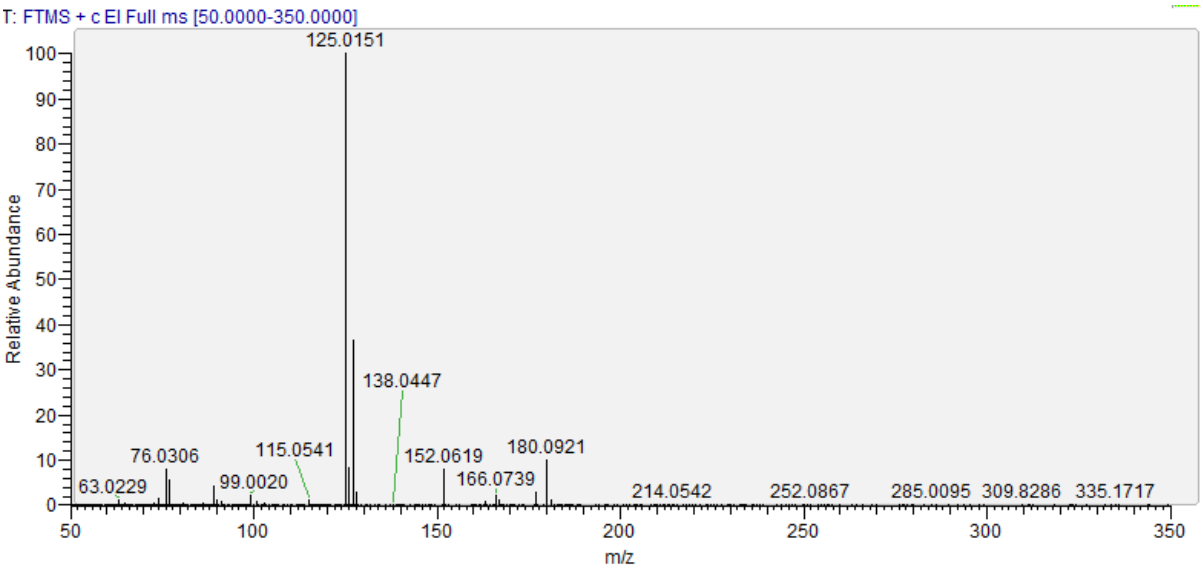

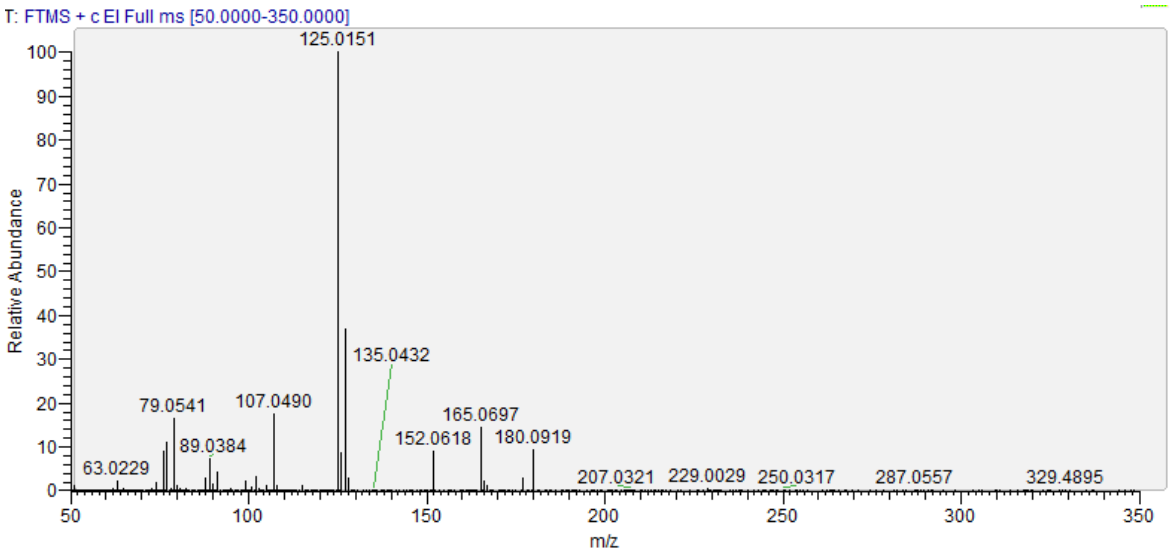

Figure 28: HRMS of S-Cl2 (Retention time: 14.4 (top) and 14.7 min (bottom) with characteristic mass fragments.

m/z: 125.0151 $C_7H_6{}^{35}Cl^+$

127.0122 $C_7H_6{}^{37}Cl^+$

180.0919 $C_{14}H_{12}^+$

165.0697 $C_{13}H_9^+$

152.0618 $C_{12}H_8^+$

S-BrCl

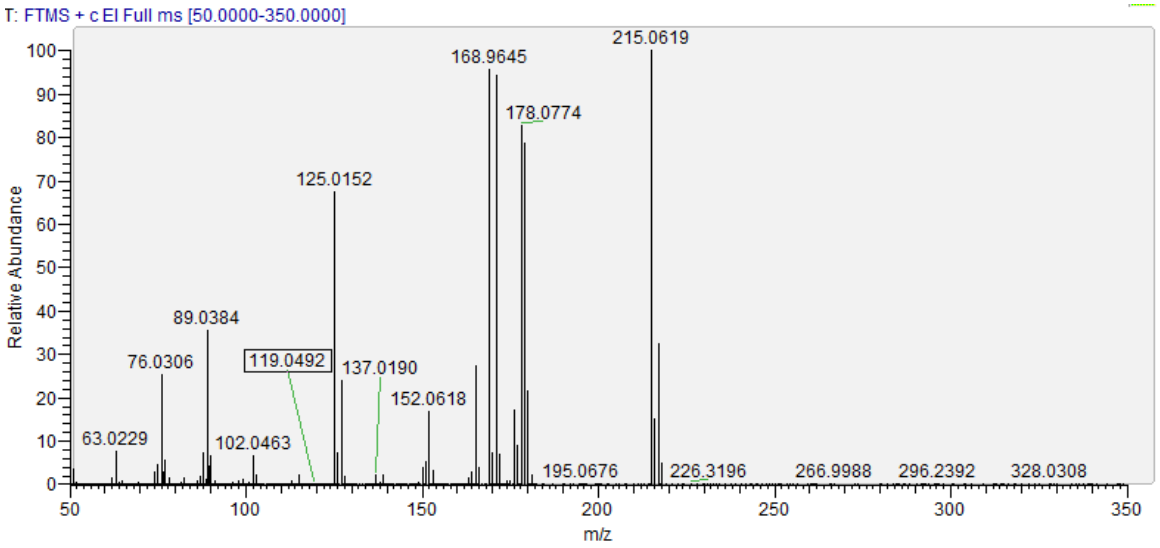

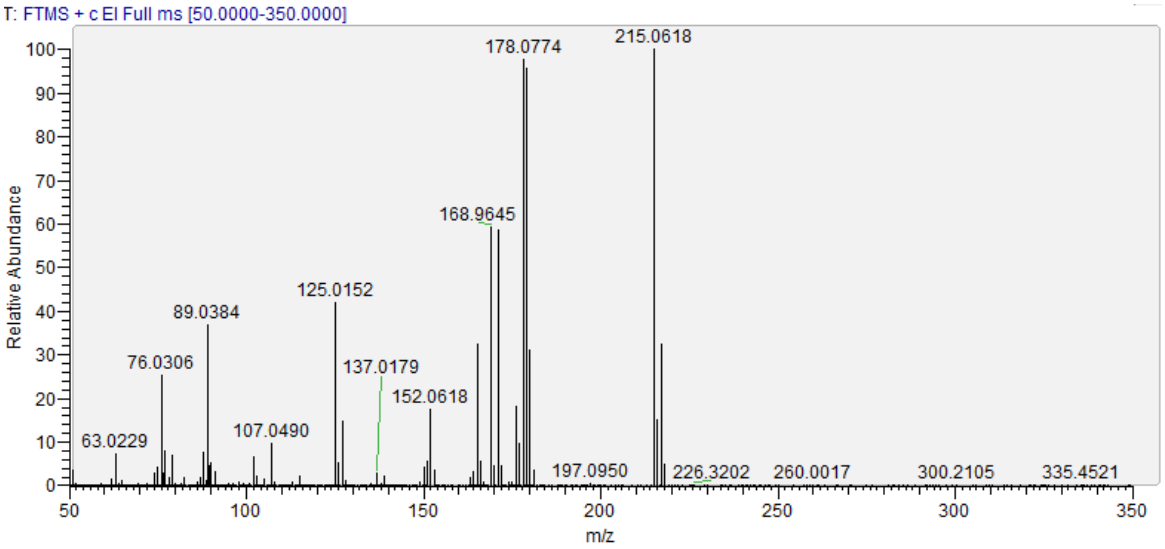

Figure 29: HRMS of S-BrCl (Retention time: 16.5 (top) and 16.8 min (bottom) with characteristic mass fragments.

m/z:	215.0618	$C_{14}H_{12}{}^{35}Cl^+$
	217.0590	$C_{14}H_{12}{}^{37}Cl^+$
	168.9645	$C_7H_6{}^{79}Br^+$
	170.9624	$C_7H_6{}^{81}Br^+$
	125.0151	$C_7H_6{}^{35}Cl^+$
	127.0122	$C_7H_6{}^{37}Cl^+$
	178.0774	$C_{14}H_{10}^+$
	152.0618	$C_{12}H_8^+$

S-Br2

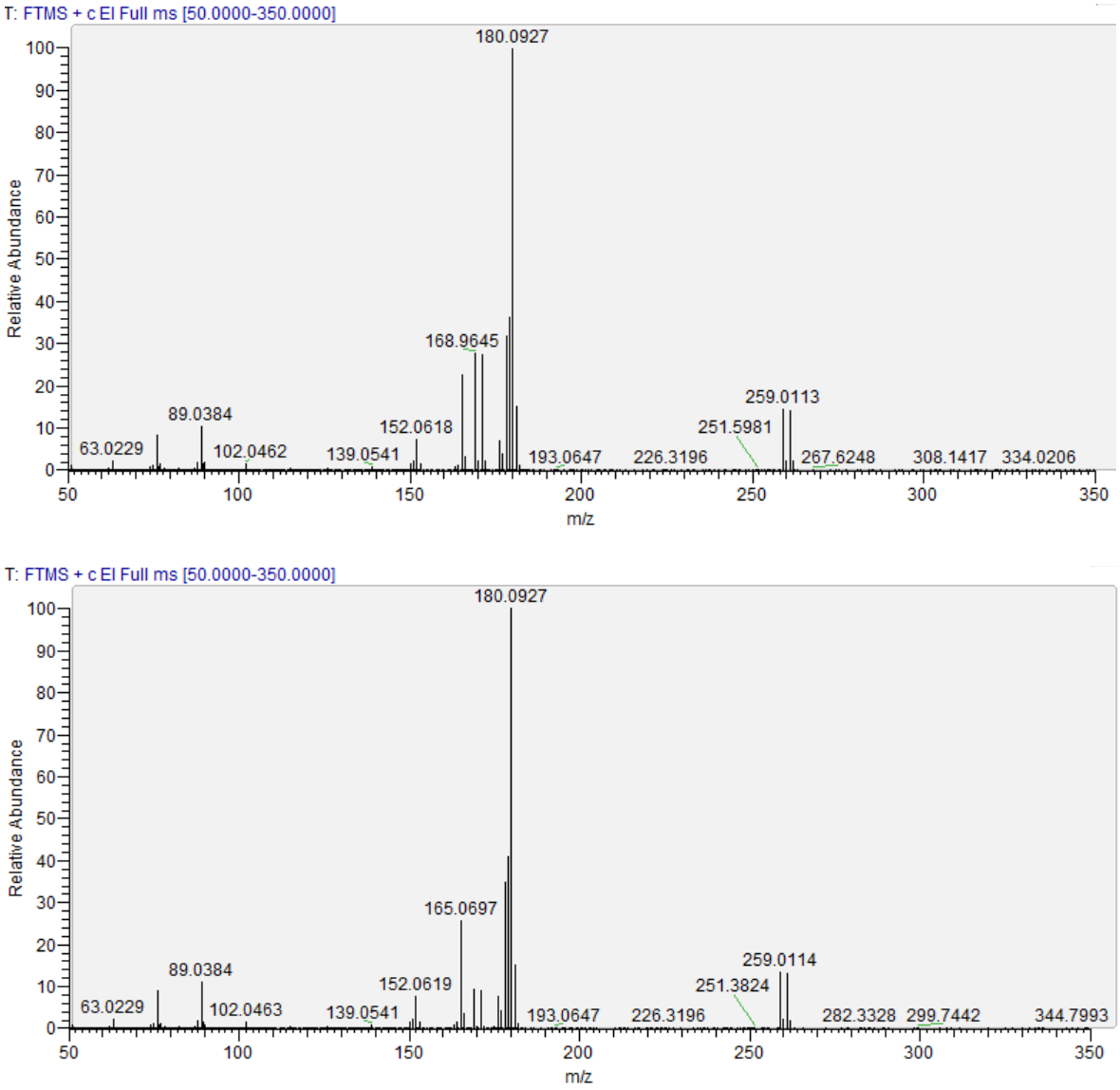

Figure 30: HRMS of S-Br2 (Retention time: 17.5 (top) and 17.7 min (bottom) with characteristic mass fragments.

m/z:	215.0618	$C_{14}H_{12}{}^{79}Br^+$
	217.0590	$C_{14}H_{12}{}^{81}Br^+$
	165.0697	$C_{13}H_9^+$
	180.0927	$C_{14}H_{12}^+$
	152.0618	$C_{12}H_8^+$

TMB derivates Chromatograms, chamber experiments

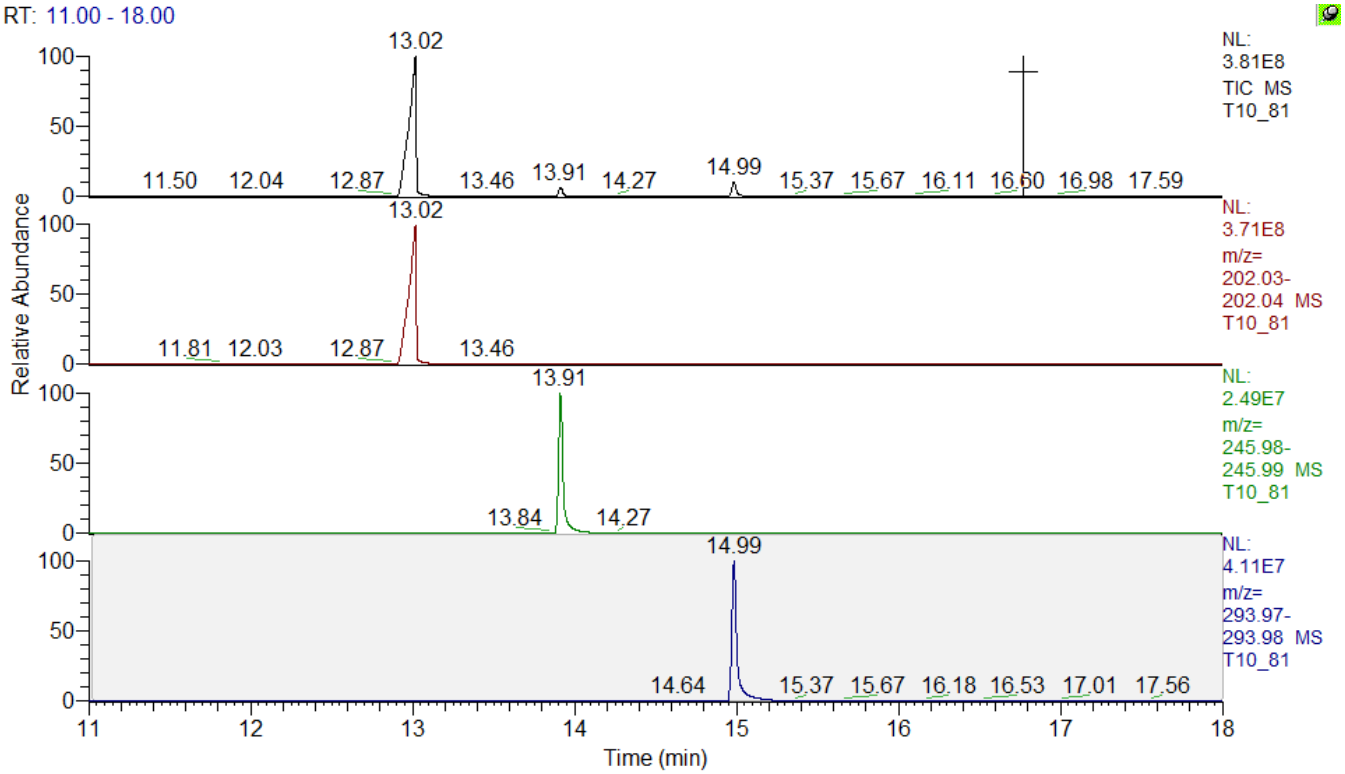

Cl-TMB

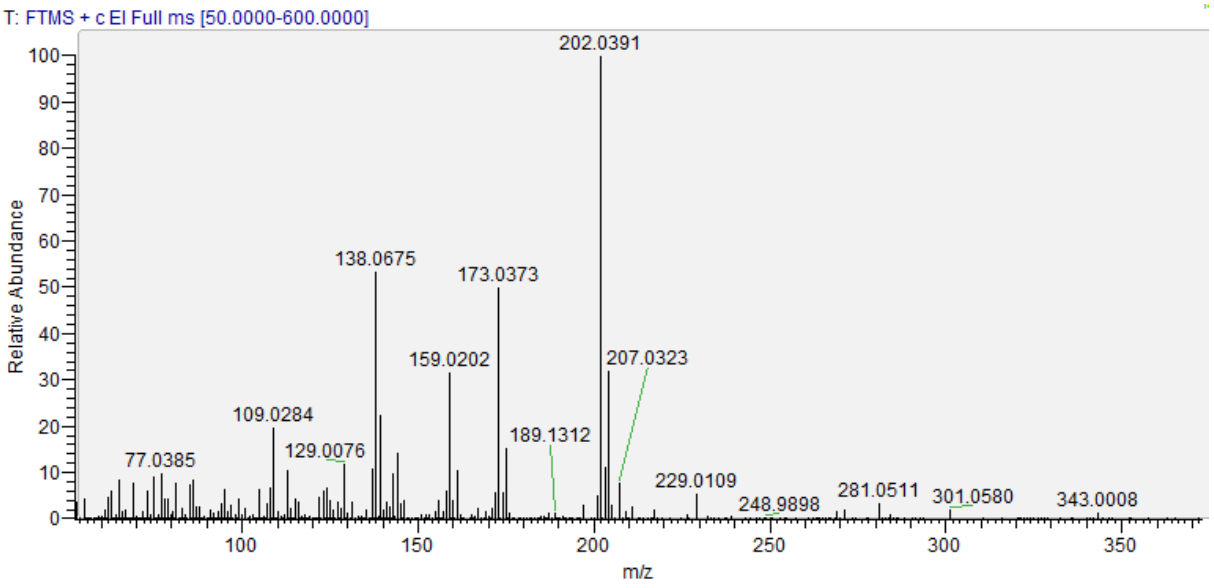

Figure 31: HRMS of Cl-TMB (Retention time: 13.0 min) with characteristic mass fragments.

m/z: 202.0391 $C_9H_{11}{}^{35}ClO_3^+$

204.0361 $C_9H_{11}{}^{37}ClO_3^+$

173.0373 $C_8H_{10}{}^{35}ClO_2^+$

159.0202 $C_7H_8{}^{35}ClO_2^+$

Br-TMB

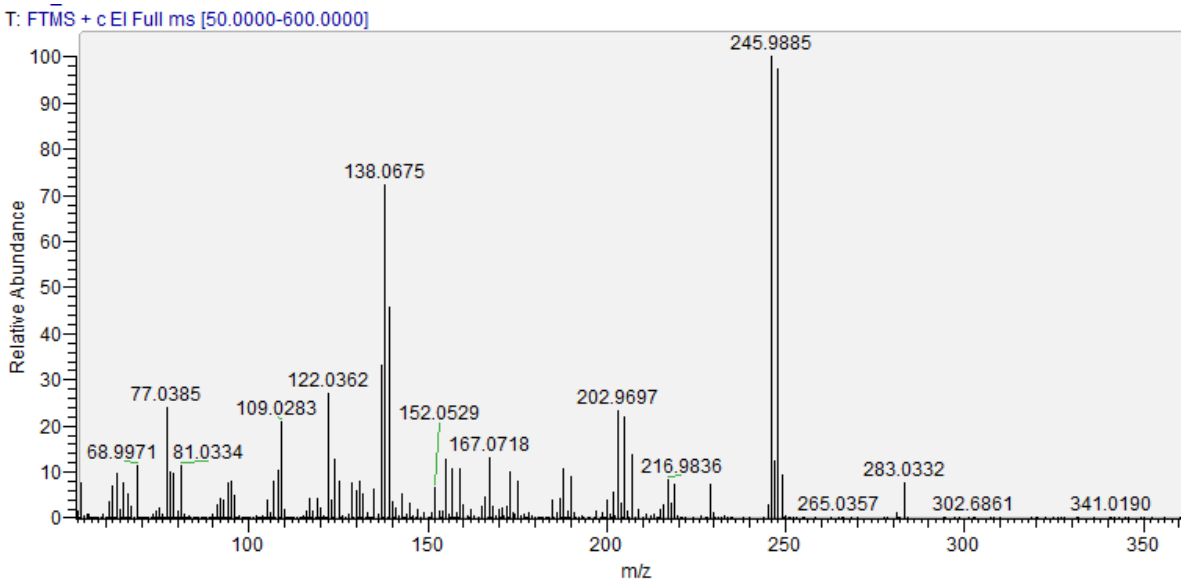

Figure 32: HRMS of Br-TMB (Retention time: 14.0 min) with characteristic mass fragments.

m/z: 245.9885 $C_9H_{11}{}^{79}BrO_3^+$

247.9864 $C_9H_{11}{}^{81}BrO_3^+$

202.9697 $C_7H_8{}^{79}BrO_2^+$

204.9684 $C_7H_8{}^{81}BrO_2^+$

138.0675 $C_8H_{10}O_2^+$

I-TMB

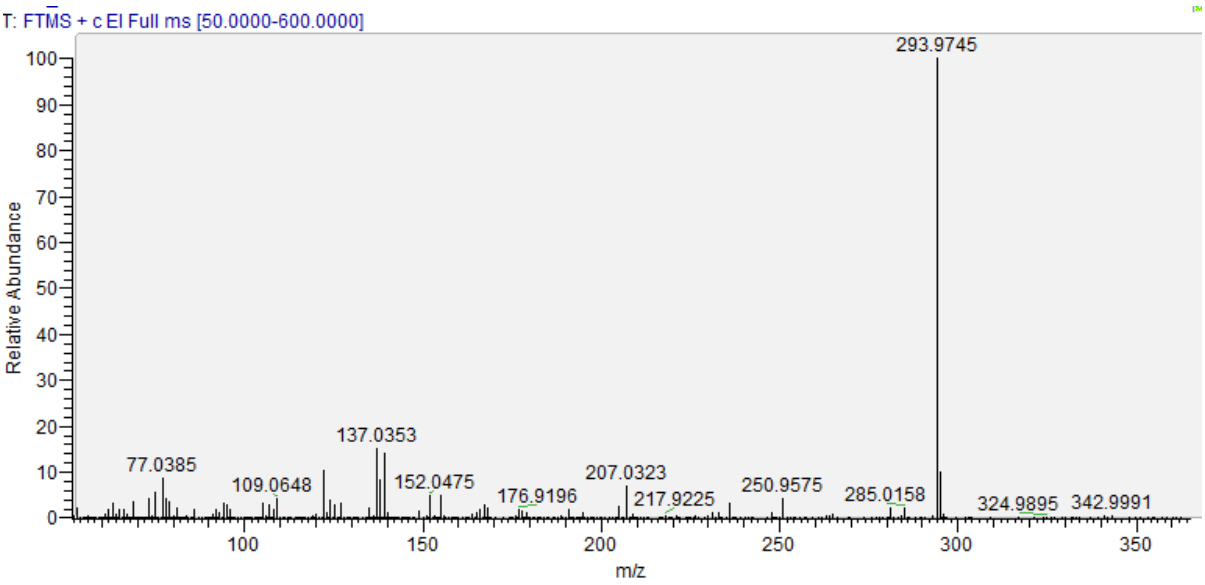

Figure 33:HRMS of I-TMB (Retention time: 15.0 min) with characteristic mass fragments.

m/z: 293.9745 $C_9H_{11}IO_3^+$

5 Recovery rates

Alkaline trap

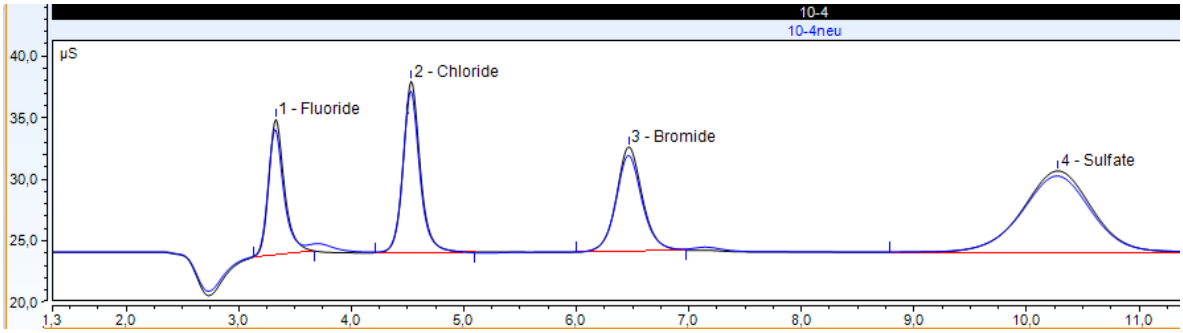

Figure 34: Chromatogram of two analyte solutions. Recovery rates for all analytes are 95 % due to dilution with wet cation exchange resin. Comparison of untreated solution (black) and neutralized solution with the same concentration of analytes (blue)

Cis-stilbene

Method	Reaction product	Volumn [µL]	Concentration [µg/L]	Recovery rate [%]
Stilbene Filter	S-Cl_2 S-BrCl S-Br_2	200	50	85 ± 1 90 ± 1 96 ± 1
			750	89 ± 1 94 ± 1 98 ± 1

TMB

Method	Reaction product	Volumn [µL]	Concentration [µg/L]	Recovery rate [%]
TMB Filter	Cl-TMB Br-TMB I-TMB	200	50	82 ± 1 88 ± 1 97 ± 1
			750	92 ± 1 91 ± 1 92 ± 1

6 LOD/LOQ

***Cis*-stilbene**							
c(solution)	S-Cl2	S-BrCl	S-Br2				
ppt	**Area (syn+anti)**	**Area (syn+anti)**	**Area (syn+anti)**	**RPG Funktion**			**ppt**
0	0.00E+00	0.00E+00	0.00E+00	S-Cl2		LOD	1299
500	5.66E+04	9.54E+03	4.65E+02	102.99119	34180.610		
500	5.33E+04	9.68E+03	1.88E+02	1.7690225	40543.047		
1000	1.11E+05	2.08E+04	1.13E+03	0.9991156	73829.937		
1000	1.04E+05	2.11E+04	8.85E+02	3389.4832	3		
5000	5.16E+05	9.64E+04	7.45E+03	1.847E+13	1.635E+10		
5000	5.12E+05	9.73E+04	7.78E+03				
10000	1.34E+06	2.32E+05	2.37E+04	S-BrCl		LOD	535
10000	1.02E+06	1.93E+05	1.57E+04	20.269736	1017.1099		
50000	5.10E+06	9.85E+05	9.47E+04	0.1434692	3288.077		
50000	5.23E+06	1.04E+06	9.83E+04	0.9998497	5987.6732		
100000	1.31E+07	2.63E+06	2.79E+05	19960.815	3		
100000	1.34E+07	2.72E+06	2.97E+05	7.156E+11	107556692		
500000	6.07E+07	1.30E+07	1.37E+06				
500000	6.23E+07	1.36E+07	1.45E+06	S-Br2		LOD	898
1000000	1.56E+08	3.67E+07	4.13E+06	1.9504956	910.33366		
1000000	1.33E+08	3.33E+07	3.72E+06	0.0231556	530.68904		
5000000	8.46E+08	2.48E+08	3.38E+07	0.9995773	966.39847		
5000000	8.58E+08	2.66E+08	3.65E+07	7095.3819	3		
				6.627E+9	2801778.0		
LOD/LOQ							
		S-CL2	S-BrCl	S-Br2			
LOD Calibration [ppt]		1299	535	898			Sample Volume [L]
Recovery/Collection		1493	582	926			0.0002
Molar Mass g/mol		251.16	259.61	340.06			
Mass ng	LOD	0.30	0.12	0.19		Air sample	
	LOQ	0.90	0.35	0.56		n(Air)	15 min, 250 ml/min
ppt	LOD	7.1	2.7	3.3		0.167	
ppt	LOQ	21	8.0	9.8			

TMB							
c(solution)	Cl-TMB	Br-TMB	I-TMB				
ppt	**Area**	**Area**	**Area**	**LOD**			**ppt**
100	9.97E+03	4.00E+04	1.90E+04	Cl-TMB		LOD	409
100	6.39E+03	2.42E+04	1.22E+04	3.99E+01	1.14E+04		
500	2.77E+04	2.39E+04	4.67E+04	9.83E-01	4.94E+03		
500	2.75E+04	2.24E+04	4.44E+04	9.98E-01	8.29E+03		
1000	5.77E+04	3.33E+04	7.77E+04	1.64E+03	3.00E+00		
1000	5.97E+04	3.50E+04	8.15E+04	1.13E+11	2.06E+08		
5000	2.30E+05	1.57E+05	3.83E+05				
5000	2.08E+05	1.42E+05	3.49E+05				
10000	4.12E+05	2.85E+05	7.02E+05	Br-TMB		LOD	736
10000	3.99E+05	2.69E+05	6.60E+05	2.61E+01	1.66E+04		
50000	1.79E+06	1.23E+06	2.95E+06	1.16E+00	5.82E+03		
50000	1.84E+06	1.26E+06	3.10E+06	9.94E-01	9.76E+03		
100000	3.42E+06	2.39E+06	5.99E+06	5.07E+02	3.00E+00		
100000	3.21E+06	2.31E+06	5.73E+06	4.83E+10	2.86E+08		
500000	1.64E+07	1.20E+07	3.12E+07				
500000	1.60E+07	1.19E+07	3.03E+07				
1000000	3.24E+07	2.49E+07	6.51E+07	I-TMB		LOD	293
1000000	3.17E+07	2.46E+07	6.39E+07	6.75E+01	1.35E+04		
5000000	1.79E+08	1.39E+08	3.69E+08	1.19E+00	6.00E+03		
5000000	1.82E+08	1.39E+08	3.68E+08	9.99E-01	1.01E+04		
				3194.77558	3		
				3.2406E+11	304307740		
LOD/LOQ							
		Cl-TMB	Br-TMB	I-TMB			
LOD Calibration [ppt]		409	736	293			Sample Volume [L]
Recovery/Collection		470	800	302			0.0002
Molar Mass g/mol		251.16	259.61	340.06			
Mass ng	LOD	0.094	0.16	0.060		Air sample	
	LOQ	0.28	0.48	0.18		n(Air)	15 min, 250 ml/min
ppt	LOD	2.2	3.7	1.1		0.167	
ppt	LOQ	6.7	11	3.2			

Bubbler		fluorid	chlorid	bromid	sulfat
konz Cl,S	konz F,Br	Area	Area	Area	Area
5.0E-06	5.0E-08	0.00E+00	1.43E-01	8.50E-04	2.26E-01
5.0E-06	5.0E-08	0.00E+00	1.44E-01	7.04E-04	2.30E-01
1.0E-05	1.0E-07	1.01E-03	2.29E-01	1.74E-03	4.43E-01
1.0E-05	1.0E-07	8.63E-04	2.32E-01	1.50E-03	4.45E-01
2.5E-05	2.5E-07	3.42E-03	5.65E-01	4.60E-03	1.11E+00
2.5E-05	2.5E-07	3.49E-03	5.65E-01	4.26E-03	1.11E+00
5.0E-05	5.0E-07	7.79E-03	1.15E+00	9.55E-03	2.27E+00
5.0E-05	5.0E-07	7.36E-03	1.15E+00	9.62E-03	2.27E+00
1.0E-04	1.0E-06	1.54E-02	2.42E+00	2.01E-02	4.67E+00
1.0E-04	1.0E-06	1.42E-02	2.42E+00	2.02E-02	4.66E+00
5.0E-04	5.0E-06	9.50E-02	1.52E+01	1.01E-01	2.74E+01
5.0E-04	5.0E-06	8.93E-02	1.52E+01	9.98E-02	2.73E+01
1.0E-03	1.0E-05	1.87E-01	3.34E+01	1.98E-01	6.05E+01
1.0E-03	1.0E-05	1.84E-01	3.33E+01	1.98E-01	6.01E+01
5.0E-03	5.0E-05	8.70E-01	1.85E+02	1.08E+00	3.39E+02
5.0E-03	5.0E-05	8.71E-01	1.84E+02	1.08E+00	3.38E+02

Fluoride				Chloride			
18736.2918	-0.0018844	LOD	1.31E-07	24116.8398	-0.013617894	LOD	2.03E-06
323.905652	0.00074319			288.520414	0.014852497		
0.99761481	0.00188523			0.99885632	0.031684744		
3346.03309	8			6986.95112	8		
0.01189212	2.8433E-05			7.01436088	0.008031384		

Bromide				Sulfat			
20447.7371	-0.00046726	LOD	1.67E-08	46770.7336	-0.03335954	LOD	9.41E-07
200.415804	0.00010317			259.151337	0.01334063		
0.99923206	0.00022009			0.99975445	0.02845949		
10409.421	8			32571.7773	8		
0.00050424	3.8753E-07			26.3812683	0.00647954		

		F	Cl	Br	S	Sample Volume		
LOD	Mol/L	1.31E-07	2.03E-06	1.67E-08	9.41E-07	0.008		
	Mol	1.05E-09	1.63E-08	1.33E-10	7.53E-09			
Recovery/Collection	Mol	1.10E-09	1.71E-08	1.40E-10	7.93E-09	Recovery Rate/Collection Efficiency		
Molare Masse		HF	HCl	HBr	SO2	0.95		
		20.01	36.46	80.91	64.06			
Masse [g]		2.21E-08	6.24E-07	1.13E-08	5.08E-07			
ug	LOD	0.022	0.62	0.011	0.51		Air sample	
ug	LOQ	0.066	1.9	0.034	1.5		n(Air)	15 min, 250 ml/min
ppb	LOD	6.6	102	0.84	47		0.1674075	
ppb	LOQ	20	307	2.5	142			

7 Python Code Figure 22:

```
import pandas as pd
import matplotlib.pyplot as plt
import numpy as np
from scipy.ndimage import gaussian_filter1d

# Aktualisierte Daten
data = {
  "time_min": [0.55, 0.75, 1.9, 1.3, 6, 6, 3.433333333, 0.9, 7.733333333, 1.1],
  "BrCl": [0.003273534, 0.022730419, 0.01244697, 0.064726774, 0.012558147,
0.011742061,
       0.016315529, 0.038783419, 0.021054015, np.nan],
  "Br2": [0.000408942, 0.001857634, 0.001153276, 0.004585409, 0.000408119,
0.000304614,
       0.000442268, 0.004631337, 0.00056115, np.nan],
  "BrOH": [0.155783686, 0.398570647, 0.96871345, np.nan, 0.176798755,
0.177718346,
       0.432675688, np.nan, 0.259770256, 0.724]
}

df = pd.DataFrame(data).sort_values("time_min")

# Fehlende Werte interpolieren
df = df.interpolate(method="linear", limit_direction="both")

# Interpolation auf gleichmäßige Zeitabstände
time_interp = np.linspace(df["time_min"].min(), df["time_min"].max(), 400)
df_interp = pd.DataFrame({"time_min": time_interp})
for col in ["BrCl", "Br2", "BrOH"]:
  df_interp[col] = np.interp(time_interp, df["time_min"], df[col])

# Stärkere Glättung mit Gaußfilter
df_smooth = df_interp.copy()
for col in ["BrCl", "Br2", "BrOH"]:
  df_smooth[col] = gaussian_filter1d(df_interp[col], sigma=10)

# Schriftgrößen
label_size = 16
title_size = 18
legend_size = 15
tick_size = 14

# Zwei Plots nebeneinander, mit größerem Abstand
fig, axes = plt.subplots(1, 2, figsize=(14, 5.5), gridspec_kw={'wspace': 0.4})

# Gesamtansicht
axes[0].stackplot(
  df_smooth["time_min"],
  df_smooth["Br2"],
```

```
    df_smooth["BrCl"],
    df_smooth["BrOH"],
    labels=["Br₂", "BrCl", "BrOH (BrONO, BrONO₂)"],
    colors=["#cb181d", "#fee391", "#fcae91"],
    alpha=0.9
)
axes[0].set_xlabel("Time [min]", fontsize=label_size)
axes[0].set_ylabel("Fraction of total bromine", fontsize=label_size)
axes[0].set_ylim(0, 1)
axes[0].set_xlim(0.55, 7.7334)
axes[0].legend(loc="upper right", frameon=False, fontsize=legend_size)
axes[0].set_title("Bromine speciation (relative to total Br, smoothed)",
fontsize=title_size, pad=25)
axes[0].tick_params(axis='both', labelsize=tick_size)

# Vergrößerter Ausschnitt (0.55–2.2 min, 0–0.07) leicht nach links verschoben
pos = axes[1].get_position()
axes[1].set_position([pos.x0 - 0.04, pos.y0, pos.width, pos.height])

axes[1].stackplot(
    df_smooth["time_min"],
    df_smooth["Br2"],
    df_smooth["BrCl"],
    df_smooth["BrOH"],
    colors=["#cb181d", "#fee391", "#fcae91"],
    alpha=0.9
)
axes[1].set_xlim(0.55, 2.2)
axes[1].set_ylim(0, 0.07)
axes[1].set_xlabel("Time [min]", fontsize=label_size)
axes[1].set_ylabel("Fraction of total bromine (zoomed)", fontsize=label_size)
axes[1].set_title("Zoom: early plume evolution", fontsize=title_size, pad=25)
axes[1].tick_params(axis='both', labelsize=tick_size)

plt.show()
```

EGU2022, Vienna

Halogen measurements with *in-situ* sampling techniques: Studies at Vulcano and Mt. Etna (Italy)

Bastien Geil[1], Xochilt Gutiérrez[1], Niklas Karbach[1], Nicole Bobrowski[2,3], and Thorsten Hoffmann[1]

- [1]Johannes Gutenberg-Universität, Anorganische Chemie und Analytische Chemie, AK Hoffmann, Mainz, Germany (bageil@uni-mainz.de)
- [2]Institute of Environmental Physics, Ruprecht-Karls-University Heidelberg, Germany
- [3]Istituto Nazionale di Geofisica e Vulcanologia – Osservatorio Etneo, Catania, 95125, Italy

Halogens in volcanic plumes are important for both volcanic and environmental research. For example, changes in the composition of the volcanic plume can be an indication of changes in the activity of the volcano. In addition to entrained air components, volcanic plumes consist mainly of SO_2, CO_2, and H_2O. However, HF, HCl and HBr are also significant constituents of volcanic emissions. A particularly interesting element in this context is bromine because of its atmospheric relevance, but also since BrO forms in the volcanic plume and, like SO_2, can be determined spectroscopically using remote sensing techniques, making it ideal for monitoring and surveillance of volcanoes. However, to interpret and use BrO concentrations, we need a fully understanding of the formation and evolution of BrO in volcanic plumes. A step forward can be gained by measuring all relevant halogen species.

Currently, several methods are used to detect the various halogen compounds. Remote sensing methods exist for only a few so we use *in-situ* sampling methods such as diffusion separators, filter packs or aqueous alkali traps to collect reactive and total halogen species, respectively.

In this study, we will present the results of total fluorine, chlorine, bromine and sulfur as well as CO_2 and their ratios between, for field campaigns at a closed volcanic system - Vulcano in September 2019 and October 2020 and at an open vent volcano Mt Etna in July 2021. The results will be discussed in the light of the different degassing activity and therefore different temperature and will be compared to earlier studies at Masaya, Nyamuragira and Etna.

EGU 2023, Vienna

Detection of chlorine, bromine and bromine chloride (BrCl) in volcanic emissions: Studies at Mt. Etna (Italy), 2022

Bastien Geil[1], Niklas Karbach[1], Nicole Bobrowski[2,3], and Thorsten Hoffmann[1]

- [1]Johannes Gutenberg-University, Department Chemistry, Mainz, Germany (bageil@uni-mainz.de)
- [2]Institute of Environmental Physics, Ruprecht-Karls-University, Germany
- [3]Istituto Nazionale di Geofisica e Vulcanologia - Osservatorio Etneo, Italy

Halogens in volcanic plumes are important for both volcanic and environmental research. For example, changes in the composition of the volcanic plume can be an indication of changes in the activity of the volcano. Volcanic emissions consist mainly of emitted H_2O, CO_2 and SO_2 and are rapidly mixed with surrounding background atmosphere. Additionally, HF, HCl and HBr are also significant constituents of volcanic emissions.

A particularly interesting element in this context is bromine because of its atmospheric relevance. Among others BrO forms in the volcanic plume and, like SO_2, can be determined spectroscopically using remote sensing techniques, making it ideal for monitoring and surveillance of volcanoes. However, to interpret and use BrO concentrations, we need to fully understand the formation and evolution of BrO in volcanic plumes. Measuring all relevant halogen species can take us one step further in our understanding of the interaction between atmosphere and volcanic gas and particle emissions.

Currently, several methods are used to detect the various halogen compounds. Remote sensing methods exist for only a few (in general BrO, OClO, HCl, HF). We use *in-situ* sampling methods such as diffusion separators, filter packs or aqueous alkaline traps to collect reactive and total halogen species, respectively.

In this study, we will present results for Cl_2, Br_2 and BrCl in volcanic plumes using AV based *in-situ* measurement with *cis*-Stilbene coated syringe filters for halogens and interhalogens (i.e., Cl_2, Br_2 and BrCl). The results are discussed considering the different degassing activities and halogen chemistry in volcanic plumes.

EGU 2024, Vienna

Halogen activation in volcanic plumes: Studies at Mt Etna (Italy) 2022 and 2023

Bastien Geil[1], Nicole Bobrowski[2,3], Niklas Karbach[1], Jonas Kuhn[4], Alexander Nies[5], Tjarda Roberts[5], Peter Hoor[6], and Thorsten Hoffmann[1]

- [1]Johannes Gutenberg-University, Department of Chemistry, AK Hoffmann, Mainz, Germany (bageil@uni-mainz.de)
- [2]Institute of Environmental Physics, Ruprecht-Karls-University, Germany
- [3]Istituto Nazionale di Geofisica e Vulcanologia - Osservatorio Etneo, Italy
- [4]Department of Atmospheric and Oceanic Sciences, University of California, LA, USA
- [5]LPC2E, CNRS/Universite d´Orleans, Orleans, France
- [6]Institute for Atmospheric Physics, Johannes Gutenberg-Universität, Mainz, Germany

Halogens in volcanic plumes are important for both volcanic and environmental research. For example, changes in the composition of the volcanic plume can be an indication of changes in the activity of the volcano. Volcanic emissions consist mainly of emitted H_2O, CO_2 and SO_2 and are rapidly mixed with surrounding background atmosphere. Additionally, HF, HCl and HBr are also significant constituents of volcanic emissions.

The halogens are of particular interest for atmospheric chemistry. They are oxidized by mixing with the atmosphere. In this context, BrO should be mentioned as it is one of the oxidation products and like SO_2, can be measured spectroscopically using remote sensing technique and therefore making it nearly ideal for surveillance of volcanoes. However only, if the oxidation process is understood, the composition of the volcanic plume at the emission site can be traced and thus possibly the changes in volcanic activity can be understood. Furthermore, these results are essential for the improvement of the atmospheric impact of volcanic halogens.

Currently, several methods are used to detect the various halogen compounds. Remote sensing methods exist for only a few (in general BrO, OClO, HCl, HF). We use *in-situ* sampling methods such as *cis*-Stilbene coated syringe filter and aqueous alkaline traps to collect reactive and total halogen species, respectively.

In this presentation, we will show quantitative results of samples taken in July 2022, June 2023 and in August 2023 for Cl_2, Br_2, BrCl, total bromine and sulfur from measurements of the Bocca Nuova and South East crater plume, Mt. Etna, Italy using

UAV based in situ measurements in various distances to those emission sources. The results confirm the increase of reactive bromine and show for the first time the differentiation into Cl_2, Br_2, BrCl and total bromine and sulfur. Also BrO/SO_2 values analyzed from DOAS measurements taken further downwind during the campaign will be presented.

CCVG 2022, Peru

Halogen measurements with *in-situ* sampling techniques: Studies at Mt. Etna (Italy)

Geil B. (1), X. Gutiérrez (1), N. Karbach (1), N. Bobrowski (2,3), T. Hoffmann (1)
(1) Johannes Gutenberg-Universität, Anorganische Chemie und Analytische Chemie, Germany
(2) Institute of Environmental Physics, Ruprecht-Karls-University, Germany
(3) Istituto Nazionale di Geofisica e Vulcanologia – Osservatorio Etneo, Italy

Halogens in volcanic plumes are important for both volcanic and environmental research. For example, changes in the composition of the volcanic plume can be an indication of changes in the activity of the volcano. Volcanic plumes consist mainly of emitted H_2O, CO_2 and SO_2 and rapidly mixed-in background atmosphere. Additionally, HF, HCl and HBr are also significant constituents of volcanic emissions. A particularly interesting element in this context is bromine because of its atmospheric relevance. Among others BrO forms in the volcanic plume and, like SO_2, can be determined spectroscopically using remote sensing techniques, making it ideal for monitoring and surveillance of volcanoes. However, to interpret and use BrO concentrations, we need to fully understand of the formation and evolution of BrO in volcanic plumes. Measuring all relevant halogen species can take us one step further in our understanding of the interaction between atmosphere and volcanic gas and particle emissions. Currently, several methods are used to detect the various halogen compounds. Remote sensing methods exist for only a few (in general BrO, OClO, HCl, HF). We use *in-situ* sampling methods such as diffusion separators, filter packs or aqueous alkali traps to collect reactive and total halogen species, respectively. In this study, we will present total concentrations of fluorine, chlorine, bromine, and sulfur as well as CO_2 and the ratios between them obtained during two field campaigns at Mt Etna in July 2021 and July 2022. In addition, we performed a new UAV based *in-situ* measurement using *cis*-Stilben coated syringe filters for halogens in the oxidation state zero (i.e., Cl_2 and Br_2). The results are discussed in light of the different degassing activities and halogen chemistry in volcanic plumes.

Halogen measurements with in-situ sampling techniques: Studies at Mt. Etna (Italy)

B.Geil[1]✉ ,N. Bobrowski[2,3] ,N. Karbach[1], X. Gutierrez[1] and T. Hoffmann[1]✉

[1]Department Chemistry; Johannes Gutenberg University Mainz, Germany (✉ hoffmant@uni-mainz.de, bageil@uni-mainz.de)
[2]Institute of Environmental Physics, Ruprecht-Karls-University Heidelberg, Germany
[3]Istituo Nazionale di Geofisica e Vulcanologia – Osservatorio Etneo, Catania, Italy

JOHANNES GUTENBERG UNIVERSITÄT MAINZ

TeMaS Terrestrial Magmatic Systems

ISTITUTO NAZIONALE DI GEOFISICA E VULCANOLOGIA

Introduction

Halogens in volcanic plumes are important for both volcanic and environmental research. Volcanic plumes consist mainly of released H_2O, CO_2, and SO_2. In addition, HF, HCl, and HBr are also important components of volcanic emissions. A particularly interesting element in this context is bromine. BrO can be determined spectroscopically using remote sensing techniques, making it ideal for monitoring.
Therefore, we use in situ sampling methods such as diffusion denuders, filter packs, or aqueous alkali traps to collect reactive or total halogen species.
At Mt. Etna, Italy, we used a new UAV-based in situ measurement technique with cis-Stilbene-coated syringe filters to determine elemental halogens (Cl_2, Br_2) and interhalogen compounds (e.g., BrCl), as well as total halogen concentrations via alkali traps.

Sampling Site, Mt. Etna, Italy 2022

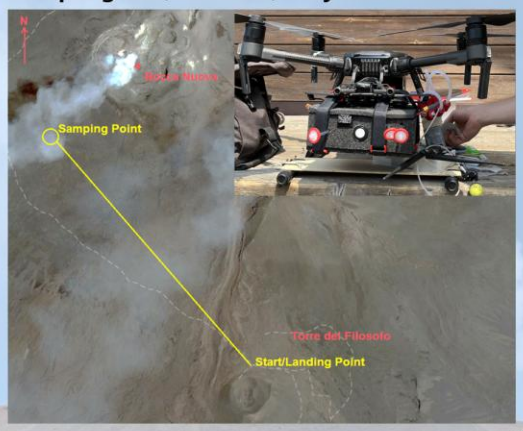

Experimental Setup "Syringe Filter"

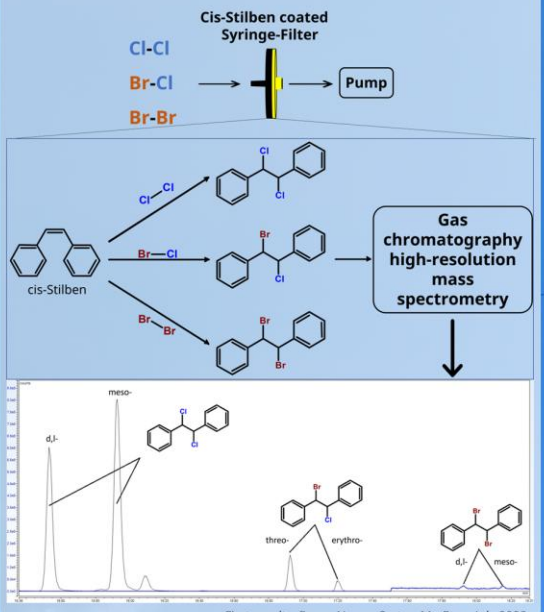

First results, Bocca Nuova Crater, Mt. Etna, July 2022

Experimental Setup "Bubbler"

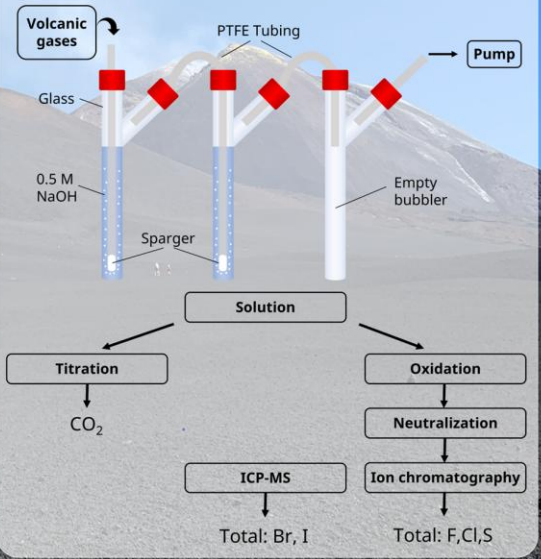

Conclusion and Outlook

With our new method, we are not only able to distinguish the reactive halogen species, but we have also succeeded in realizing a very lightweight setup for in situ measurements using drones (UAVs) directly in the volcanic plume. The combination of bubblers and filters allows the simultaneous measurement of the individual halogen species as well as the total halogen concentration.

Next steps:

- Quantification of all the halogen species
- Detection and quantification of new species with improved coatings for syringe filters
- Improvement of theoretical models for evolution of halogen species in volcanic plumes

Picture: Bastien Geil, Mt Etna 2022

Quantification of Chlorine (Cl_2), Bromine chloride (BrCl) and Bromine (Br_2) in volcanic plumes via drone-based measurements: Studies at Mt Etna (Italy)

Bastien Geil, Johannes Gutenberg-University Mainz, Germany
Nicole Bobrowski, Istituto Nazionale di Geofisica e Vulcanologica, Italy
Niklas Karbach, Johannes Gutenberg-University Mainz, Germany
Alexander Nies, LPC2E, CNRS/Université d´Orleans, France
LMD/IPSL, ENS, Sorbonne Université Paris, France
Tjarda Roberts, LMD/IPSL, ENS, Sorbonne Université Paris, France
LPC2E, CNRS/Université d´Orleans, France
Thorsten Hoffmann, Johannes Gutenberg-University Mainz, Germany

Halogens are a key component of volcanic emissions, and the ratio of halogens to quasi-inert dilution tracers (e.g., S_{total}) serves as a potential indicator of changes in volcanic activity. Only a limited number of halogen species (e.g., BrO, OClO, HCl, HF) can be reliably quantified by remote sensing. BrO, for instance, forms through the oxidation of HBr via reactions with ambient O_3 and OH. Understanding these rapid oxidation processes—occurring within minutes of emission—is essential for linking remote observations to source conditions and volcanic activity.

We conducted UAV-based *in-situ* sampling at varying distances (10–5300 m) from the Bocca Nuova crater (Mt. Etna) during field campaigns in 2022 and 2023. Reactive halogen species (HalX) were collected using *cis*-stilbene- and trimethoxybenzene-coated syringe filters as *in-situ* derivatization agents, while total halogen and sulfur contents were collected using aqueous alkaline traps.

We present quantitative results for total chlorine, bromine, sulfur, and for the first time, differentiate Cl_2, Br_2, and BrCl in volcanic plumes. The maximum observed molar Hal/S_{total} ratios in 2022 were $Cl_2 = 7 \times 10^{-5}$, $BrCl = 3 \times 10^{-4}$, and $Br_2 = 2 \times 10^{-5}$. HBr was oxidized within two minutes ($BrX/Br_{total} = 0.98$, 114 s). Our data confirm a rapid increase in reactive bromine with plume age and reveal a clear chemical distinction between reactive halogen species and total halogen content.

This dataset provides novel constraints on reactive halogen chemistry in young volcanic plumes and supports the development of future plume chemistry models for improved monitoring and interpretation of volcanic activity.

Quantification of Chlorine (Cl_2), Bromine chloride (BrCl) and Bromine (Br_2) in volcanic plumes via drone-based measurements: Studies at Mt. Etna (Italy)

B.Geil[1]✉ ,N. Bobrowski[2,3] ,N. Karbach[1] , A. Nies[4,5] ,T. Roberts[4,5] and T. Hoffmann[1]✉

[1]Department Chemistry, Johannes Gutenberg University Mainz, Germany (hoffmant@uni-mainz.de, bageil@uni-mainz.de)
[2]Institute of Environmental Physics, Ruprecht-Karls-University Heidelberg, Germany
[3]Istituto Nazionale di Geofisica e Vulcanologia – Osservatorio Etneo, Catania, Italy
[4] LPC2E, CNRS/Université d´Orleans, France
[5] LMD/IPSL, ENS, Sorbonne Université Paris, France

Motivation

- Halogens are key components in volcanic emissions
- Halogen-to-sulphur ratios can serve as indicators of volcanic activity
- Remote sensing quantifies a limited subset of halogen species (e.g., BrO, OClO, HCl, HF)
- Plume oxidation processes need to be understood to reveal source composition from oxidized halogen measurements in downwind plumes

Background

- Fast oxidation of halogen species via O_3 and HO_x within minutes after emission
- Understanding these fast reactions is essential to interpret remote sensing data
- UAVs enable direct in situ sampling at multiple distances from vent
- Reactive halogen species can be stabilised by derivatisation (cis-stilbene, TMB)

Goals

- Conduct UAV-based in situ sampling of volcanic plumes at Etna (2022/2023)
- Collect both total halogen and sulphur (alkaline trap) and reactive halogen species (derivatisation filters)
- Provide quantitative in plume differentiation of Cl_2, Br_2 and BrCl
- Quantify conversion of halides into reactive halogen species
- Deliver new constrains for volcanic plume chemistry and modelling

Methods and Measurements

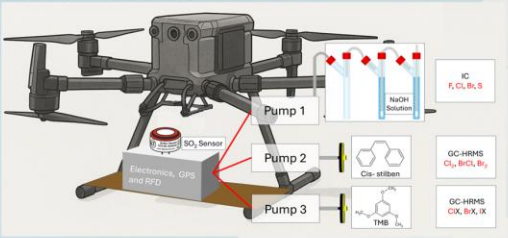

- **Alkaline trap (NaOH):** total amounts of halogen and sulphur via ion chromatography
- **Cis stilbene filter:** in situ derivatisation with chlorine (Cl_2), bromine (Br_2) and bromine chloride (BrCl) with subsequent quantification by mass spectrometry.
- **TMB filter:** in situ derivatisation with non-radical reactive halogen species (RHS, oxidation state 0 and +1; e.g., ClX, BrX, IX) with subsequent quantification by mass spectrometry

Reactive halogen speciation

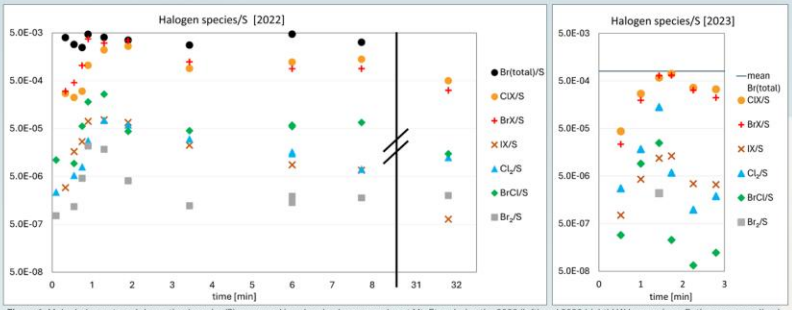

Figure 1. Molar halogen-to-sulphur ratios (species/S) measured in volcanic plume samples at Mt. Etna during the 2022 (left) and 2023 (right) UAV campaigns. Ratios are normalised to total sulphur, and individual data points represent sampling intervals within the first minutes after emission. Species derived from derivatisation filter analyses. Note that 2022 data extend to later plume ages, while 2023 sampling focussed on the early plume (< 3 min).

BrX denotes non-radical bromine species with oxidation state 0 or +1 (e.g. HOBr, $BrONO_2$, BrCl, Br_2). Reduced bromine (HBr) and to the best of our knowledge radical species (Br·, BrO) are not included.

Results:

- **Species detected:** Cis-stilbene filters quantified Cl_2, Br_2, and BrCl; TMB filters trapped BrX, ClX, and IX (non-radical RHS, halogens in oxidation state 0 or +1).

Temporal evolution:

- All released halogen species (HBr, HCl, HI) changed strongly within the first minutes after emission.
- BrX, ClX and IX increased rapidly after emission, with a clear peak around ~2 min.
- The maxima of Cl_2, BrCl, and Br_2 were reached **right before the BrX maximum**, showing a short temporal offset between interhalogen release and the bulk BrX peak.
- BrCl, and Br_2 are only a minor fraction of the combined species that lead to the BrX signal (ca. 5-10%).

Late-plume behaviour:

- Minor increases in Cl_2, Br_2, and BrCl were observed in later sampling points, superimposed on the overall decline.
- IX species declined most rapidly, almost to complete loss within minutes.
- BrX decreased at an intermediate rate, while ClX remained comparatively stable.

Interannual contrasts:

- 2022: Br_2 was detected; BrCl stabilised at later plume ages. **BrCl > Cl_2**; higher bromine concentration leads to higher formation of BrCl
- 2023: Br_2 remained below LOD; BrCl declined continuously. **BrCl < Cl_2**; lower bromine concentration restrained formation of BrCl
- These observations demonstrate clear year-to-year variability in bromine behaviour, consistent across the differences between total Br/S ratios and speciation patterns.

Interpretation[1-4]:

Initial oxidation (0–2 min):

- OH-initiated reactions convert HBr/HCl to radicals
- (e.g., OH + HBr → Br + H_2O), which react rapidly with O_3 and HO_2 to form HOBr and HOCl.
- These HOX species most likely dominate the BrX and ClX signals, while the directly measured interhalogens (Cl_2, Br_2, BrCl) account for only minor fractions. Additional contributions from halogen nitrates (e.g., $BrONO_2$, $ClONO_2$) are possible but could not be quantified with the present method

Interhalogen release (1–2 min):

- The maxima of Cl_2, BrCl, and Br_2 slightly **preceding the BrX peak** indicate that heterogeneous release in droplets can occur very rapidly once HOX is available, potentially reaching its maximum earlier than the gas-phase HOX pool. A partial contribution from sampling resolution cannot be excluded.

Photolysis and loss (>2 min):

- Photodissociation of ClX, BrX and IX species shifts the budget toward radicals. IX loss also reflects iodine's particle uptake.

Broader implication:

- The strong interannual contrast in Br-speciation, consistent with differences in Br/S ratios, underlines bromine's sensitivity and central role in linking magmatic degassing with plume chemistry.

References:
[1] Rüdiger et al.; ACP, 21, 3371-3393, 2021, https://doi.org/10.5194/acp-21-3371-2021
[2] Glasow: Environmental Science, 107, 12, 6594-6599, 2009 https://doi.org/10.1073/pnas.0913164107
[3] Bobrowski et al.; J. Geoohys. Res., 112, 1-17, 2007, https://doi:10.1029/2006JD007206
[4] Roberts et al.; ACP, 14, 5, 11201-11219, 2014, https://doi.org/10.5194/acpd-14-5445-2014

Alkaline trap

	Molar mean ± standard deviation		
	F/S	Cl/S	Br/S
2022	0.25 ± 0.09	1.6 ± 1.1	(3.6 ± 0.8) • 10^{-3}
2023	0.14 ± 0.06	2.4 ± 1.4	(8.0 ± 0.6) • 10^{-4}

Cl/S: Remained broadly constant across 2022 and 2023, pointing to relatively stable chlorine degassing behavior.
F/S: Showed small inter-annual differences, which could be linked to variable fluorine retention in the melt or changes in eruptive activity.
Br/S: Exhibited the strongest and most significant change between years, highlighting the particular sensitivity of bromine release.
Interpretation: These differences could be driven by variations in magmatic conditions (volatile budget, melt–fluid partitioning) as well as by differences in volcanic activity
Key point: The pronounced Br/S variability is mirrored by the reactive halogen speciation (BrX, BrCl, Br_2), where bromine species also show strong year-to-year contrasts. This coupling underlines bromine's central role in linking magmatic degassing with plume chemistry.

Cl_2, BrCl, Br_2, BrO, IO, $BrONO_2$, SO_2, OClO, ...

↑ Oxidation by ambient air (Ozone, HO_x)

HCl, HBr, HI, SO_2 ....

Conclusion & Outlook

- Halogen/sulphur ratios reveal stable Cl degassing but variable Br and F, reflecting magmatic controls.
- Time-resolved speciation shows rapid halide oxidation to HOX, heterogeneous release of interhalogens, and fast iodine loss by photolysis.
- Open questions remain on the exact HOX composition, the role of halogen nitrates, and the radical budget.
- Future work should integrate radical detection, particle-phase iodine speciation, petrological constraints and chemical modelling to fully link magmatic sources with atmospheric impacts.

Anakon 2025, Leipzig

Drones as flying measuring platforms: halogen speciation in volcanic plumes using *in-situ* derivatization with coated filters and alkali traps

B. Geil, Mainz/DE, T. Hoffmann, Mainz/DE

B. Geil, University Mainz, Duesbergweg 10-14, 55122 Mainz/DE

Several techniques are available for monitoring volcanic activity, including remote sensing, e.g. DOAS, satellites, etc., as well as *in-situ* measurements such as Raschig tubes and filter packs.[1] Nevertheless, these measurements have advantages and disadvantages. A new approach to measuring volcanic gases is the use of drone-based measurements within the volcanic plume. This results in measurements that would be impossible or too dangerous without a drone. However, there are some challenges with drone-based measurements, such as the weight of the measurement system and the relatively short sampling time. Existing techniques are currently unsuitable for measurements using drones as they are either too heavy or the detection limits are insufficient. A new approach here is the development of a lightweight system called "bubbler", which is based on the functional principle of a drechsel bottle. This basic trap provides the good absorption properties of a Raschig system and is significantly lighter in its structure. The smaller sample volume promotes a greater accumulation of analytes. Furthermore, the subsequent treatment was also improved regarding sampling volume, time and limit of quantification.

Small syringe filters replace heavy denuders and at the same time offer improved absorption and detection limit of oxidised halogen species ($Hal^{0/+1}X$) as well as new quantifiable substances within the volcanic plume (Cl_2, BrCl, Br_2).

Literature:

[1]: Wittmer, J. et al.: Active alkaline traps to determine acidic-gas ratios in volcanic plumes: Sampling techniques and analytical methods, AGU Publications, 15, 2797-2820, https://doi.org/10.1002/2013GC005133, 2014.

Drones as flying measuring platforms: Halogen speciation in volcanic plumes using in situ derivatization with coated filters and alkali traps

B.Geil[1]✉ ,N. Bobrowski[2,3] ,N. Karbach[1] and T. Hoffmann[1]✉

[1]Department Chemistry; Johannes Gutenberg University Mainz, Germany (✉ hoffmant@uni-mainz.de), bageil@uni-mainz.de)
[2]Institute of Environmental Physics, Ruprecht-Karls-University Heidelberg, Germany
[3]Istituo Nazionale di Geofisica e Vulcanologia – Osservatorio Etneo, Catania, Italy

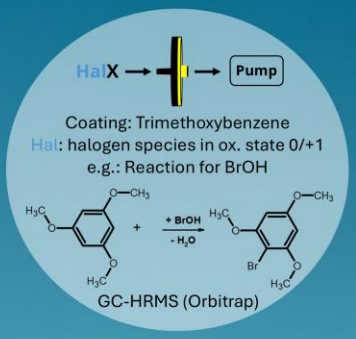

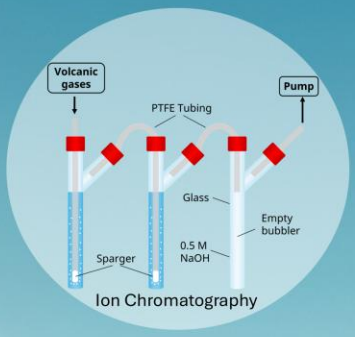

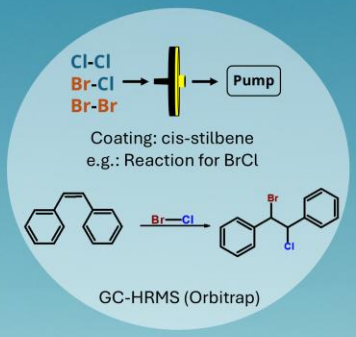

Cl_2, BrCl, Br_2, BrO, IO, $BrONO_2$, SO_2, OClO, ...

Oxidation by ambient air (Ozone)

HCl, HBr, HI, SO_2 ....

Bubbler:
Analytes: total halogens and S
Solution: 4 ml each bubbler
Absorption Efficiency: 99 %
Recovery Rate: 90-95 %
LOQ: hundreds of ppbv (F,Cl,S)
3 ppbv for Br
Sampling time: 15 min
Pump flow: 250 ml/min

Filter methods:
Analytes: HalX, Cl_2, BrCl, Br_2
Absorption Efficiency: > 99.9%
Recovery Rates: 87-97 %
LOQ: few pptv
Sampling time: 15 min
Pump flow: 250 ml/min

Introduction:
Several techniques are available for monitoring volcanic activity, including remote sensing, e.g. DOAS, satellites, etc., as well as in situ measurements such as Raschig tubes and filter packs. A new approach are drone-based measurements within the volcanic plume. Existing techniques are currently unsuitable as they are either too heavy or the detection limits are insufficient. A new approach here is the development of a lightweight system called “bubbler”, which is based on the functional principle of a drechsel bottle. This basic trap provides the good absorption properties of a Raschig system and is significantly lighter in its structure. The smaller sample volume promotes a greater accumulation of analytes. Furthermore, the subsequent treatment was also improved regarding sampling volume, time and limit of quantification. Small syringe filters replace heavy denuders and at the same time offer improved absorption and detection limit of oxidised halogen species ($Hal^{0/+1}X$) as well as new quantifiable substances within the volcanic plume (Cl_2, BrCl, Br_2).

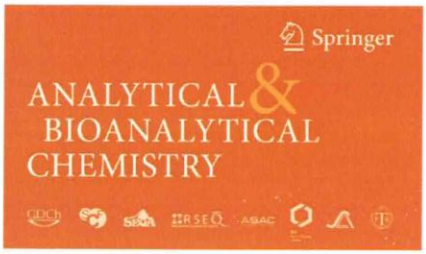

Springer

Poster Award for

Bastien Geil

Drones as flying measuring platforms: halogen speciation in volcanic plumes using in situ derivatization with coated filters and alkali traps

Congratulations! You are the winner of a poster prize awarded for excellent presentation of analytical research on the occasion of the

ANAKON 2025

10th-13th March 2025

Leipzig, Germany

This Award, sponsored by *Analytical and Bioanalytical Chemistry*, entitles you to a free selection of books published by Springer up to a value of 330,- Euro.

N. Oberbeckmann-Winter

Nicola Oberbeckmann-Winter
Managing Editor
Analytical and Bioanalytical Chemistry

Please send your book selection, including a copy of this certificate, to: abc@springer.com. You are warmly invited to submit a research paper based on the results of your presentation for consideration in 'Analytical and Bioanalytical Chemistry' should it be clearly within the aims&scope of this journal (www.springer.com/abc). With your submission, please indicate that you received this award. You are welcome to add a respective footnote to your manuscript.

PoV, Hannover 2023

Halogens and Interhalogens in volcanic plumes

Bastien Geil[1], Niklas Karbach[1], Nicole Bobrowski[2,3], and Thorsten Hoffmann[1]
1Johannes Gutenberg-University, Department Chemistry, Mainz, Germany
2Institute of Environmental Physics, Ruprecht-Karls-University, Germany
3Istituto Nazionale di Geofisica e Vulcanologica - Osservatorio Etneo, Italy

Halogens in volcanic plumes are important for both volcanic and environmental research. For example, changes in the composition of the volcanic plume can be an indication of changes in the activity of the volcano. Volcanic emissions consist mainly of emitted H_2O, CO_2 and SO_2 and are rapidly mixed with surrounding background atmosphere. Additionally, HF, HCl and HBr are also significant constituents of volcanic emissions.

A particularly interesting element in this context is bromine because of its atmospheric relevance. Among others BrO forms in the volcanic plume and, like SO_2, can be determined spectroscopically using remote sensing techniques, making it ideal for monitoring and surveillance of volcanoes. However, to interpret and use BrO concentrations, we need to fully understand the formation and evolution of BrO in volcanic plumes. Measuring all relevant halogen species can take us one step further in our understanding of the interaction between atmosphere and volcanic gas and particle emissions.

Currently, several methods are used to detect the various halogen compounds. Remote sensing methods exist for only a few (in general BrO, OClO, HCl, HF). We use *in-situ* sampling methods such as diffusion separators, filter packs or aqueous alkaline traps to collect reactive and total halogen species, respectively.

In this study, we will present results for Cl_2, Br_2 and BrCl in volcanic plumes using AV based *in-situ* measurement with *cis*-Stilbene coated syringe filters for halogens and interhalogens (i.e., Cl_2, Br_2 and BrCl). The results are discussed considering the different degassing activities and halogen chemistry in volcanic plumes.

E: KI-Tools

Tool	Used for	Where
Open Ai Chat GPT 4.5-5.2	Readability, Translation, grammatical corrections,	Complete Document
Open Ai Chat GPT 5.2	Generating Figures	Figure 1: Background
Deepl	Translation	Complete Document
Deepl Write	Readability	Complete Document